Elastic interactions with the great wave off Kanagawa:

An experimental study on the influence of plate-wave configurations and entrainment of air during hydroelastic impacts

Master Thesis

T. van Gestel

TU Delft

Elastic interactions with the great wave off Kanagawa:

An experimental study on the influence of plate-wave configurations and entrainment of air during hydroelastic impacts

by

T. van Gestel

Studentnumber: 6042392

November 7, 2025

Supervisor:	Dr.ir. P.R. Wellens
Thesis committee:	Dr. A. Coraddu
	Ir. M.M. Bockstael
Project Duration:	January, 2025 - November, 2025
Faculty:	Faculty of Mechanical Engineering, Delft
Master:	Offshore and dredging engineering
Cover:	Sarano, V. [1]

TU Delft

Abstract

This report explores recent developments in research on breaking wave impacts on offshore structures. Through a literature review, research questions are formulated to form the basis of the thesis, along with the planned approach for addressing these questions. The report begins with an overview of breaking waves, their chaotic nature, the influence of fluid-structure interaction and effects of scaling. The literature review identifies a knowledge gap regarding the influence of time-varying mass on structural response and whether wave impact characteristics can be determined through analysis in the spatio-temporal domain. The main research question is:

How do hydroelastic effects influence the structure response during specific breaking wave type interactions?

To investigate this question, a two-dimensional scale experiment is carried out using a sloshing tank to generate waves and examine their impact on a plate. The behaviour is compared to a CFD model capable of computing rigid wave impacts.

The results show that for a cantilevered plate, the relative angle between the incoming wave and the plate strongly influences the magnitude of peak forces and pressures. Different wave geometries excite distinct structural responses, and frequency analysis of the plate deformation reveals a link to the wetted interaction between the wave and the plate. Plate deformation is governed by the combined effects of flexibility, aeration, and wave alignment, which interact non-linearly to determine the overall response, highlighting the complex dynamics of hydroelastic wave–structure interaction.

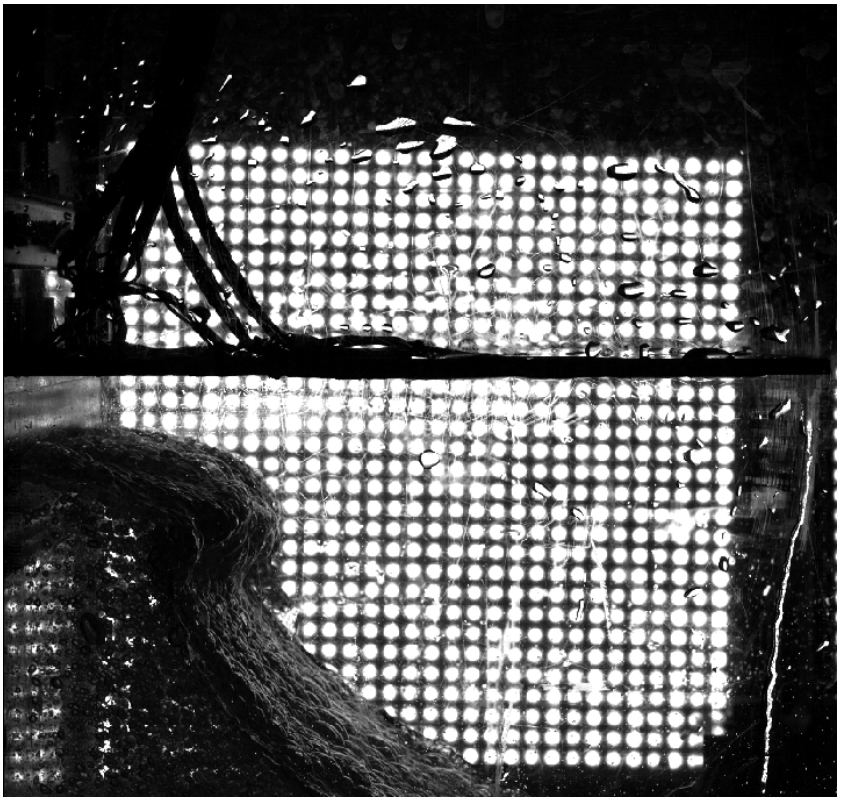

Figure 1: An aerated wave on the verge of impacting the overhanging plate

Preface

During my master's in Offshore & Dredging Engineering at Delft University of Technology, the curriculum revolved around hydro-, structural-, and soil mechanics, all describing the interaction between water and the offshore environment. From high-resolution CFD simulations and non-linear wave modelling to complex frequency analyses of wave-structure interactions, each course provided an advanced perspective on the offshore environment.

Yet throughout my academic journey, I often found myself wondering: How did scientists such as Daniel Bernoulli (1700–1782), William Froude (1810–1879), and Sophie Germain (1776–1831) connect mathematics and physics? With the limited tools of their time, were they theorist with great physical intuition, or was their question simply: How and why?

This exact question was for me the motivation to conclude my master's with a similar mindset. Certainly not to the extent of those exceptional scientists, but with the same spirit of exploration. In the context of my field of research, this translated into questions such as: How does water behave? What is the role of air in breaking waves? Why do structures interact the way they do? And ultimately: How are all these phenomena connected? In essence simple questions, on which I had the privilege to touch upon for the last year in the academic environment, while others spend an honourable lifetime exploring them. And finally after these past 10 months, I am pleased to say that I have come a bit closer to understand these mad scientists from the 18th century.

Tyl van Gestel

Contents

1

Introduction

Katsushika Hokusai's iconic *The Great wave off Kanagawa (1831)*, has captured both artistic imagination and scientific curiosity. The cresting form of Hokusai's wave, ready to swallow the fragile boats below, reflects the very real threats posed by breaking waves to offshore structures today. The work gives a visual analogy to the physics involved with wave impacts, including entrained air at the curling wave crest. With rising wave heights and increasing impacts due to climate change [2], understanding wave behaviour and its coupling to offshore structures has become more critical. Offshore wave loads are designed based on historical wave data, yet as environmental conditions evolve, the safety and integrity of offshore structures face growing challenges, and events of injury and death may arise [3]. Increasing loads from extreme wave events therefore impose significant risks, including structural failure, marine accidents, and severe economic and human losses. To mitigate these risks, a deeper understanding of wave impacts and their interaction with structures is essential.

This study aims to advance knowledge of fluid-structure interactions in the context of breaking waves. The key focus is the role of hydroelastic effects, which influence the varying contact time between breaking waves and offshore structures. Hydroelasticity examines the motion and deformation of flexible structures under hydrodynamic, inertial, and elastic forces, making it a crucial factor in predicting wave-induced loads more accurately. The impact duration and temporal variation of the impact loads on offshore structures are governed by multiple interrelated factors. These include the velocity profile of the wave tip, the wetting time and area of the structure, and its wet natural period, which all dictate the oscillatory response. Other complexities, such as air entrapment, structural scale effects, and the three-dimensional nature of wave-structure interactions, further influence impact forces, but complicate the characterisation of specific wave phenomena. It raises the question of whether this theoretical development will bring clarity or introduce new uncertainties into the existing chaos of breaking wave interactions.

By interrelating wave geometries, hydroelastic effects, and entrainment of air within the spatio-temporal domain, this research seeks to expand the knowledge on wave impacts on structures, contributing to the safer and more resilient design of offshore structures in an era of changing ocean conditions.

2

Literature review

Understanding the characteristics of impact loads enables a better prediction of structural responses under different wave-breaking scenarios. Hydro-elasticity defines the two-way coupling between the wave loading and structure response and is up to this day a complicated engineering problem which requires further investigation. Simulation models are often built on incompressible solvers, whereas in reality breaking waves contain trapped air and offshore structures are loaded by an air-water mixture instead of incompressible water. In this chapter, breaking wave characteristics are described, characterisation methods are discussed and the knowledge gap is identified which reveals the motivation for the research presented in this thesis.

2.1. Breaking wave impacts

Breaking wave impacts occur when ocean waves reach a critical height and collapse, potentially crashing into offshore structures such as platforms, vessels and breakwaters. These impacts are intense and highly dynamic, delivering concentrated forces over very short time intervals. Unlike regular wave loads, breaking waves generate sudden and impulsive pressures that can exceed the structural design limits if not properly accounted for.

The stages in a breaking wave can be categorised in three critical moments in time: breaking onset, the incipient point and the impingement point [4], [5], see Figure 2.1. The breaking onset refers to the critical moment beyond which wave breaking cannot be avoided. This is followed by the incipient point which marks the beginning of wave overturning, characterised by a vertical wave front. And at last, the impingement point is the location where the wave crest makes contact with the water surface ahead of it.

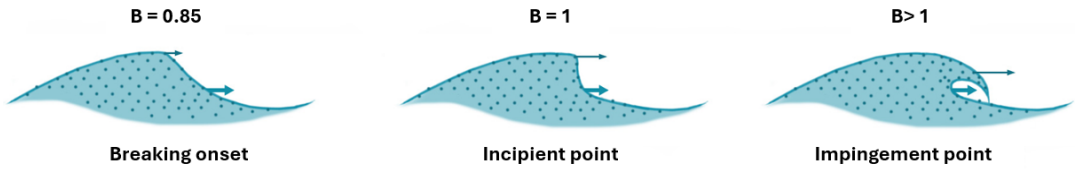

Figure 2.1: Critical moments in time of breaking waves

Varing [5] defined a kinematic breaking criterion B as:

$$B = \frac{||u||_m}{C_x} \tag{2.1}$$

where C_x is the wave speed and $||u||_m$ represent the maximum free surface particle velocity magnitude, which is dependant on the horizontal and vertical free surface velocity.

$$||u||_m = max(\sqrt{u_x^2 + u_z^2}) \tag{2.2}$$

The wave speed C_x is described based on the linear dispersion relation, where $h(x)$ is the water depth and depends on the bathymetry and the wave number k.

$$C_x = \sqrt{\frac{g \cdot tanh(k \cdot h(x))}{k}} \tag{2.3}$$

There, g is the acceleration due to gravity, the wave number k relates to the wave speed and the angular wave frequency ω:

$$k = \frac{\omega}{C_x} \tag{2.4}$$

Equation 2.1 up to Equation 2.4 relate measurable quantities to different wave shapes. However, breaking waves include other complex phenomena. Lafeber [6] identified three elementary Loading Processes (ELPs) when a breaking wave impacts a flat or a corrugated wall: direct impact (ELP1), the building jet (ELP2) and the compression/expansion of entrapped or escaping gas (ELP3). Wave impact types are often defined as a slosh, a flip-through, a gas pocket, or an aerated type of wave impact, showing that braking wave impacts can undergo multiple phases during impact [7].

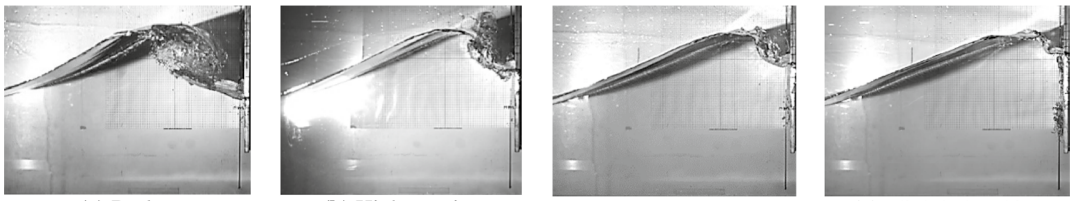

(a) Broken **(b)** High aeration **(c)** Flip-through **(d)** Slightly breaking

Figure 2.2: Different stages of a breaking wave [8]

In Bos [9], an experiment was conducted to measure the response of a one degree-of-freedom pendulum in a focused, breaking wave. Although the energy of the wave input was the same for all experiments, the response of the pendulum varied greatly with small variations of initial vertical clearance and wave focus location. Both the wave impact on a breaking wall and the wave impact on the pendulum show variability in measured impact pressures and forces. The difference is that the pressure impulse is constant for a wall [10], but not for the pendulum as the impacted object is moving. Variability in measured impact pressures has been described more often [11], [12]. The loads and structural responses were found to align with experimental observations only when the added mass effects were taken into account. Differences between the one degree-of-freedom pendulum and a vertical wall are the freedom to move of the pendulum, reduced air entrapment during breaking waves and the impact time on the structure with varying added mass effects. Bos [9] touches upon a wide variety of breaking waves characteristics, underlying the effects of varying added mass and introducing the chaos of breaking wave behaviour and the response of elastic structures.

2.1.1. Wave instabilities

Instabilities on wave crests and gas flow dynamics significantly influence impact pressure variability. The development of vortices and secondary circulation alters gas velocity near the wave crest, introducing additional lift and variability [13]. However, understanding the exact dynamics of the wave crest involves complex physics and multiple possible causes of instabilities and perturbations, making it difficult to exactly define the origin of the wave variability. Derakhti [14] investigated the total loss of wave energy and momentum flux associated with wave breaking, analysing the spatial variation of these fluxes in intermediate- and deep-water unsteady breaking waves generated by dispersive focusing. It was shown that the widely used formulas over-predict both fractional and total losses of horizontal wave energy flux by approximately 35–70% for the breaking packets, due to the neglect of the increase of the characteristic group velocity after the breaking region. Turbulence induced by vortices and secondary circulation near the wave crest plays a key role in modulating impact pressure variability and the spatial distribution of energy and momentum dissipation during wave breaking.

2.1.2. Entrainment of air

The air entrainment in waves appears both as distributed aeration with bubble clouds and void fractions dispersed in the water column and as large-scale entrapment such as cavities of air trapped beneath overturning jets. The degree of aeration has strong implications for wave dynamics, energy dissipation, and impact loads on marine structures and the stages of development and types of air pockets lead to impact specific pressure profiles [10], [15]. Quantifying the air content during breaking waves remains challenging due to the turbulent and highly complex flow fields created by air–water mixing. Reported air volume fractions during breaking events range from as low as 0.1% up to about 20% [16], and literature has even documented values as high as 55% [17]. Peregrine [18] further notes that significant reductions in pressure may occur even with relatively small amounts of entrained air in violent, confined flows. Additionally, void fractions have been observed to decrease exponentially with depth [16], [19].

Air entrapment

Large-scale air entrapment can occur when an overturning wave collapses and encloses air, or when a filling flow traps a void as a result of specific interactions between the wave and structural features, such as cracks or angled corner plates on offshore structures. Bredmose [20] carried out numerical investigations of wall pressure, impact force, and impulse during flip-through impacts under both low- and high-aeration conditions at different scales. For high-aeration impacts, it was observed that the air pocket undergoes closure and continued compression until the maximum pressure is reached. The study also revealed a distinct vertical distribution of pressure within the pocket and that pressure waves propagate downward along the wall before the peak impact pressure occurs. Compared with low-aeration impacts, larger air pockets lead to a longer duration of the large impact pressure.

In the process of breaking waves, the large scale entrapped air may also be broken down and additional splash formation leading to dispersed aeration [18], [21], which on its turn influences the impact. This happens through dissolution, diffusion, and degassing while large variations in the temporal and spatial distributions of the bubbles occur during this cycle. The timescales of the lifecycles of the bubble plumes vary greatly, from hundreds of milliseconds during bubble creation to hundreds of seconds for bubble dissolution and degassing [22].

Aeration

Dispersed aeration reduces the water density and introduces a two-phase compressible mixture behaviour, potentially cushioning impacts and reducing impact pressures. Dispersed aeration results from the entrainment of air during wave breaking into the water column. In plunging breakers, the crest jet impacts the free surface, forming a primary air cavity followed by multiple entrainment events, including jet-impact, backward-splash, splash-impact, leading-edge, and turbulent mechanisms. Spilling breakers, in contrast, exhibit a simpler pattern dominated by leading-edge and weak turbulent entrainment, with shallower and less intense air incorporation [23].

A small fraction of air dramatically lowers the sound speed [24]. Mach numbers based on this sound speed can reach significant values in large-scale flows. The Mach number is described as:

$$M = \frac{U}{c} \tag{2.5}$$

where U is the flow velocity and c is the speed of sound in the flow medium. When $M < 1$ it describes a subsonic flow, at $M = 1$ a sonic flow and when $M > 1$ a supersonic flow is present. The ratio of the impact velocity to the speed of sound in water can be used to assess when compressibility effects in aerated water become significant. The effective speed of sound in the homogeneous aerated mixture, c_f, can be computed using Wood's equation [25]:

$$c_f^2 = \frac{1}{\rho_f \left(\dfrac{\alpha}{\rho_g c_g^2} + \dfrac{1-\alpha}{\rho_l c_l^2} \right)}, \tag{2.6}$$

where $\rho_f = \alpha\rho_g + (1-\alpha)\rho_l$ is the mixture density, α is the gas void fraction, ρ_g and ρ_l are the densities of gas and liquid, and c_g and c_l are their respective speeds of sound.

Breaking waves impacts generate high local pressures over short timescales where the flow velocity may be larger, resulting in water-hammer type impacts and shock formation. For violent aerated wave impacts, a part of the impact energy goes into compressing the bubbles, and not solely into forcing pressure onto the structure. Although the pressure peaks may be lower, the extended contact time and area may result in an increased pressure impulse [10]. Via numerical and experimental research of water entry of cones, Elhimer [26] found that compressibility has a relevant effect on the impact pressure for edge Mach number (an additional factor of $1/tan(\alpha)$ to account for the wedge entry angle α) above 0.05. Based on experimental research from van der Eijk [27] it was concluded that when $0.05 < Ma_{edge} < 0.3$ the largest changes in impact pressures are found. Further research is needed on various wave–plate interactions, particularly regarding the effects of entrapped air and aerated water on pressure transmission and dynamic loading. This will help clarify how aeration affects different breaking wave–plate interactions and how these effects are related to the Mach number.

2.1.3. Fluid-structure interaction

Based on high-speed video recordings of wave motion, Zhang [28] identified two phases of breaking waves which are most crucial for developing high loads on columns of offshore structures based on a small scale model, namely a spilling breaker with air cavity and plunging breaker with small air cushion. In their research they found that in addition to local wave steepness, there are three other parameters that play a dominant role in the identification of the breaker type in the presence of a structure, revealing that the structure has a significant influence on wave breaking characteristics:

- d_f/d_s: The ratio of the water depth at the column front d_f when the wave breaks and the still water depth d_s.
- d_b/d_s: The ratio of the water depth at the column back d_b when the wave breaks and the still water depth d_s.
- v_h/v_u: The ratio of the horizontal velocity of the breaker crest v_h and the vertical upward velocity of the water surface at the column front v_u.

The location of the maximum local impact load is related to the breaker type, and the spilling breaker was found to cause the most severe wave impact on the column structure [28]. For the spilling breaker, similar magnitudes were found, although at a different occurrence position, and the presence of the small air cushion increased the duration of the breaking wave pressure. In their research, they discovered that the breaker type could be identified from wave impact loads without using any records of the wave motion, thus bypassing the need for elaborating complex physics of breaking waves. In Figure 2.3, the spatial variation of a pressure impulse induced by different breaker types and the corresponding rise and fall durations are illustrated. Since the magnitude of a pressure impulse is not only related to the peak impact pressure, but also depends on the total duration of the impact pressure, the spatial variation of a pressure impulse appears to be a combined result of changes in both the peak impact pressure and the duration.

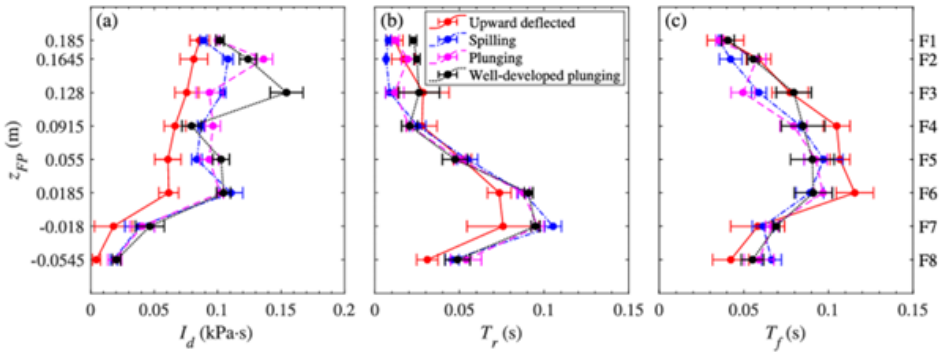

Figure 2.3: Spatial variation of the pressure impulse and the durations of breaking wave impacts: (a) pressure impulse, (b) rise duration, and (c) fall duration. The error bar indicates the mean with a standard deviation of peak impact pressures for repeated wave tests [28].

Furthermore, the breaking wave impact process involves multi-scale air entrapment, including air bubbles and air cavities, as well as potential air compression. Since the study focused purely on the wave impact load itself, the material properties of the experimental structure were not specifically considered and appropriate scaling would have to be verified.

An accurate understanding of the plate flexibility effect on wave impact is still a challenge and new methods of analysis are needed to improve the understanding of the interaction between waves and flexible structures. There have been different conclusions about the effect of flexible structures. Mai [8] looked at slamming impact pressures and forces which were considerably reduced for the elastic plate compared to the rigid one, though only at high impact velocities. The total impact force on the elastic wall was found to reduce for the high aeration, flip-through and slightly breaking wave impacts. However, the impact pressure decreased on the elastic wall only under flip-through wave impact. Linton [29] and Zhang [30] also observed reduced wave forces at a flexible wall compared to a rigid wall. For impacts on rigid surfaces, some of the total kinetic energy of the fluid is lost. With an elastic impact in which the fluid rebounds from the solid target, there is no kinetic energy dissipation due to the material. This approximation is suitable for real applications, where energy dissipation is expected to be relatively small [31], [32]. According to Attili [31], based on small-scale laboratory tests of wave impact on offshore plates of different stiffnesses, it was concluded that plate stiffness had negligible effects on the upwave forces, with relatively small deviations observed in the total force for simply supported beams. In their findings, the rigid plate did not necessarily result in the maximum wave forces, yet smaller total forces were observed for more deformable offshore plates.

2.1.4. Cavitation

The action of overturning waves can produce very short and intense loadings that are similar in character to the pressure time histories caused from underwater explosions caused by hull cavitation [33]. Cavitation occurs when liquid evaporates and vapour bubbles form in regions where the pressure drops below the saturation vapour pressure. The presence of cavitation can significantly alter the characteristics of an underwater shock wave loading signature compared to a scenario without cavitation and may introduce great variability in measured pressures. Also, cavitation can increase the common pressure on the deforming surface. Cavitation bubbles typically nucleate and collapse on timescales of hundreds of microseconds up to a few milliseconds , depending on their maximum size. This relation may be described by the Rayleigh-Plesset equation [34]. By assuming constant temperature, disregarding surface tension and gas content (which are two assumptions that may be violated during wave impacts), the collapse time from the bubble radius $R = R_0$ to $R = 0$ is described by:

$$t_{TC} = 0.915\sqrt{\frac{\rho_l R_0^2}{p_\infty^* - p_V}} \tag{2.7}$$

Where ρ is the liquid density, ρ_∞ is the ambient pressure and p_V is the vapour pressure. It should be noted that collapsing bubbles may lose their spherical symmetry. The growth time can also be described via a time dependant Rayleigh–Plesset equation, as the radius is a function of time and depends on the pressure history. According to Equation 2.7, for bubble diameters between 0.1 and 10mm, the collapse time is approximately 0.05 to 0.5 ms, meaning that to capture the collapse of cavitation a frame rate of at least 20000 frames per second is needed with implementation of a high speed camera, with the requirements that the resolution of the camera is sufficient to capture the cavitating bubble radius.

For wave impacts, during the pressure loading process, a hull element can move faster than the water. As a consequence, the hull can separate from the water and thus generate so-called hull cavitation in the water. This hull cavitation can increase the pressure on the deforming surface and the effects of the hull/breaking wave interaction. The average pressure is increased because the cavitation limits the magnitude of the suction acting on the hull surface. In the case of the waves of sufficiently long duration, cavitation appears if the pressure in the water drops to the order of 0.2 to 0.35 MPa [35], relative to the local absolute pressure field during impact. These values are several orders of magnitude above the thermodynamic vapor pressure because of nuclei effects and hydrodynamic conditions such as turbulence [34]. Galiev [35] stated that the effect of cavitation is expected to be important if the duration of the loading by the water pressure is less than the fundamental period of the plate vibration. Galiev

[35] serves as an example that cavitation may occur sooner in real flows. The susceptibility of a flow to cavitation is commonly expressed in terms of the dimensionless cavitation number σ, defined as:

$$\sigma = \frac{p_\infty - p_v}{\frac{1}{2}\rho U^2} \tag{2.8}$$

where U is a characteristic velocity of the flow. The cavitation inception number σ_i denotes the value of σ at which cavitation is first observed. A low value of σ_i indicates that the liquid must be driven close to its thermodynamic vapour pressure before cavitation occurs. Contrarily, a high value of σ_i implies that cavitation appears at much higher absolute pressures, reflecting a liquid with abundant nuclei or turbulence [34].

2.2. Characterising wave impacts and hydroelasticity

The effects of hydroelasticity and air entrainment significantly increase the contact time between the breaking wave and the structure, introducing new phenomena to the pressure impulse variability as a continuation of wave characteristics/instabilities [12], [36]. Together with scaling uncertainties presented by Attili [37], a new approach towards defining breaking waves is needed. In the case of extreme loads, the largest interest is towards plunging and spilling breaking waves/flip through for the direct application of offshore structure integrity analysis's [9], [28], [38].

2.2.1. Hydroelasticity

Faltinsen defined the importance of hydroelasticity for an elastic hull with wedge-shaped cross-sections penetrating an initially calm water surface based on the ratio between the wetting time of the structure and the greatest wet natural period of the stiffened plating using orthotropic plate theory [39], see Figure 2.4(a). Faltinsen introduced the following non-dimensional parameter:

$$\xi = \frac{tan(\beta)}{V\sqrt{\rho L^3/EI}} \tag{2.9}$$

where L is the length of the analysed longitudinal stiffener between two successive transverse frames, β is the dead rise angle, V is the impact velocity, ρ is the water density, and EI represents the bending stiffness. The parameter ξ is proportional to the ratio used by Bereznitski [40] between the wetting time of the rigid wedge which is the load duration T_d and highest natural period T_{n1} of the stiffener which is described in Equation 2.10.

$$Ratio = \frac{T_d}{T_{n1}} \tag{2.10}$$

Figure 2.4(a) shows their results obtained including a quasi-steady analysis, which assumes the structure behaves rigidly in the hydrodynamic calculations, and an asymptotic hydroelastic analysis applied for small deadrise angles.

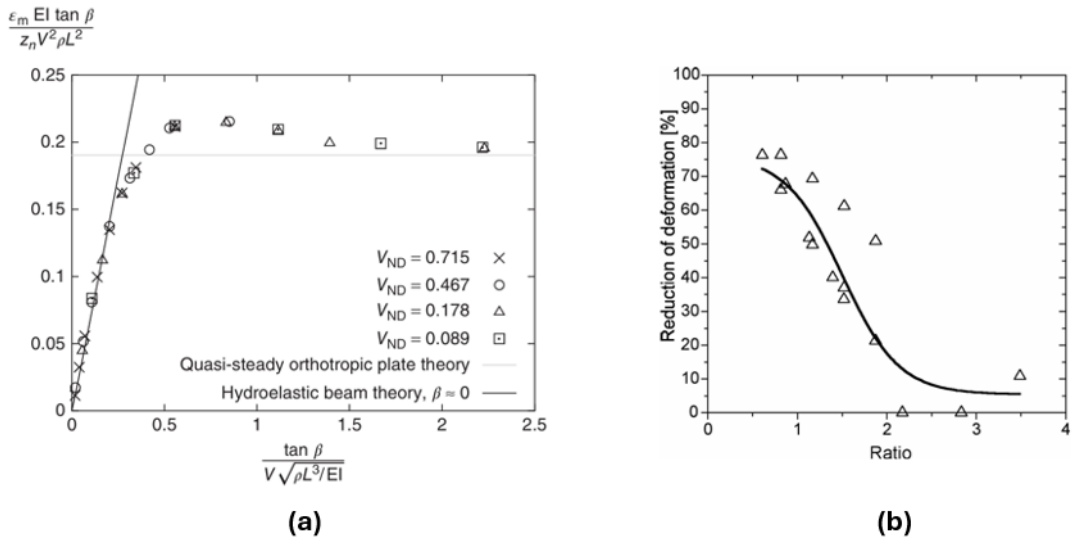

Figure 2.4: Graphs showing the importance of hydroelasticity: (a) the non-dimensional maximum strain ϵ_m in the middle of a longitudinal stiffener at the keel for different non-dimensional constant impact velocities V_{ND} [39], (b) a function of ratio between the duration of impact and the first period of natural vibration of the dry beam [40].

Bereznitski [40] found that the ratio between the impact duration and the period of first mode of vibration of dry structure is the key factor in determining the importance of hydroelastic effects. A small ratio means that hydroelasticity is important and a large ratio means that hydroelasticity is not important, see Figure 2.4(b). The duration of the impact is the impulse duration for the rigid body penetration where the effect of air is included.

Additionally, his research looked into parameters such as the stiffness of the structure, presence of entrapped air between the structure and the water surface, and penetration of water at different dead rise angles. This ratio was found to be proportional to the dead rise angle and inversely proportional to the impact velocity. It was observed that for small dead rise angles $(0° - 5°)$, the presence of entrapped air between the structure and the water surface significantly reduces impact loads and structural deformation. The entrapped air acts as an effective cushion. The presence of entrapped air therefore increases the duration of the impact which means that the impact can not be extremely short. Since the effect of hydroelasticity is the most important for impacts with a very short duration, air entrapment has a large influence on whether breaking wave impacts may be considered hydroelastic.

Bos [9] studied the effect of hydroelasticity on freely floating maritime structures upon impact of breaking waves by analysing breaking waves hitting a suspended pendulum. By means of image processing of high-speed camera images, they found that although the largest pendulum response occurs for the largest wave front velocity, and the lowest response for the lowest wave front velocity, the maximum front velocity and angle do not correlate well with the response. The response correlates best with the surface elevation at the position of the pendulum. This was confirmed by the results of a reduced-order model that translates the surface elevation near the pendulum to a force and subsequent response corresponding well with the experimental results, without wave front velocity and angle. The response also showed a variability between experiments in which focus position and initial vertical clearance were kept the same. The largest variability of the response was observed for the wave breaking farthest away from the position of the pendulum; it is thought that the variability is largest for this condition because here the overturning breaking wave has had the longest time to entrain air and to generate smaller flow structures, again underlining the importance of time variance, entrained air and the associated contact time of a wave impact.

2.2.2. Rise time

The loads on offshore structures can be characterised by looking at the rise time in the presence of hydroelastic behaviour. The pressure rise time may be defined as the time difference between the point at which the pressure starts to rise to the point of peak pressure, see Figure 2.5 [41]. The question arises whether pressure rise times associated with different breaking wave types can be linked to the wetted natural frequencies of structures, as well as the time-varying added mass effect and its significance in hydroelasticity. Bullock [10], characterised breaking with low aeration by high impact pressure with short rise times, and breaking with high aeration by pressure oscillations caused by the oscillation of the entrapped air pockets. Research of Chella [42], indicates that the angle of the wave front edge impacts the rise time and the initial sharp increase of the impact load. Govindasamy [41] investigated the pressure distribution of breaking waves on monopiles where for impacts caused by a fully developed overturning jet, the rise time becomes even shorter for wave groups of low steepness. Notably, the shortest rise time does not correspond to the largest impact pressure but instead shows a trend depending on a combination of wave steepness and impact conditions.

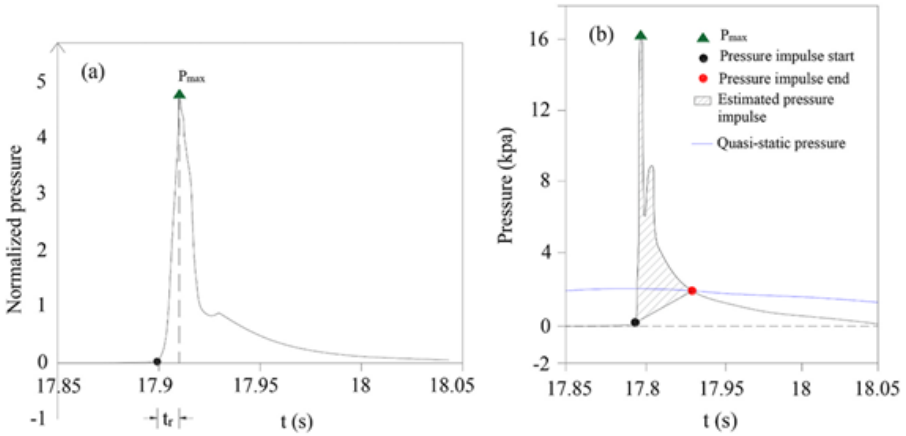

Figure 2.5: Definition sketch for (a) pressure rise time and (b) pressure impulse.

Hu [36] studied the interaction between breaking waves and an elastic wall. It was found that the impact force, impact duration, and impact impulse are affected by the structural deformation in progressive waves. Their model showed that the incompressible air assumption can provide reasonable predictions for the peak impact force and quasi-hydrostatic force but is less effective at reproducing the impact duration and sub-atmospheric pressure, compared with the compressible air assumption. Nonetheless, the two-dimensional compressible simulation can lead to over-predicted pressure oscillations. For future studies they suggested studying the effect of air compressibility together with the effects of three dimensionality and structural responses for predictions of violent breaking wave impacts on structures at a large scale. Studying the loading time and rise time may be relevant to connect these topics.

2.2.3. Added mass

Added mass, representing the dynamic reaction force from the fluid, varies over time during impact and depends on both the wetted area and the geometry of the impacting wave. A similar observation was reported by Lugni [7], who described sloshing model tests incorporating fluid-structure interactions for a flip-through impact. As previously discussed, Faltinsen established a relationship to define the importance of hydroelasticity by looking at the water entry of a wedge. However, the solution uses only one structural mode, the added mass is assumed constant in space and time. The reason for this was that the lowest mode is most important for the maximum strain, that the maximum strain occurs on the time scale of the natural period of the lowest mode, and that structural damping of the lowest mode is small.

Abrahamsen adds another method in solving the hydrodynamic problem by using a 2D boundary element method at different submergences by accounting for the hydrodynamic load modification due to the structural vibrations, where the added mass matrix varies with time [43], [44]. An additional term

to the classic approach by Faltinsen [39] is given, by the introduction of slam damping. Slam damping is a hydrodynamic pressure proportional to both the deflection velocity and the impact velocity, and accounts for the fact that the effective slamming force depends on relative impact velocity, i.e. the impact velocity minus structural deflection velocity.

There is room for interpretation regarding the choice of added mass for the classic dynamics method, and the added mass calculated for the fully wetted beam is an upper bound. The methods depend on an analogy between the wave impact and a planar structure ('wedge') impacting an undisturbed free surface, in that the measured impact pressure peaks and load rise times are converted to equivalent impact velocities and dead rise angles of a wedge. This gives a reasonable correspondence between the pressure time history of the wedge impact compared to the measured pressure time history, but could be improved for breaking waves of specific types and other plate configurations.

Abrahamsen [43] explored the effect of hydroelasticity on local structural FPSO response due to measured wave impact loads by modelling a vertical beam at the upper flare of a vessel as an Euler beam fixed on the lower end and pinned on the upper end. Based on the measurements of the experimental setup, triangular pressure time histories were fitted to the measured beam pressure time histories to estimate the load duration and to simplify the response calculations, see Figure 2.6. Subsequently, these spatio-temporal histories can be used as input to the structural dynamics calculation (Equation 2.15) and may be characterised for specific wave types and related to the effect of added mass and the wet natural frequencies of structures. The response of the plate, simplified to a 2D Euler-Bernoulli beam, is described as follows:

$$\rho A \frac{\partial^2 w}{\partial t^2} + EI \frac{\partial^4 w}{\partial x^4} = p(x,t) \tag{2.11}$$

The displacement of the plate $w(x,t)$ is expressed as a linear combination of its natural mode shapes $\phi_i(x)$ weighted by the corresponding modal coordinates $q_i(t)$ for the number of considered modes n:

$$w(x,t) = \sum_{i=1}^{n} \phi_i(x) q_i(t) \tag{2.12}$$

The governing equation for each modal coordinate can be written as:

$$(m_i + m_a)\ddot{q}_i(t) + c_i \dot{q}_i(t) + k_i q_i(t) = F_i(t), \tag{2.13}$$

where m_i, m_a, c_i, and k_i denote the modal mass, added mass, damping, and stiffness, respectively, and $F_i(t)$ represents the modal forcing obtained by projecting the external hydrodynamic load distribution $p(x,t)$ onto the i-th mode shape:

$$F_i(t) = \int_A p(x,t)\, \phi_i(x)\, \mathrm{d}A. \tag{2.14}$$

The deformation of the beam is assumed to be dominated by the first mode of response associated with the lowest natural frequency of the system. The added mass is defined in the following equation [43] and approximation [45]:

$$m_a = \rho B \int \phi(x)\Phi(x)dx \approx \frac{2\ln(2)}{\pi} \rho L^2 B \bar{\phi}^2 \tag{2.15}$$

where $\Phi(x)$ is the velocity potential. The wet natural frequency f_w, dependant on the stiffness k and total mass, may then be computed as:

$$f_w = \frac{1}{2\pi}\sqrt{\frac{k}{m + m_A}} \tag{2.16}$$

The second term presented in Equation 2.15 is the approximation of a constant added mass where a relevant wetting of the structure needed to be selected, presented by Faltinsen [45]. For the added mass calculations, the whole flare was assumed submerged with the free surface intersecting the upper (pinned) end of the flare beam [43]. The wet natural frequency was calculated assuming that the wet mode shape was equal to the dry mode shape. Furthermore, incompressible potential flow theory was assumed valid, which meant that the water flow was described by the velocity potential $\phi(x)$, which satisfies the Laplace equation. However, modal analysis assumes linear, time-invariant coefficients. In scenarios where the added mass varies over time, such as during a breaking wave impact, the eigenvalue problem cannot be solved. Consequently, the Faltinsen's [45] approximation is not applicable to breaking wave impacts or the study of hydroelastic interactions, since the added mass effect varies significantly in the spatio-temporal domain.

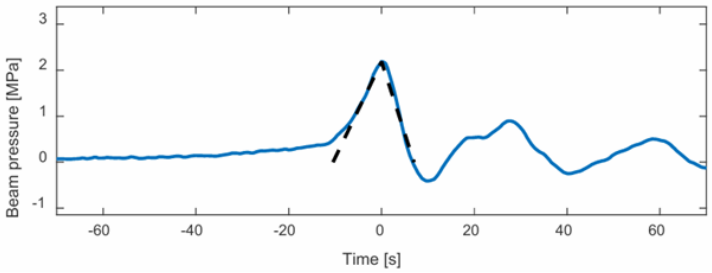

Figure 2.6: Spatially averaged pressure time series acting on the beam and fitted simplified triangular pressure time histories [43]

2.3. Numerical approximations

Bos [46] presented a reduced order model for ELP2 based on the Wagner impact model, in the form of non-hydrostatic shallow water equations made suitable for numerical implementation of the coupling between the fluid and structure interaction. Figure 2.7 shows how the reduced order model from the paper relates to an actual wave impact, where the orange lines approximate the shape of the breaking wave.

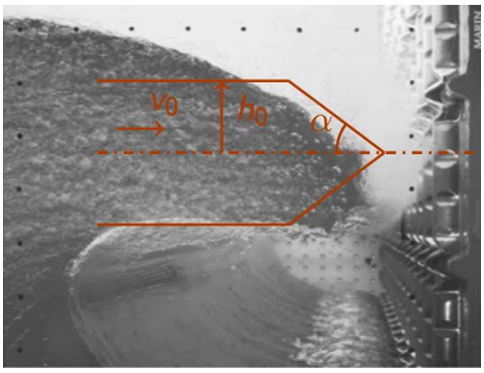

Figure 2.7: Wave impact analysed by Bos [6], [46]. The orange lines represent the cut-off wedge impact which is simulated in this paper. The cut-off wedge has an initial constant velocity v_0 towards the wall, an angle α and an initial height h_0.

For the model, the air density was chosen to be close to zero. It was found that the response is changed by a different load shape with the same total impulse. The response of the wall becomes increasingly dynamic with increasing angle and velocity. As the impact has a higher velocity or steeper angle, the interaction is increasingly important. This is based on two load characteristics: the load rise time is such that it excites the structure and the load magnitude such that it is felt by the structure.

It was also observed that the structural response after impact did not damp out. Over time mass enters the domain with a velocity, therefore adding energy. To solve this a cut-off time was used. In almost all cases, the maximum force in the coupled calculation is higher than in the uncoupled calculation. This is

because the structure initially moves with the impact and then rebounds, reaching the maximum force during this return motion.

When looking at simulating the breaking waves to retrieve a correct impact duration, whether or not the air is assumed compressible has a significant effect. For wave impacts it was found that the effect of compression waves in the air pocket dominates the dynamics and leads to pressure oscillations that are of the same order of magnitude as the pressure caused by the initial impact on the base of the wall [47]. Hu [36] performed two-dimensional simulations of large-scale violent breaking wave impacts on a flexible wall using both compressible and incompressible solvers to determine the temporal evolution of horizontal force on a rigid wall subjected to the high aeration impact. Their results reported that the advantage of using the compressible solver is that the sub-atmospheric pressure and the subsequent damped oscillations can be correctly produced. However, the magnitude and the duration of the oscillations are exaggerated, which are both influencing factors with regards to the pressure rise time. The reason for this simulated phenomenon is that in the physical experiment, the entrapped air pocket may not be completely wrapped by the vertical wall and the highly irregular free surface during the violent impact, resulting in a leakage of air from the pocket. In their case, using the assumption of an incompressible fluid provided sufficiently accurate input for the structural analysis.

To incorporate energy dissipation mechanisms, improved boundary conditions could enhance long-term response predictions. Van der Eijk [48] improved the boundary conditions to model the effect of the high density ratio at the interface in ComFLOW, which is a non-hydroelastic CFD solver based on a Volume-of-Fluid approach. Consistent momentum and mass transport with an additional continuity equation were introduced which preserves the shape of the droplet, resulting in that fluids with different densities are kept separately. A staggered grid with CLSVOF is used for the interface between fluids, describing a consistent momentum and mass method with a temporary continuity equation and is extended with a two-way coupled fluid-structure interaction [47], [49].

In summary, accurately modelling breaking wave impacts involves capturing the complex interaction between the fluid and the structure, as well as accounting for air flow and compressibility effects. Reduced-order models can effectively simulate dynamic structural responses, while compressible solvers better represent pressure oscillations, though they may exaggerate their intensity. Despite ongoing improvements in boundary condition modelling, current methods still face limitations in accurately capturing the highly irregular characteristics of air–water–structure interactions during wave impacts.

2.4. Experimental studies

While numerical simulations enable flexible and repeatable investigation of breaking wave impacts across a wide range of conditions, experimental studies provide insight of complex phenomena like turbulence and air entrainment which are difficult to capture numerically. However, experimental studies also come with limitations: experiments can be costly, time-consuming, and may involve scale effects that complicate extrapolation to full-scale applications, and are constrained by the precision and capacity of test equipment.

2.4.1. Sloshing

Breaking wave impacts may be reproduced with the use of a sloshing tank [45], [46]. Sloshing experiments are relevant for the characterisation of breaking wave impacts for the reason of offering a controlled and repeatable way to simulate complex fluid dynamics similar to those observed in real ocean wave breaking events. When the liquid inside a partially filled tank is subjected to oscillatory motion, the non-linear behaviour of breaking waves can be controlled by alternating the sloshing frequency.

To get hydroelastic effects, large impact velocities are needed which occur when the tank is excited close to the first natural frequency of the fluid. However, resonance does not occur exactly at the natural frequency of the fluid due to the non-linear feature of sloshing problems [50], [51]. For a given rectangular tank, the first natural frequency of the fluid in the tank is given by:

$$\omega_1 = \frac{1}{2\pi}\sqrt{\frac{\pi g}{L} tanh(\frac{\pi h}{L})} \tag{2.17}$$

where L is the tank length, h is the water depth and g is the gravitational acceleration. Although full-scale ocean waves feature complex propagation and run-up processes, sloshing tanks can reproduce similar steepening and overturning of waves along the tank walls. By adjusting the tank geometry, fill level, and excitation frequency, it is possible to generate wave shapes and impact dynamics that resemble breaking waves, making sloshing a useful tool for investigating the concentrated forces, pressure and deflections caused by breaking waves.

2.4.2. Influence of test equipment

Regarding the test equipment, the use of piezoelectric sensors is recommended due to their fast response time [52] as high-frequency measurements can be limited by the rise time of the sensors. Additionally, these sensors have a high natural frequency, which helps prevent resonance with wave interactions and air bubbles while still capturing high-frequency measurements.

It must be kept in mind that small vibrations for pressure measurements after impact can be caused by the natural frequency of the sensor [53]. Additionally, shorter rise and decay times are associated with increasing peak forces. If air bubbles are expected to have an effect, their diameters may be related to frequency using the Fast Fourier Transform (FFT) of the pressure signal [54]. Ha [54] examined wave impact patterns and the effect of air bubbles using measured data, specifically analysing the relationship between air bubble oscillation frequency and the sensor's natural frequency. A strong correlation was found between rise time and forces/pressures for spilling waves, whereas for plunging waves this correlation is influenced by the presence of large air bubbles. Air bubbles near pressure sensors can generate extreme impact pressures. In plunging waves, pressures influenced by air bubbles exhibit very short rise and decay times, whereas pressures without air bubbles have relatively longer rise and decay times. It is clear that for studying the effects of added mass variability and the relationship between rise time, wetted natural frequency, and structural response in offshore structures, that air entrapment needs careful attention.

2.4.3. Effect of scaling

When performing experimental research on breaking waves, the selection of appropriate scaling laws is essential if the aim is to carry out a comparison of the results from the laboratory to full-scale conditions.

In non-aerated water impacts, Froude's law captures the ratio of the water's inertial to gravitational forces, where wave speed, free-surface profiles, and global hydrodynamic loads scale consistently, and the extrapolation of laboratory behaviour to full scale is relatively straightforward [20]:

$$Fr = \frac{U}{\sqrt{gL}} \tag{2.18}$$

where U is the flow velocity and L characteristic length of the impacted structure. The law is based on the assumption that the water surface tension, viscosity and the influence of air can be neglected. However, the presence of entrained air raises doubt on the applicability of the Froude scaling law for scaled experiments involving violent wave impacts [20], [55] as air bubble scaling effects (bubble size, buoyant rise time, collapse time, dependency on salinity water [17], [56]) and effective compressibility of the fluid start playing a role. Bredmose [20] showed that the Bagnold–Mitsuyasu scaling law can be applied to any situation in which all the kinetic energy within a certain fluid region goes into the compression of an air pocket, although this assumption may be questionable for hydroelastic impacts. For impact pressures of $P < 318$ kPa it was found that Froude scaling performed sufficiently, but when $P > 318$ kPa the Bagnold–Mitsuyasu approached the experimental results better. On the other hand, the Cauchy scaling law characterises the ratio of inertial forces in a fluid to elastic or compressive forces in a structure and may be related to the Mach number. The Cauchy number is expressed as:

$$Ca = \frac{\rho_f V^2}{K} \tag{2.19}$$

where K is the elasticity factor taking into account the compressibility of the mixture and is described as:

$$K = -\frac{dP}{dV/V_0} \tag{2.20}$$

With V_0 being the original volume and dV is the increase in volume due to aeration or compression. A higher K is equivalent to a stiffer medium, whereas a lower K is a more aerated and compressible medium.

Attili [37] found that in Wave–Flexible Structure Interaction (WFSI), additional scale effects emerge when the fluid and/or structural properties are improperly scaled. Their numerical results showed that for non-breaking wave impacts, no significant scale effects occur when the fluid properties remain unscaled while the plate properties are scaled. However, for breaking waves, scale effects in the pressures reached up to 132$\%$ due to the unscaled fluid properties. A new scaling approach was developed which includes factors such as the is the wave height, the water depth, and plate flexural rigidity in addition to the traditional Froude-Cauchy Scaling. In their findings the plate structural rigidity did improve the WFSI model. Nonetheless, even with these parameters the models did not capture the complex free water surface of the breaking wave observed for the prototype in detail. The shape, size and the pressures of the air pockets are also incorrectly scaled and the main differences concern the magnitude of the maximum peak, which was underestimated. The surface tension and air bulk modulus were overrepresented in the models, resulting in relatively smaller and stiffer air pockets at reduced scales. On the other hand, stronger turbulence was observed at a later stage with the resurfacing of the air pocket such that Reynold effects are expected to be more significant. Due to scale effects, converting different types of breaking wave impact loads to full-scale values may require separate scaling laws [20], [28]. This suggests that scaling parameters have a varying importance over different stages in time and space of breaking waves, and are relative to the scale.

2.5. Literature analysis

The literature indicates that aeration and air entrainment play a critical role in shaping wave impact pressures which may be related to Mach's number, where peak loads are most sensitive [20], [27], [28]. Hydroelastic effects are significant for short-duration, high-intensity events, with the ratio of impact duration to structural natural period being a key factor; this has been demonstrated in studies of wedge-shaped impacts penetrating the water surface [39], [40] and in freely floating structures impacted by breaking waves represented by using pendulum setups [9]. Experimental and numerical studies suggest that rigid structures do not necessarily experience the largest loads, as coupled fluid-structure dynamics, air entrapment, and wave overturning can amplify loads over time. While aeration can locally dampen peak pressures, it may increase the total loading duration due to extended contact times between the breaking wave and the structure [9], [31], [38]. Scaling introduces further complexity: while Froude's law captures global hydrodynamics in non-aerated flows, the presence of entrained air and unscaled fluid properties can produce significant discrepancies in impact pressures, requiring stage-dependent and separate scaling approaches for different types of breaking waves [17], [20], [37].

2.6. Knowledge gap

Despite considerable research on breaking wave impacts, the hydroelastic interaction between waves geometries and various cantilevered plate configurations in the spatio-temporal domain remains insufficiently understood. Existing studies on hydroelasticity predominantly study wedge-shaped models impacting still water, where boundary constraints at both ends and membrane effects restrict the plate's free response. Such constraints complicate the isolation of hydroelastic effects from other interacting phenomena.

Building on this, another important but underexplored aspect concerns the role of air entrapment and aeration during wave–structure interaction. The presence of entrapped air, which occurs when the wave approach angle is smaller than the plate inclination and creates a significant air cavity, can strongly influence peak pressures, contact durations, and force impulses during the initial impact stage. In contrast, aerated water alters the subsequent flow characteristics and dynamic loading throughout the impact process. A systematic experimental framework is therefore needed to quantify how these air-related effects interact with plate flexibility and plate-wave geometry. Controlled studies that isolate these mechanisms are particularly important for elastic plates, as they enable a more complete understanding of hydroelastic responses under realistic breaking wave conditions.

2.7. Research questions

Primary question:
How do hydroelastic effects influence the structure response during specific breaking wave type interactions?

Sub-questions:

1. What is the effect of the angle of the impact plate and shape of the wave at the moment of impact on the force, pressures and deflections measured on the plate?
2. What is the relationship between impact duration, wetted natural frequency, and structural response?
3. How does the presence of aerated water, causing the fluid to be compressible, influence the hydroelastic behaviour during wave impact?
4. How does the presence of entrapped air influence the hydroelastic behaviour during wave impact?

3

Methodology

The influence of various plate–wave configurations on the hydroelastic response can be examined through a combined numerical and experimental approach. First, ComFLOW simulations [57] provide a range of loads and visualisations of the waves, which inform the design of the experimental test setup. Then, the impacting waves can be studied using the experimental setup, offering a more realistic representation of actual waves at model scale. Finally, the results from the numerical simulations are compared with the experimental measurements.

3.1. Numerical Simulation

The ComFLOW model, which is a one-phase model that simulates fluid flow based on the Navier-Stokes equations, is used to simulate fluid behaviour in a sloshing tank, focusing on the interaction between fluid motion and the rigid overhanging plate. This two-dimensional model captures key parameters such as pressure distribution, forces acting on the plate, and fluid behaviour over time. The influence of air in the numerical model is neglected and hydroelasticity is not taken into account. The objective of using this model is to give a comparison between the values found from the experiment and numerical simulations. Additionally, it serves as an indication for the expected loads in the sloshing tank, on which the design of the experiment can be based. This analysis helps to identify patterns in how these factors influence one another and how the system responds dynamically to different sloshing frequencies. The output of the model provides an understanding of the fluid-structure interaction for rigid plates.The model will simulate the experiment, where a plate with a length of 200 mm is subjected to wave impacts created by sloshing oscillations at different frequencies, ranging from 0.85 up to 1.40 Hz. A time step of 0.005 seconds is used, simulating a total of 1-1.5 seconds depending on the sloshing frequency. Additionally, it records velocity and pressure at 200 specific points along the plate, spaced 1 mm apart, offering a sufficient resolution in space.

Figure 3.1: Comflow model layout: a) Volume aperture, b) Initial liquid fill ratio, c) Liquid fill ratio upon impact.

3.1.1. Mathematical model

The fluid motion in the sloshing tank is described by the Navier-Stokes equations. Since the tank is open, air can escape, making the assumption of single-phase flow more applicable in cases where aeration is minimal and air entrapment is avoided. The water in this two-dimensional model is considered to be an incompressible and viscous fluid, which simplifies the Navier-stokes equations. The parameters in the equations are described as follows: ρ stands for the water density, p the pressure, μ is dynamic viscosity, $u = (u, w)$ is the velocity vector, F represents for external forces such as gravity.

The conservation of mass is simplified to:

$$\nabla \cdot u = 0 \tag{3.1}$$

The conservation of momentum for the domain Ω with domain boundary $\delta\Omega$ is described as:

$$\frac{\delta u}{\delta t} + u \cdot \nabla u = -\frac{1}{\rho}\nabla p + \frac{\mu}{\rho}\nabla \cdot \nabla u + F \tag{3.2}$$

The boundary conditions at the domain boundary $\delta\Omega$ and free surface are needed to solve the Navier-stokes equations. At the walls of the sloshing tank, the aeration stones and the impact plate, no fluid should go through the boundaries. Therefore at these boundaries the following condition is applied:

$$\overrightarrow{u} \cdot \overrightarrow{n} = 0 \tag{3.3}$$

with $\overrightarrow{n}$ the direction perpendicular to the wall. The displacement of the free surface, when its position is assumed to be at $s(x, t) = 0$, is described by:

$$\frac{Ds}{Dt} = \frac{\delta s}{\delta t} + (u \cdot \nabla)s = 0 \tag{3.4}$$

This condition signifies that the free surface is a material surface, stating that fluid particles located on the interface remain on it throughout the motion and therefore no mass flux occurs across the free surface. Additionally, at the free surface there are boundary conditions required for the pressure and velocity, which follow from the continuity of normal and tangential stresses:

$$-p + 2\mu\frac{\partial u_n}{\partial n} = -p_0 + 2\sigma H \tag{3.5}$$

$$\mu\left(\frac{\partial u_n}{\partial t} + \frac{\partial u_t}{\partial n}\right) = 0 \tag{3.6}$$

Here, u_n stands for the normal component of the velocity, u_t is the tangential component of the velocity, p_0 is the atmospheric pressure, σ describes the surface tension and $2H$ denotes the total curvature.

The fluid in the sloshing tank exerts a pressure and shear force on the impact plate and the wall. In ComFLOW the shear force is neglected in the post-processing as it is typically much smaller than the pressure force. The pressure force is calculated along the boundary dS of the impact plate:

$$F_p = -\int_S p\overrightarrow{n} \quad dS \tag{3.7}$$

3.1.2. Numerical model

The fluid flow in the model is calculated using a Cartesian grid with staggered variables, where the pressures are defined in the cell centres and the velocity on the cell boundaries. With the introduction of the fluid, bodies and empty spaces, a difference in character is required in the numerical method by introducing edge and volume apertures. This results in the following geometry labels: a boundary (B), empty cells (E), surface cells (S) and fluid cells (F) , see Figure 3.2a. The distinction is recalculated and determined every time step before the Navier-Stokes equations are discretised in time and space.

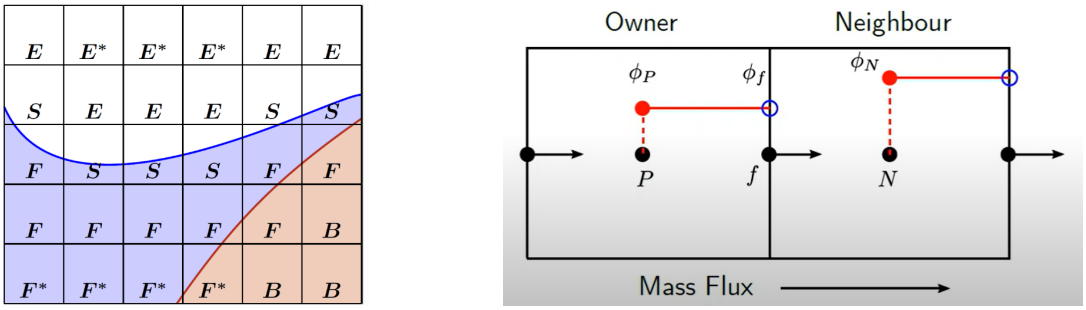

Figure 3.2: The numerical model in ComFLOW: (a) illustration of the cell labelling system [58], (b) representation of the upwind difference scheme.

For the time discretisation the first-order Forward-Euler method is used as it functions properly with stiff systems (the rigid impact plate) under the condition that very small time steps are used. The spatial discretisation is based on the finite volume method (VOF) and a first order upwind scheme which depends on the direction of the mass flux:

$$F_f = \rho_f A_f (U_f \cdot \hat{n}) \tag{3.8}$$

there $F_f < 0$ indicates the mass flow out of the owner cell into the neighbour cell and $F_f > 0$ indicates the mass flow into the owner cell. The value on the cell face is therefore related to the owner cell or neighbour cell depending on the direction of the flow [57]. This is particularly important because of the convection term in the Navier-Stokes equation. As the value on the cell face is constant between the cell centroid and the cell face, the upwind differencing is first-order accurate. This does mean that resolution is reduced and that the physics may not be correctly represented. However, with small enough time steps, it gives a stable and computationally efficient solution.

The time step is adjusted using the CFL-condition, which is the ratio between the fluid velocity components and the local grid spacing size multiplied with the current time step, meaning that the fluid must not propagate more than 1 grid cell per time step:

$$CFL = max_{i,j,k}\left(\frac{|u_{i,j,k}|\delta t}{h_{x,i}} + \frac{|v_{i,j,k}|\delta t}{h_{y,j}} + \frac{|w_{i,j,k}|\delta t}{h_{z,k}}\right) \leq 1 \tag{3.9}$$

If the computed CFL-number is larger than CFL_{max} the time step will be decreased, if the number is smaller than CFL_{min} during 10 successive time steps, the time step will be doubled.

3.1.3. Convergence study

Two types of convergence studies will be performed to ensure correct utilisation of the upwind discretisation scheme. First, a convergence study on the location of the monitoring points evaluates how the placement of monitoring points relative to the grid affects the solution. It ensures that the results are not artificially influenced by grid alignment or boundary discontinuities, confirming that the extracted data is representative and physically meaningful. Secondly, a grid refinement study assesses how the solution changes as the mesh is refined. The converging solution should show smaller differences

between successive mesh resolutions, up to the point where sufficient accuracy is obtained and the computational effort is not too elevated.

Location monitoring points

When using the upwind differencing scheme in CFD simulations, the location of monitoring points significantly affects the accuracy and convergence of the results. In this study, the computational grid was constructed such that it aligns precisely with the edge of the horizontal impact plate. However, placing monitoring points exactly on this boundary can lead to inaccurate or non-convergent results. This is because discretisation errors tend to arise at sharp material interfaces or boundaries.To evaluate this effect, two different monitoring point placements were considered:

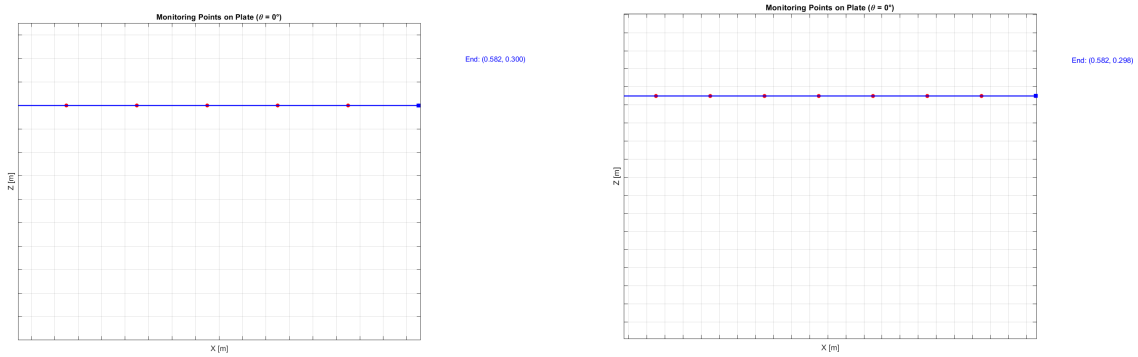

(a) **(b)**

Figure 3.3: Positioning of the monitoring points: (a) monitoring points on plate edge, and (b) monitoring points half a grid cell below the plate edge.

The resulting pressure signals over time are shown in Figure 3.4a and Figure 3.4b. When the monitoring points are located directly on the plate border, the pressure response shows exclusively negative pressure values. This behaviour occurs because the monitoring points are positioned at the interface where the physical conditions change abruptly. There is a hard transition from Body to Fluid cell. The interpolation across this discontinuity can be inaccurate. On the other hand, when the monitoring points are placed half a grid cell below the plate, the pressure displays both a descending and an ascending trend. This is because these points are located within the fluid domain away from the interface, allowing the solver to interpolate away from the boundary.

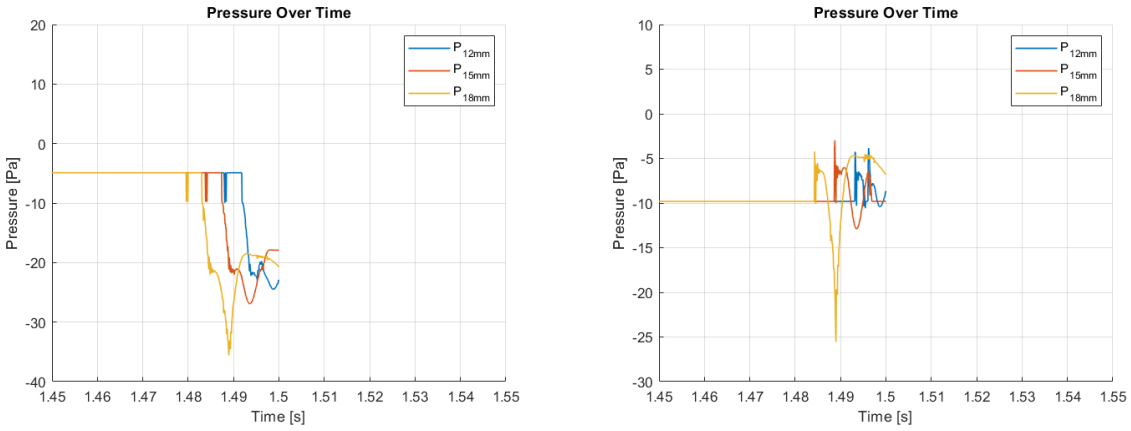

(a) **(b)**

Figure 3.4: Pressure time histories: (a) pressure output with monitoring points on plate border, (b) pressure output with monitoring points half a grid cell below plate border.

Although the behaviour of Figure 3.4b seems to be improved, the pressure before impact is negative. The hydrostatic pressure is given by $P = \rho g h$,where P is the pressure at depth h, ρ the density of the water, g is the acceleration due to gravity (9.81 m/s^2) and h represents vertical depth below the surface. The tank has been filled up to 200 mm. The hydrostatic pressure at this point should be equal to zero but shows -9.81 pa, meaning that the pressure values from ComFLOW must be corrected accordingly.

Grid refinement

The grid refinement study is performed to assess the sensitivity of the computed hydrodynamic forces to the grid resolution. The analysis focused on the most impulsive wave impact, characterised by a wave approach angle of $5°$ and a plate angle of $0°$. Three levels of grid refinement were examined, consisting of 292x160, 583x32, and 1166x640 cells respectively. Figure 3.5 presents the results of the convergence study, showing the temporal evolution of the impact forces for the three grid levels. A comparison of the results indicates that overall the grids behave similarly. However, the finer grids exhibit a higher level of numerical noise.

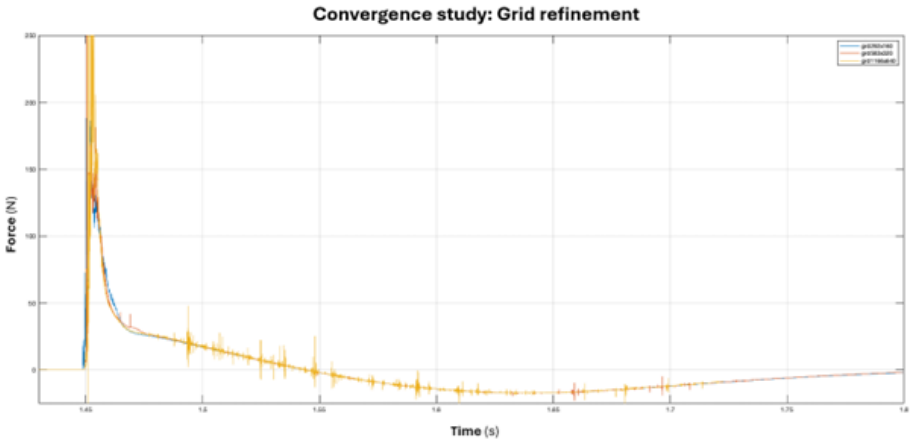

Figure 3.5: Convergence study of the computed force with respect to grid refinement.

Close-up views of the force signal (Figure 3.6a and Figure 3.6b) further illustrate the lack of convergence especially near the force peak. Due to the larger cell size of the coarser grid, the spatial averaging during integration is performed over a broader area. This averaging causes the computed force to start rising earlier, as the effect of the approaching wave front is spread over a broader region of the plate.

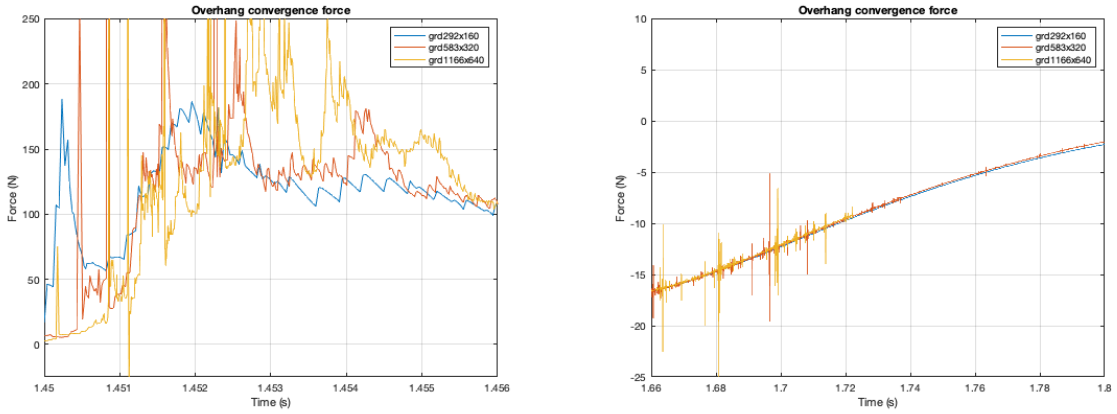

(a) **(b)**

Figure 3.6: Detailed views of the convergence behaviour: (a) near the force peak, and (b) in the force tail region.

The observed non-convergent behaviour at the force peak is likely related to the impulsive nature of the breaking wave impact, where small differences in the mesh resolution can significantly influence

the flow structure and pressure distribution on the plate. Consequently, additional grid refinement may be required to capture the true physical response, but could not be performed in within the time span of this thesis. Furthermore, comparison with the experimental data is necessary to validate the computed numerical force evolution.

3.1.4. Ramp up sloshing rig

To accurately model the ramp-up behaviour of the rig's electrical motor in ComFLOW, the motion characteristics of the tank are measured across different sloshing frequencies ranging from 0 to 2 Hz. The pulses of the motor are recorded over time, see Figure 3.7a. For this test, the tank was not mounted on the sloshing rig, which could influence the results since the inertia of the water is not accounted for. This approach is considered acceptable, as the additional power required to accelerate the water and tank is small relative to the motor capacity, and a frequency controller ensures stable operation.

The raw output signal exhibits noise, particularly in the upper and lower horizontal segments of the pulses. For the frequency analysis, the signal is converted into a binary format (Figure 3.7b) using a threshold value that distinguishes noise from the pulse data.

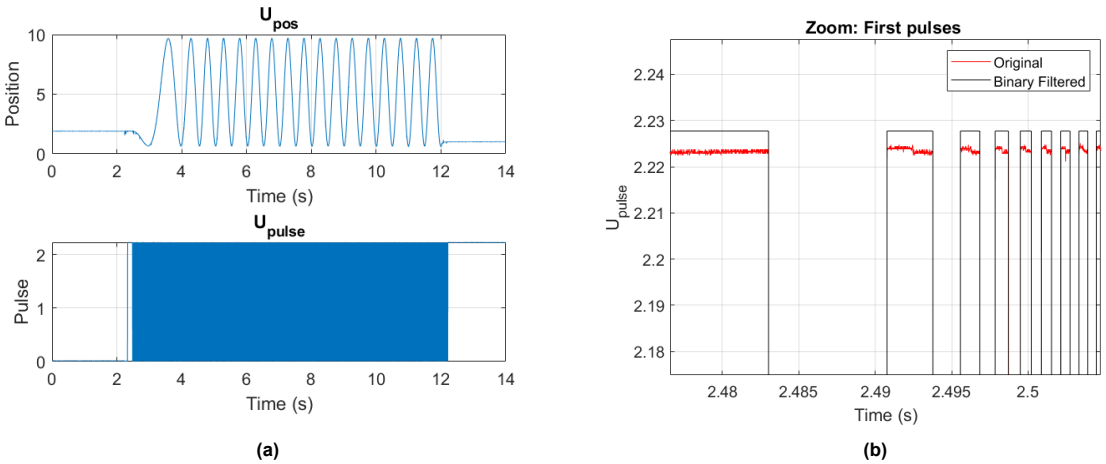

Figure 3.7: Position vs. motor pulse: (a) the raw signal from the sloshing tank position and motor pulse, (b) the original unfiltered pulse vs. the binary filtered pulse.

The differences between consecutive pulse edges give the time intervals between pulses, which is the inverse of the pulse frequency. The ramp up time is determined by interpolating between the first measured pulse and the start of the steady frequency region after the ramp-up, resulting in the desired sloshing frequency (Figure 3.8a).

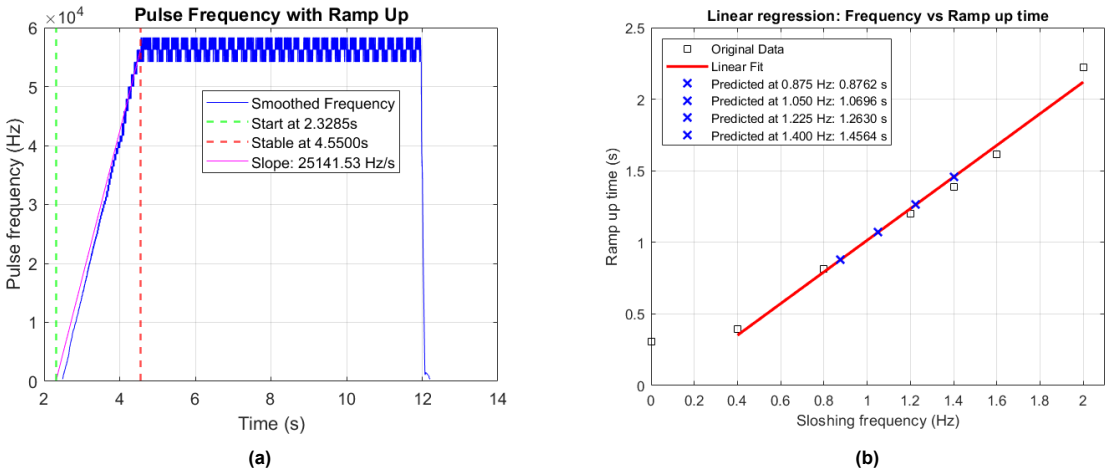

Figure 3.8: Tank sloshing frequency:(a) the frequency ramp up for a final sloshing frequency of 2 Hz , and (b) the interpolated ramp up for different sloshing frequencies.

The ramp up time, motor acceleration and pulse frequency plateau across different sloshing frequencies are described in Table 3.1. While the tank's pulse frequency and ramp-up slope show some variance, the ramp-up time increases linearly with frequency, with an R-squared value of 0.9888 indicating a highly consistent relationship. This is visualised in Figure 3.8b.

Input voltage turning knob	Sloshing frequency [Hz]	Stable pulse frequency [Hz]	Slope ramp up [Hz/s]	Ramp up time [s]
0.1	0	806	987	0.3091
2	0.4	10606	25758	0.3934
4	0.8	21667	25931	0.8165
6	1.2	32291	26572	1.1975
7	1.4	37500	26406	1.3900
8	1.6	43750	26762	1.6145
10	2.0	56250	25141	2.2215

Table 3.1: The ramp up time and slope across different sloshing frequencies.

For the ComFLOW wave simulations, the position, velocity, and acceleration of the sloshing tank must be determined for the selected sloshing frequencies, which correspond to the wave approach angles of interest. Seventh-order polynomial curve fitting is employed to smoothly ramp up the tank motion to the target sloshing frequency, following a method developed by PhD candidate M. Bockstael at TU Delft. These curves for are applied as boundary conditions in the ComFLOW model, leading to a more realistic prediction of the fluid behaviour and wave formation inside the sloshing tank.

3.1.5. Initial prediction loads

With the behaviour of the sloshing rig now accurately modelled, the expected load ranges are determines, see Table 3.2. These ranges are used as input for the design of the experimental setup regarding the choice of for example pressure sensors and load cells.

Table 3.2: The expected load ranges based on preliminary ComFLOW simulations.

Type	Range	Unit
Force	30-600	N
Pressure	0-400	kPa
Pressure rise time	0.00001-0.004	s
Velocity	4.7	m/s

3.2. Experimental setup

The interaction between breaking waves and flexible structures is highly complex and non-linear and is difficult to capture accurately using solely numerical simulations. To study the effect of hydro-elastic wave impacts in the spatio-temporal domain, the problem is simplified into a two-dimensional representation in space. This is achieved by making the dimension perpendicular to the wave loading significantly larger than the other dimensions, ensuring that variations in this direction have minimal influence on the system's response. To address how varying levels of aeration, in conjunction with wave shape and plate configurations, influence the measured impact pressures and flexible plate deflections, air bubble diffusers will be used in the setup.

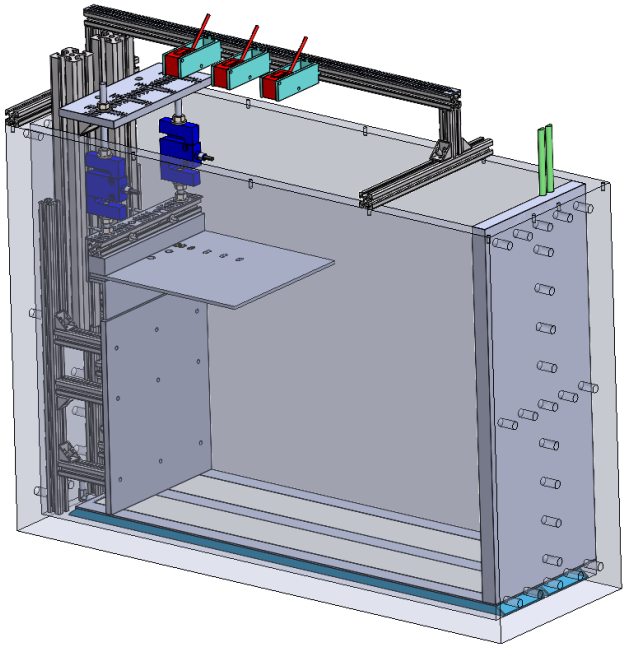

Figure 3.9: A CAD model of the experimental setup in the sloshing tank. The water height is measured using a water level gauge (green), plate deformation with laser distance sensors (red), the impact force with the load cells (dark blue), aeration is produced with air bubble diffusers (blue/white) and the impact pressure is measured with pressure sensors (yellow).

The sloshing rig is initially designed by Dr. Ing. S. Schreier and the current experimental setup is based on the design of ir. J. Bromlewe, for his thesis on "*Green water impacts on flexible breakwaters an experimental study*" [59].

Table 3.3: Tank parameters.

Parameters	Symbol	Value	Unit
Tank length bottom	L_t	583.2	mm
Tank length middle	L_t	584.0	mm
Tank width bottom	W_t	199	mm
Tank width middle	W_t	200	mm
Tank height	H_t	496	mm
Relative plate height	H_p	307	mm
Plate density (RVS)	ρ_p	8000	kg/m^3
Youngs Modulus (RVS)	E_p	$193 \cdot 10^9$	Pa
Relative still water level	H_w	145	mm
Fluid natural frequency	ω_{n1}	0.935	Hz
Max amplitude	$a_{t,\text{max}}$	60	mm
Tank start position	x_0	+50	mm
Max sloshing frequency	$f_{t,\text{max}}$	2.0	Hz

Note that the width of the impact plate assembly is set at 199 mm to prevent damage to the perspex sloshing tank and make installation of the sub-assembly less restricted. As a result, small amounts of fluid may pass the border of the plate during testing. The tank will return its motion (direction towards negative amplitude) from the starting position at +50 mm. The relative still water level and plate height are the distances from the top of the aeration stones, and not the bottom of the tank. The natural frequency of the fluid in the tank is described in Table 3.3 and calculated from Equation 2.17. It must be noted that there is an approximated 2mm difference in height between the top of the bottom plate and the aeration stones.

3.2.1. Wave generation

A wave front will be generated in the sloshing tank. The wave is considered uni-directional and spans the full width of the tank, resulting in a loading pattern that is as symmetric as possible. Only waves that create high enough impact which are relevant for hydroelastic analysis (based on the model of Faltinsen [39]) should be established. The experiment in the sloshing rig offers a controlled and repeatable environment to study these interactions in detail.

The sloshing rig moves horizontally at a frequency *f* with an amplitude *a*. The run up is wedge shaped representing a propagating wave having a characteristic velocity, wave tip width and approach angle varying with the alternating sloshing frequency of the tank. These characteristics may be sliglty variable in space and time, especially with the introduction of aeration as is described in Appendix B. In Figure 4.8b a schematic close-up of the wave tip is shown, where the fluid near the wall is propelled by the wave itself resulting a a slight run-up along the wall. To determine the approach angle of the incoming wave, the linear wave section is used as the reference surface.

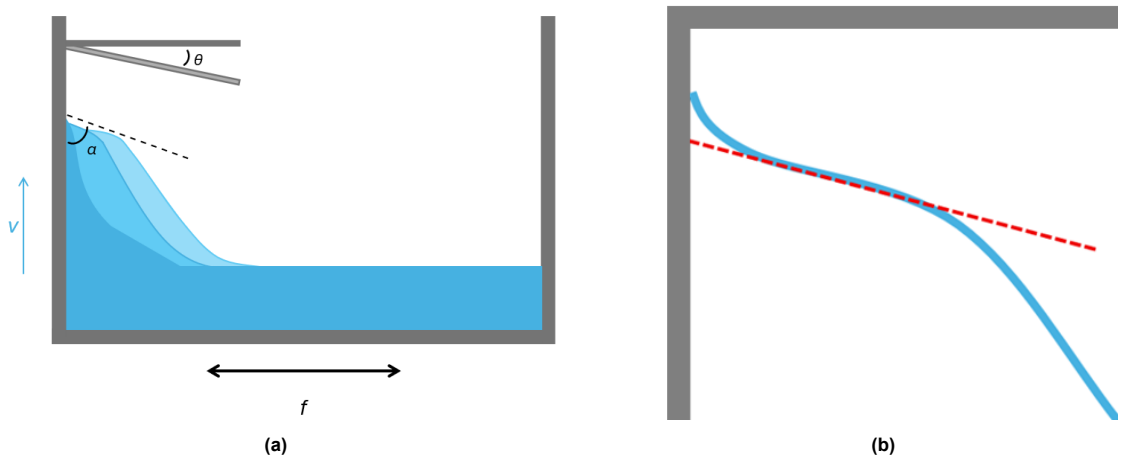

Figure 3.10: Sloshing rig characteristics: (a) Schematic representation of the experimental setup in the sloshing rig and adjustable variables, (b) close-up view of the wave shape near the wall, with the wave approach angle approximated by the section indicated with the red line.

To verify the integrity of the test setup at higher frequencies, the sloshing frequency will be gradually increased in trial runs, as higher frequencies are known to induce greater loads on the system.

3.2.2. The impact plate assembly

To investigate the effect of hydro-elasticity, four impact plate thicknesses are used, ranging from rigid (4 mm) to highly flexible (0.5 mm). The plate angle, θ, can be adjusted using clamping blocks with different inclinations. These blocks are secured with bolts, allowing plates of varying thicknesses to be mounted, while any gap created by thinner plates is filled with shim plates to maintain correct alignment. By comparing the pressures, forces and deflections measured on the flexible plates with those obtained from the rigid plate, the degree of hydro-elastic behaviour can be assessed.

In the previous setup the load cells were mounted separately to the profiles of the sloshing rig, see Figure 3.11a, which made the installation more complex and required additional adjustments. To reduce

these inaccuracies and decrease the installation time, a mounting plate for both load cells is designed, including tolerance marks (Figure 3.11b) to facilitate replicable positioning of the parts.

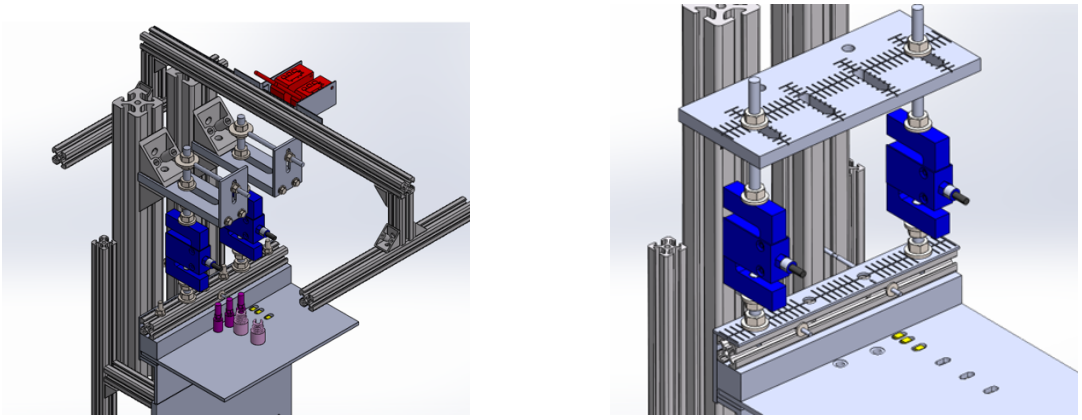

(a) (b)

Figure 3.11: The sub-assembly: (a) the previous setup with mounts for each load cell, (b) the new setup where the load cells are mounted on marked plates to ensure accurate positioning.

Due to the increase in sloshing frequencies, the wave shape changes and a larger wave front is created. As a result, the plate length needs to increase from 100 to 200 mm to be able to interact with the entire wave front. Because of the increased length and larger wave front, the moment on the plate increases, which requires reinforcing the impact plate assembly. The rear supporting plate is therefore increased from a 2 to 5 mm thickness, see Figure 3.12a.

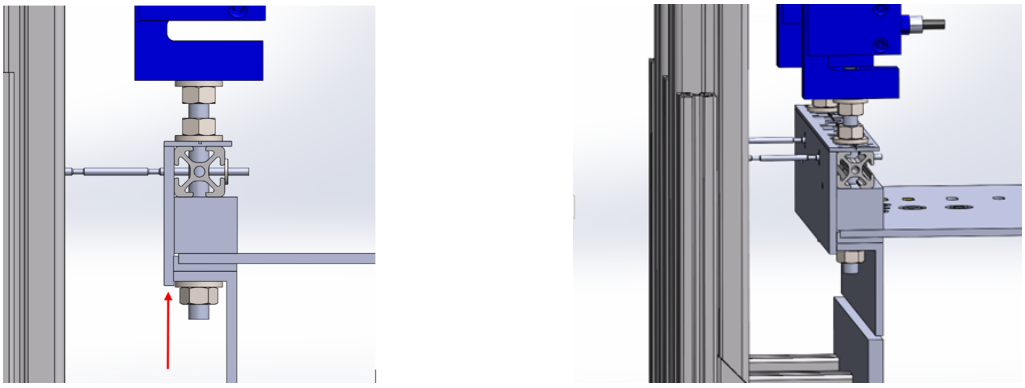

(a) (b)

Figure 3.12: Sub-assembly details: (a) increased thickness of the rear supporting plate (see red arrow) due to the increased moment on the impact plate, (b) increased rotational stiffness around the z-axis to ensure two-dimensional behaviour.

3.2.3. Controlling aeration

The level of aeration in the fluid can be controlled using a flow system controller which is connected to the valve controlling the input of the Pentax DYPFP24 Micro-bubble air diffusers, which have a maximum flow capacity of 7 liters per minute, or 345 kPa. The level of aeration is measured using an aeration float as is described in section A.6. To ensure repeatable experimental results, it is essential to maintain boundary conditions that minimise interference with the natural fluid motion. For this reason, a flat plate with openings for the aeration stones is used for the bottom surface.

By observing the change in water level, one can estimate the distribution between the air and water volume assuming that the conservation of mass is valid, see Figure 3.13. This means that no air will leave the system at any other place than at the free surface.

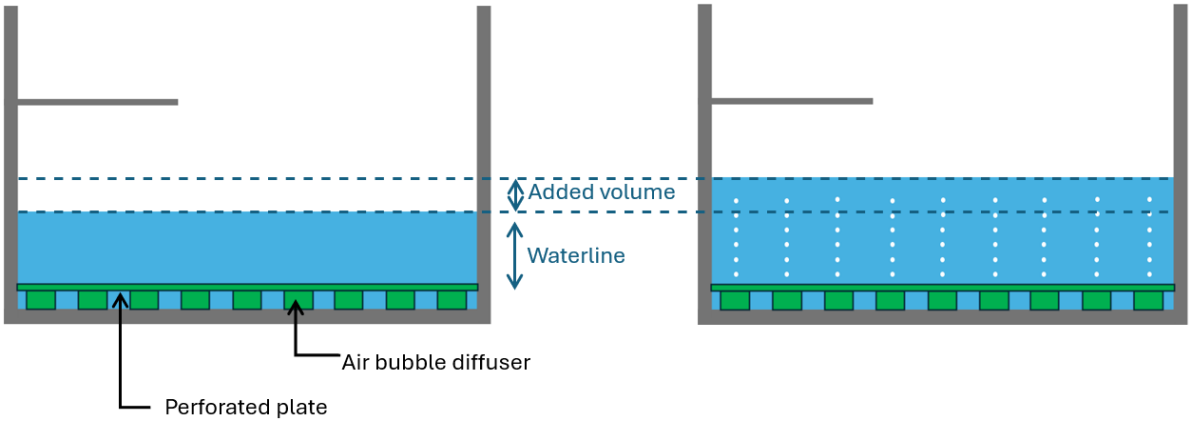

Figure 3.13: Schematic representation of the experimental setup in the sloshing rig including the air bubble diffusers and a perforated plate. The addition of air bubbles increases the volume and water level.

The aeration stones generate a flow within the tank, resulting in fluctuations of the free water surface level, as illustrated in Figure 3.14. Nevertheless, the mixture appears to remain relatively homogeneous in the region near the impact wall and plate. For future experiments, it is recommended to install a separating wall on the opposite side of the tank to ensure a more homogeneous mixture in the flow impacting the plate.

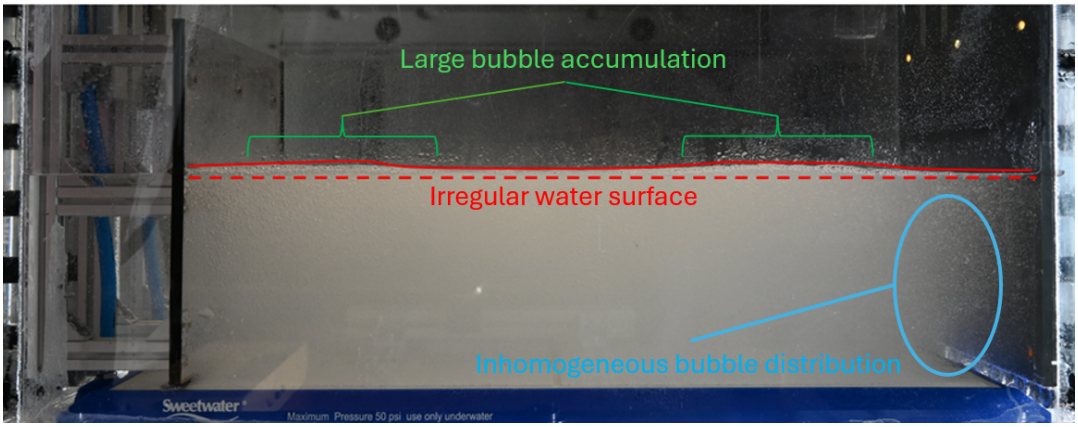

Figure 3.14: The resulting flow behaviour upon aeration.

3.2.4. Sensors

The loads on the plate will be measured using pressure sensors and load cells. The impact loads vary along the length of the plate; since the location of the peak pressure shifts with increasing sloshing frequency, pressure sensors must be distributed across the entire plate. Pressure sensors will only be placed on the rigid 4mm plate as sensor readings are influenced by local deformation of the elastic plates and vice versa. By mounting sensors on an elastic plate its stiffness and mass distribution as well as the natural frequencies and vibration modes are affected. Besides measuring the local pressures, the total load is also be examined. As a result, all the added equipment influences the response of the setup. A sufficient amount of sensors must be placed to ensure a high resolution, while at the same time they may not interfere with the system's accuracy.

Table 3.4: Overview sensors.

Sensor function	Model	Quantity	Operating range	Max range	Non-linearity
Pressure	SMI 5420E-30-AHS	6	207 kPa	621 kPa	± 0.34 %
Pressure	PCB 113B24	3	6895 kPa	13790 kPa	± 0.55 %
Impact load	Zemic H3	2	50 kg	75 kg	± 0.15 %
Plate distance	Panasonic HG-C1400	3	200–600 mm	–	± 0.30 %
Tank position	WayCon LZW-M	1	120 mm	–	± 0.02 %

Load cells

Two load cells are used to measure the total load acting on the impact plate. Their placement is designed to provide sufficient rotational stiffness of the system. To quantify the vertical load on the impact plate, Zemic-H3 load cells are calibrated according to the load range established in subsection 3.1.5. Although the load cells primarily measure the vertical component of the impact force, the moment applied to the plate can influence the measured vertical load, which depends on the specific plate and wave configurations as described in section A.1. To allow for the displacement of the load cells upon and after impact, a gap of 1mm is maintained between the bottom vertical wall and vertical wall of the impact plate assembly as is shown in Figure 3.15.

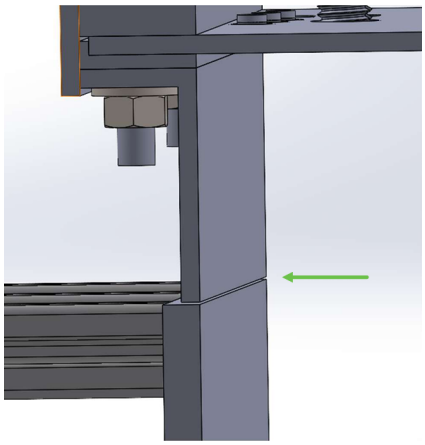

Figure 3.15: A gap designed to allow for the load cell's oscillation response during and following impact.

Pressure sensors

Two types of pressure sensors are used to enable verification of the pressure response and peak pressure at different locations along the plate. The precise spacing of the pressure sensors (Figure 3.17) is determined based on the results of initial ComFLOW simulations.

To investigate the pressure behaviour, piezo-resistive sensors are implemented. This type of sensor can measure both static and dynamic pressures by detecting changes in electrical resistance that occur when the sensing diaphragm undergoes mechanical deformation. For this purpose, the SMI 5420E-30-AHS sensors were selected. They feature an operating pressure range of 0–30 PSI and a maximum (proof) pressure of 90 PSI. The sensor combines MEMS piezoresistive sensing with integrated signal-conditioning electronics that perform temperature and offset compensation, providing a stable and linear output suitable for both static and moderately dynamic measurements.

In addition, piezoelectric sensors are used to capture rapid pressure peaks. These sensors are recommended for high-frequency measurements due to their fast response times [52]. Their high natural frequencies help prevent resonance effects associated with wave interactions or entrapped air bubbles,

enabling accurate detection of sharp pressure peaks during impact events. Accordingly, PCB 113B24 piezoelectric sensors are used to identify pressure peaks during wave impacts. However, it is important to note that piezoelectric sensors are limited to measuring dynamic pressures and cannot record static or slowly varying loads due to the inherent signal decay.

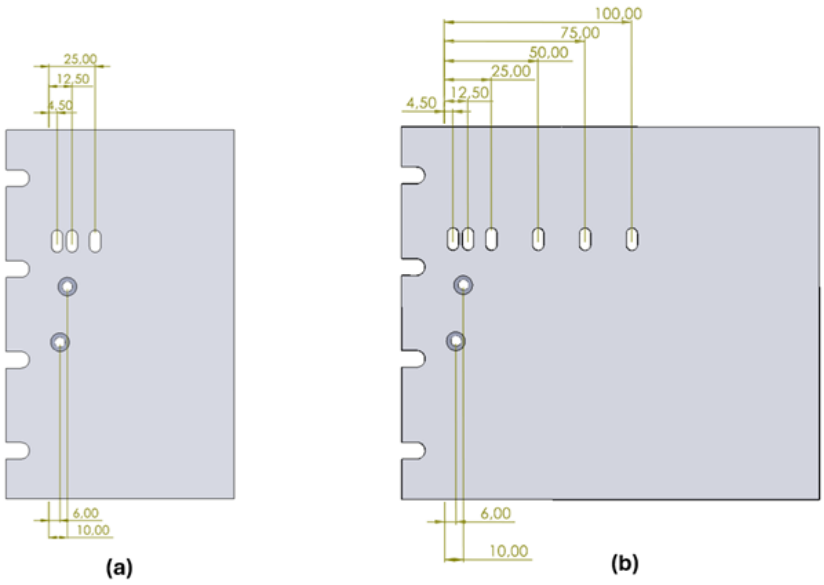

Figure 3.16: Location of the pressure sensors (from left to right): for the 100 mm plate (a): SMI7, SMI8, SMI9; and for the 200 mm plate, (b): SMI1, SMI2, SMI3, SMI4, SMI5, SMI6. PCB1 and PCB3 are interchanged between the two plates.

Distance sensors

The deformation of the elastic plates is measured using three Panasonic HG-C1400 laser distance sensors with ID numbers 169,170 and 171. Laser 169 is measuring at 50mm from the wall, laser 170 measures at 100mm from the wall and laser 171 measures approximately at the wave tip. Because of changes in the plate angle, the exact positions of the laser 171 measurements on the plate will vary.

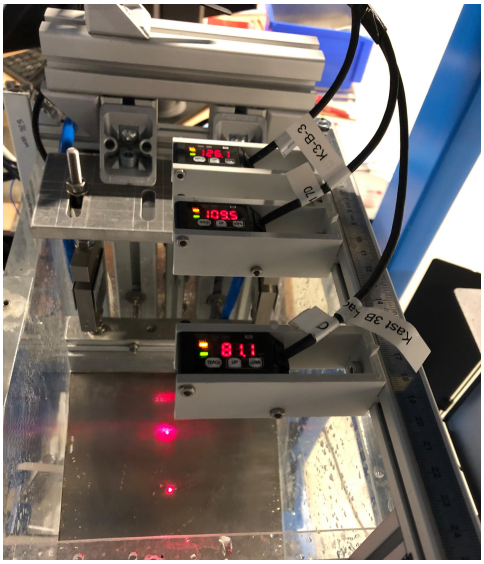

Figure 3.17: Positioning of the lasers distance sensors in the setup for measuring the plate deflection upon wave impact.

The sloshing tank will accelerate towards the desired frequency and is influenced by factors as break release and inertia of the tank. The position and acceleration of the tank will be measured by a linear Waycon position sensor. The measured position can then be used as input for numerical simulations.

Wave gauge

The water level is tracked using a water level height sensor. An in-house capacitive wave gauge made of two parallel stainless steel strips is used to reduce flow disturbance in the tank. A voltage is applied to one strip, and the circuit closes through the water. As the water level rises, the circuit shortens, lowering resistance and increasing output. The sensor linearity depends on strip alignment. Because the tank is open, there is a possibility of water droplets leaving the tank, and all test equipment including the supported plate need to be cleaned after each test to ensure a consistent starting point. The water level in the tank is kept constant. As a result, the level of the water needs to be filled up to the original level after each test using a syringe.

High speed camera

Two high-speed cameras are used in the experimental setup to capture different aspects of the wave impact dynamics. The first camera records the velocity and wedge angle of the wave during impact. The second camera is positioned at an angle beneath the impact plate to visualise the hypothesised formation of cavitation. This second camera is used for imaging purposes only and does not contribute to quantitative measurements due to distortions caused by the mirror and refraction effects as light passes through the water. These distortions can alter the apparent shape and position of objects, limiting the accuracy of any measurements derived from the images.

Both cameras are Photron FASTCAM SA-Z models operating at 20000 frames per second (fps). Due to differences in lighting conditions, the shutter speeds of the two cameras may vary. However, they are calibrated to run at the same frame rate, ensuring temporal alignment. This synchronisation allows for precise comparison of the cavitation imagery with the corresponding load peaks detected by the sensors.

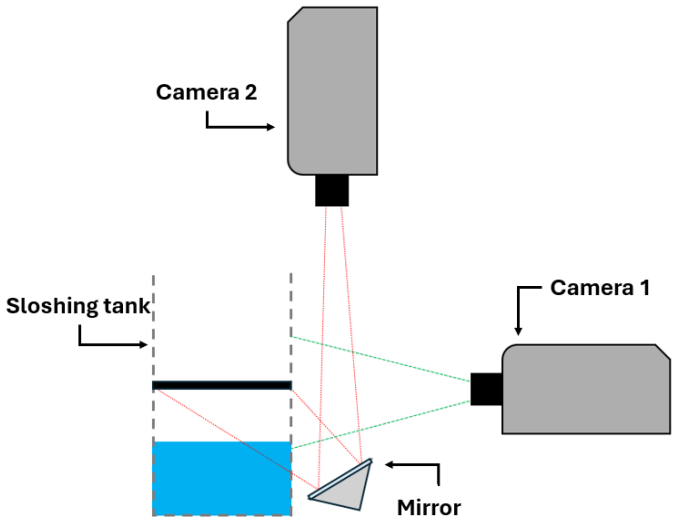

Figure 3.18: Setup of the two high-speed cameras: Camera 1 measures the wave impact, Camera 2 visualises the formation of cavitation.

3.2.5. Data acquisition

To retrieve the information from the camera, sensors and load cells, a data acquisition system (DAQ) is needed to record the data and video images. The DAQ used for the force, pressure, deflection and tank position measurements has a maximum sampling rate of 100 kHz, and based on Nyquist–Shannon sampling theorem [60] this means that reconstruction of the output signal of the channels is guaranteed for a bandlimit half this frequency. An additional DAQ measuring with a frequency of 10 kHz is used for measurements that require less accuracy, such as the wave gauge and air flow. A trigger signal based

on the first motor pulse sends a signal once the sloshing rig starts to move. Subsequently, the data is saved some time before and after the trigger signal.

The interface scheme presented below provides a comprehensive overview of the experimental setup and illustrates how the various components are interconnected through the different data acquisition systems. It shows the signal pathways between sensors, actuators, control hardware, and data acquisition devices.

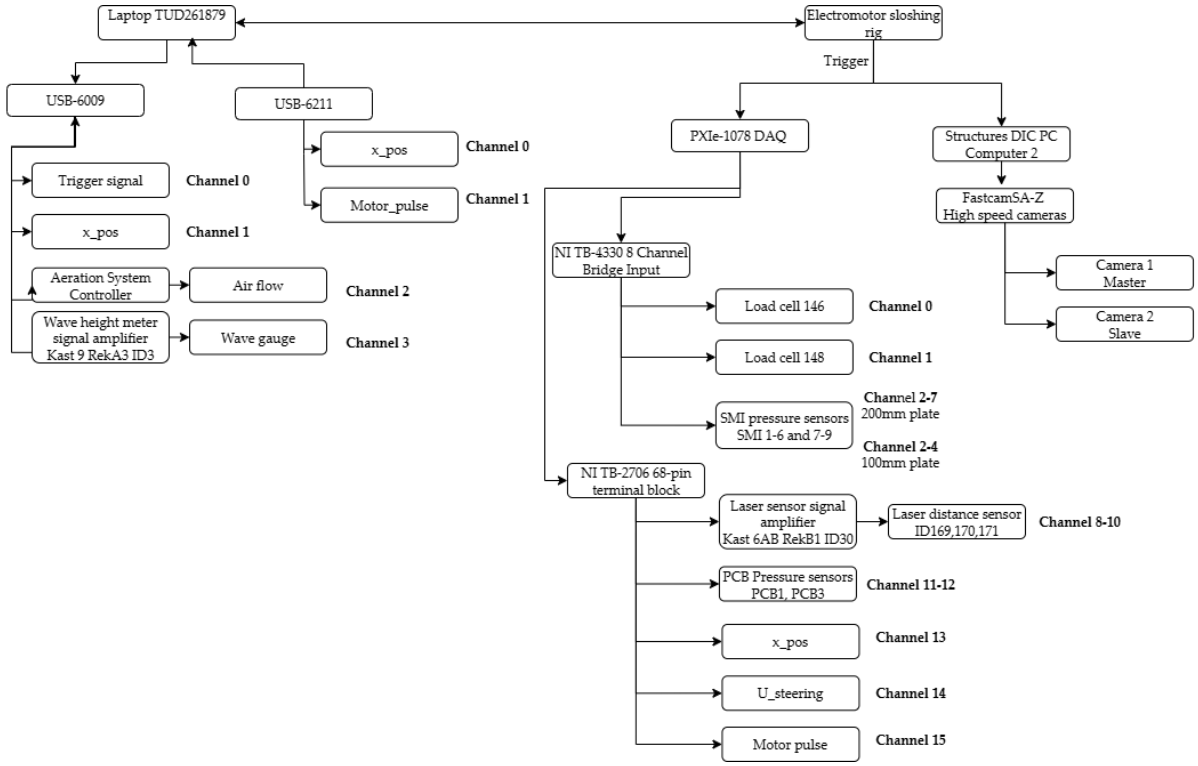

Figure 3.19: Interface scheme of the instrumentation.

3.2.6. Introduction dimensionless number

In a similar approach to the dimensionless number ξ introduced by Faltinsen [39] described in Equation 2.9, an adapted version is required which facilitates a comparison to other hydroelastic cases.

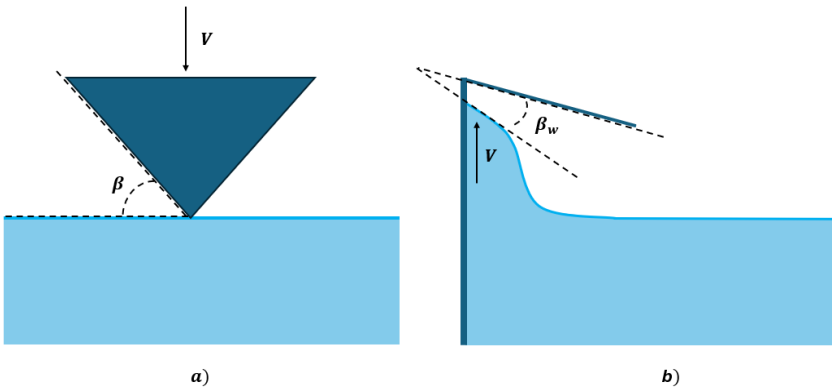

Figure 3.20: Definition of the dimensionless number: (a) the setup of Faltinsen [39], and (b) the current setup.

The parameter ξ presented in Equation 2.9 should be evaluated in order to adapt the parameter from slamming to wave impacts. In the numerator, $\tan(\beta)$ represents the geometric influence on the hydro-

dynamic impact. The rate of increase of the wetted length depends on the slope of the wedge and tan(β) captures the flow expansion in all directions. The denominator captures the inertial and elastic response of the structure and the fluid and reflects the relative importance of fluid inertia versus the structural stiffness. According to Faltinsen, when ξ is much greater than 1.5, the impact behaves like a rigid-body slamming event with negligible structural deformation. When ξ is around 1.5, hydroelastic effects begin to emerge, altering the pressure distribution and wetted region. For values of ξ significantly less than 1.5, the structural flexibility plays a dominant role in the impact response, indicating strong hydroelastic behaviour.

A key distinction between the setup used by Faltinsen and the present experiment lies in the boundary conditions of the impacted plate. In Faltinsen's model, the plate is clamped at both ends, constraining both rotation and in-plane displacement. This constraint induces in-plane membrane tension during deformation, thereby increasing the plate's stiffness and affecting its dynamic response. Consequently, the plate's response to hydrodynamic loading is governed not only by bending but also by axial tension, leading to altered deformation patterns and mode shapes. In contrast, the plate in the current flip-through wave setup is cantilevered: being fixed at one end and free at the other allowing for larger bending deformations and resisting less to transverse motion. To account for these differences, a modified form of the dimensionless parameter may be introduced which includes an correction factor κ representing the influence of boundary conditions:

$$\xi^* = \frac{\tan(\beta_w)}{V\sqrt{\rho L^3/(\kappa EI)}} \tag{3.10}$$

In this expression, β_w is the relative angle between the wave front and the plate (analogous to the deadrise angle), see Figure 3.20. The coefficient κ reflects the reduction in effective stiffness and altered modal response associated with the cantilevered boundary condition.

Together with the alternative approach of Bereznitski [40] described by Equation 2.10, the introduction of the parameter β_w enables a more meaningful comparison between the current wave impact experiments and earlier hydroelastic studies, providing a dimensionless basis for evaluating the hydroelastic effects across varying structural configurations.

3.2.7. Test matrix

The test matrix for this study is designed to systematically investigate the impact of waves on a plate under a wide range of physical conditions. With 4 different plate thicknesses, 4 wave approach angles, 4 plate angles and 4 aeration conditions a total of 256 unique test cases are created. The plate thicknesses are chosen based on the ratio between the impact period and the first natural period of the plate as defined by Bereznitski [40]. To ensure sufficient reliability of the results, each test case will be repeated three times as described in Appendix B. Additional calibration and control tests will be conducted to validate measurement consistency and system performance for a comparison to Bromlewe's results [59]. For a sloshing frequency of 0.823 Hz, the experiment is performed with a plate length of 100 mm (equal to the one used in Bromlewe's experiment) and with a plate length of 200 mm as calibration and comparison to the previous plate length.

Table 3.5: The test parameters for the experiment in the sloshing tank.

Plate Thickness (mm)	Wave Approach Angle (°)	Plate Angle (°)	Aeration Percentage
4.0	0	0	0%
1.5	10	10	1%
1.0	20	20	2%
0.5	30	30	4%

Plate natural frequencies

The first dry natural frequency of the experimental plates is identified using a free decay test, with the tip motion measured by laser distance sensor 171. By placing the plate in the sub-assembly and exciting it with a short impulse, such as a hit with a hammer, the plate will vibrate. By plotting the measured signal of the lasers, the experimental natural frequency of the plate can be approximated. Subsequently, to predict the wetted natural frequency of the plate (assuming a full wetted length) to study the effect of added mass, the water level is raised to exactly the height of the plate such that the bottom side of the plate is in contact with the water surface. Again, the plate is excited with a short impulse and the natural frequency is retrieved from the signal of the laser distance sensors.

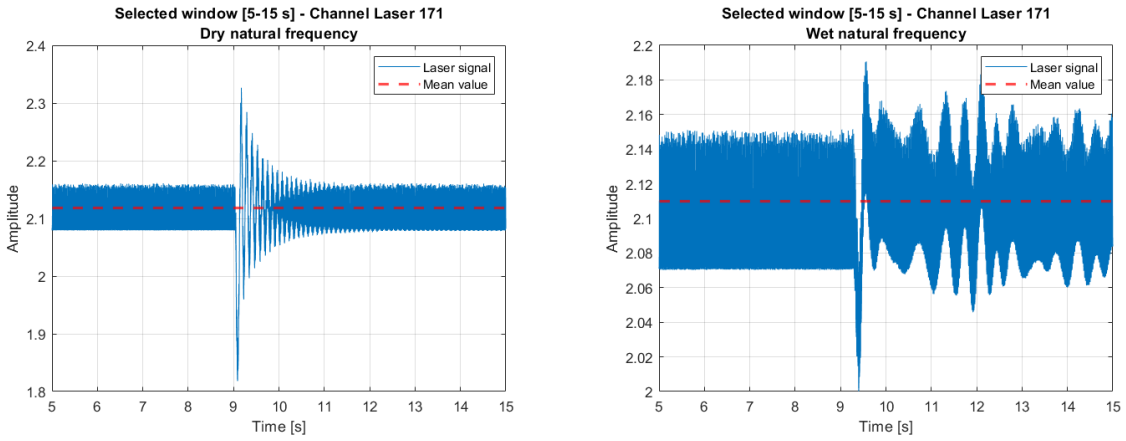

Figure 3.21: Excitation of a 0.5 mm plate: (a) response of the dry plate, (b) response of a wetted plate.

As can be noticed from Figure 3.21b and Figure 3.21a, there is a large difference in the response after initial excitation. This is due to the fact that upon excitation, where in Figure 3.21a both the plate and the water have a response, resulting in a continuing motion of the plate. For that reason, only the first period of the excitation is used to approximate the wetted natural frequency.

To verify the values of natural frequencies found during the free decay test, a comparison is made to an analytical approximation. The plate can be approximated by a 2D-beam model. The natural frequency of a cantilevered beam can be approximated by and have been determined analytically based on the Euler-Bernoulli beam theory:

$$f_{n,beam} = \frac{1}{2\pi}\frac{1.875^2}{L^2}\sqrt{\frac{EI}{m}} = \frac{1.875^2}{2\pi\sqrt{12}}\frac{t_p}{L_p^2}\sqrt{\frac{E}{\rho_p}} \tag{3.11}$$

with $I = \frac{b_p t_p^3}{12}$ being the moment of inertia. This means that the natural frequency of the plates is proportional to the following:

$$f_n \propto \frac{t_p}{L_p^2} \tag{3.12}$$

To accommodate the different wave approach angles by doubling the length of the impact plate, the plate thickness must be reduced to one-quarter. The resulting computed natural frequency of the plates are presented in Table 3.6. The experimental values of the natural frequencies for the plate length of 100mm are taken from Bromlewe [59]. The error is calculated as the difference between the measured dry natural frequency f_{n1m} and the analytical dry natural frequency f_{n1a}.

Table 3.6: Natural frequencies of the plates with varying lengths and thicknesses.

Plate Length [mm]	Plate Thickness [mm]	$f_{n1a,\mathrm{dry}}$ [Hz]	$f_{n1m,\mathrm{dry}}$ [Hz]	$f_{n1m,\mathrm{wet}}$ [Hz]	Error $f_{n,\mathrm{dry}}$ [%]
100	0.4	33.2	32.0	-	3.61
	0.5	40.3	40.0	-	0.74
	0.6	48.3	51.3	-	-6.21
	1.0	80.5	76.5	-	4.97
	4.0	322.0	-	-	-
200	0.5	9.88	8.63	2.46	12.65
	1.0	19.77	19.23	8.77	2.73
	1.5	29.65	27.30	11.63	7.92
	4.0	79.06	-	-	-

Test sequence

Each experiment follows a standardised test sequence described by the scheme presented in Figure 3.22. The total measurement duration on the laptop at 10 kHz is 15 seconds. The measurement is started manually on the laptop and is not synchronised with the trigger. This duration provides sufficient time to activate all controls before and during the measurement. The fast data acquisition measuring with 100 kHz, is triggered automatically with data recorded from 1 second before to 3 seconds after the trigger. This approach ensures that sufficient data around the event is captured while avoiding excessive storage requirements.

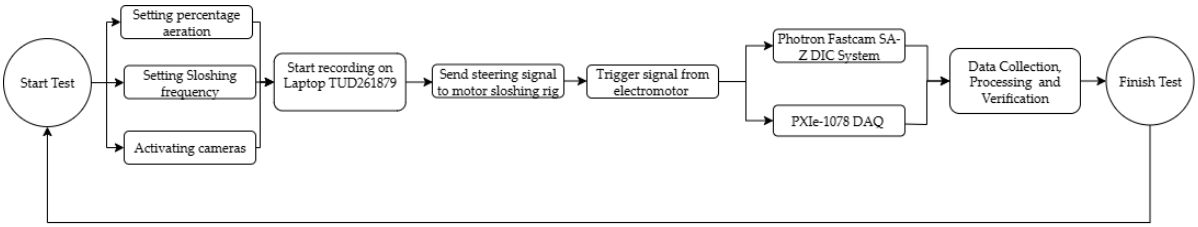

Figure 3.22: Scheme of the test sequence.

3.2.8. Signal processing

The raw measurements obtained during the wave impact experiments include not only the structural response but also background noise and high-frequency disturbances. Attention is required because filtering may suppress important features of the signal.

To address this, a low-pass Butterworth filter is applied to reduce noise while preserving the lower frequency content relevant to the plate dynamics. The plate motion is primarily governed by its natural vibration modes, which typically occur at lower frequencies depending on the plate geometry and loading conditions. The filter is applied only to the laser distance measurements, which exhibit significant noise, and to the force signals to determine mean values for identifying the start of the rise time.

4

Results

This chapter presents the numerical and experimental results of the study on breaking wave impacts and hydroelastic interaction. The experimental data are first introduced to describe the observed impact pressures, forces and structural responses, followed by a comparison with the numerical observations.

4.1. Experimental results

The study investigates how plate rigidity and inclination, aerated water and large air entrapment, and the wave shape affect the impact dynamics in the spatio-temporal domain. Key response parameters include maximum pressure, rise time, plate deformation, the total impact force, impact duration and added mass effects. All signals are aligned relative to the second edge of the motor pulse which is one pulse after the trigger signal. It was found that the duration of the initial motor pulse varies, whereas the ramp-up phase of the second pulse remains constant.

4.1.1. Generated waves

In Figure 4.1 the wave approach angles are shown as a result of their corresponding sloshing frequency of the tank for a plate angle of $0°$. The wave approach angle of $0°$ was not attainable with the current settings of the sloshing tank. When the resulting wave approach angles are larger than the plate angle ($\beta_w < 0$), air entrapment occurs in the corner between the vertical wave and the impact plate. In Figure 4.2a the resulting wave approach angle is plotted against the sloshing frequency.

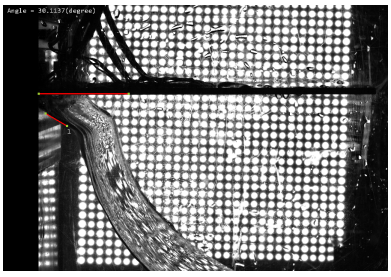

(a) 30° wave approach angle, 0.85 Hz

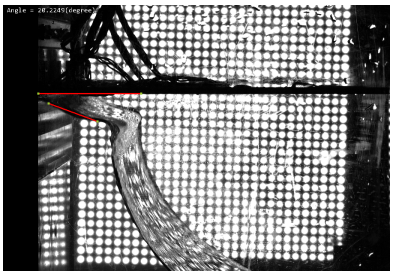

(b) 20° wave approach angle, 1.00 Hz

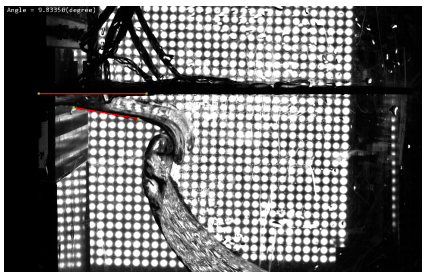

(c) 10° wave approach angle, 1.15 Hz

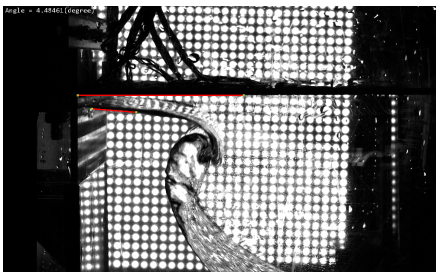

(d) 5° wave approach angle, 1.40 Hz

Figure 4.1: Resulting wave shapes for different wave approach angles and sloshing frequencies: (a) 30° at 0.85 Hz, (b) 20° at 1.00 Hz, (c) 10° at 1.15 Hz, and (d) 5° at 1.40 Hz.

The wave velocity is calculated based on the high-speed camera images, where the number of pixels per frame is converted to the velocity in m/s, see section A.7 for the approach. The wave velocity appears to be slightly affected by the presence of air in the fluid (Figure 4.2b); with increasing aeration the velocity decreases. The difference between non-aerated and aerated water is more pronounced at smaller wave approach angles, where the velocity is higher and may induce greater flow disturbances. This decrease in the wave velocity is likely due to the reduced effective density and increased compressibility of the air–water mixture. Since aeration reduces the velocity of the wave, also the wave approach angle is slightly changed.

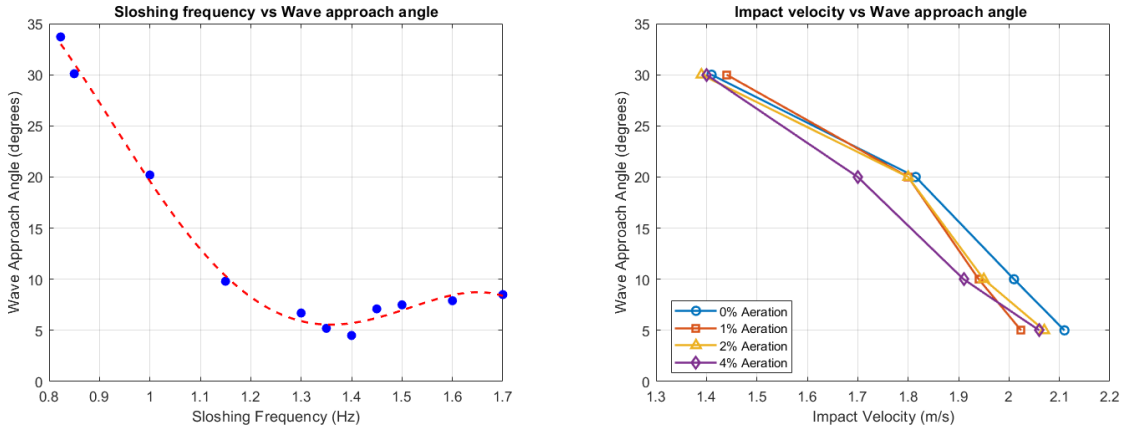

Figure 4.2: Wave characteristics for different sloshing frequencies: (a) the resulting wave approach angles for a range of sloshing frequencies, (b) the impact velocities approximated from camera images for different sloshing frequencies and percentages of aeration.

Based on the wave velocities presented in Figure 4.2 the Mach number described by Equation 2.5 can be approximated for the different levels of aeration. The results are presented in the Table 4.1, where an increasing Mach number is found for decreasing wave angles and increasing levels of aeration.

Table 4.1: Flow velocities, mixture speed of sound, and Mach numbers for different aeration levels and wave approach angles

Wave angle [°]	Aeration [%]	Wave velocity [m/s]	Speed of sound [m/s]	Mach number [-]
30	0	1.41	1481.	0.001
	1	1.44	120.4	0.012
	2	1.39	85.70	0.016
	4	1.40	61.27	0.023
20	0	1.81	1481	0.001
	1	1.80	120.4	0.015
	2	1.80	85.70	0.021
	4	1.70	61.27	0.028
10	0	2.01	1481	0.001
	1	1.94	120.4	0.016
	2	1.95	85.70	0.023
	4	1.91	61.27	0.031
5	0	2.11	1481.	0.001
	1	2.02	120.4	0.017
	2	2.07	85.70	0.024
	4	2.06	61.27	0.034

4.1.2. Pressure: effect of relative angle, plate rigidity and aeration

The pressures were measured using the SMI pressure sensors positioned as described in Figure 3.17. The sensor positioning has a significant influence on the measured pressures, as local pressure effects occur along the entire plate length. Locally entrapped air and minor disturbances of the free water surface, such as those caused by airflow or falling droplets, can also affect the measured pressures. Figure 4.3a is showing the difference in impact time and pressure behaviour at SMI1 for different wave approach angles. Larger wave angles with lower velocity impact the pressure sensor later in time with respect to the smaller wave angles with higher approach velocities. The effect of aeration is shown in Figure 4.3b, where the reduction in the peak force is a result of higher levels of aeration. Greater aeration leads to a broader initial pressure peak, demonstrating that air reduces the pressure amplitude but increases the impact duration.

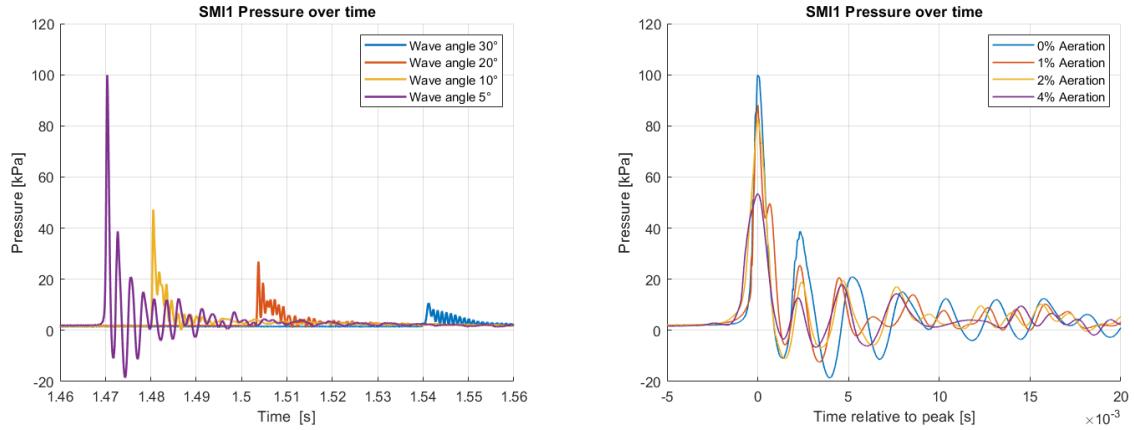

Figure 4.3: Pressure signals:(a) pressure development over time for different wave approach angles for a plate angle of $0°$ and 0% aeration, and (b) effect of aeration on the pressure development over time for a plate angle of $0°$.

For steep plate angles (30°), flatter wave approach angles (5° and 10°) produce a shift of the maximum pressure toward approximately 75 mm, corresponding to the location of SMI 5. This shift is due to the free water surface impacting that location sooner because of the plate/wave configuration. As the plate angle decreases, the shift of the maximum pressure for lower wave approach angles becomes less pronounced. Most peak pressures occur in water with 0 $\%$ aeration, although this is not universal. This indicates that even at low levels of aeration and a Mach number of 0.016, the compressibility of water plays a significant role during breaking wave impacts.

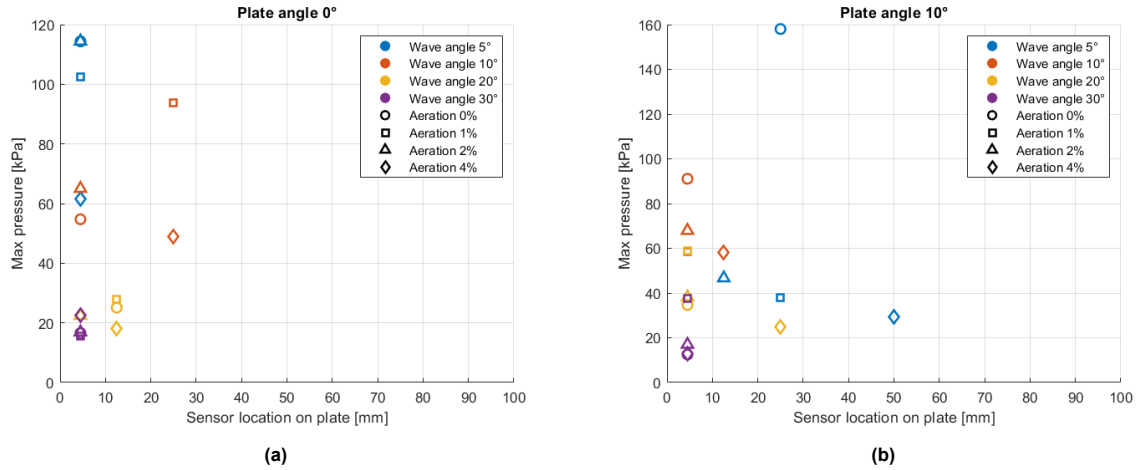

Figure 4.4: Max pressures vs. location for different wave approach angles, levels of aeration and plate angles: (a) $0°$ and (b) $10°$.

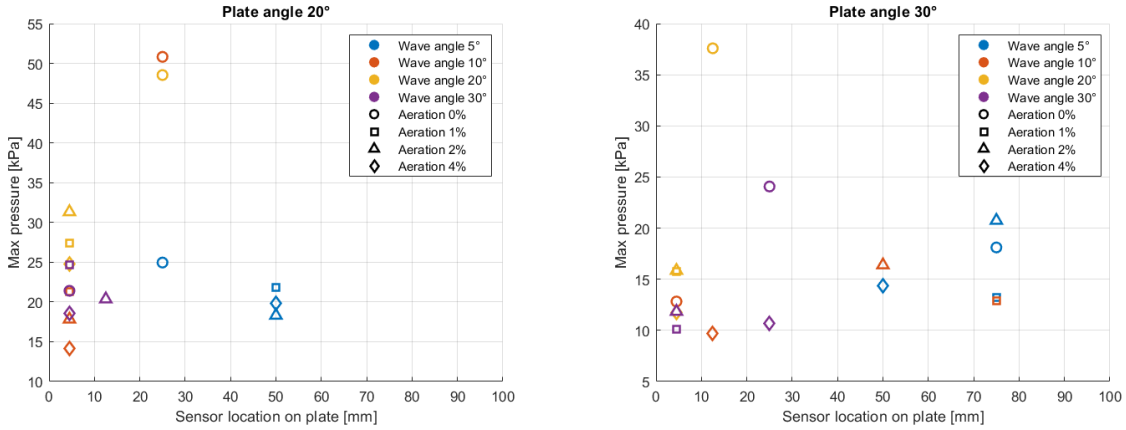

Figure 4.5: Max pressures vs. location for different wave approach angles, levels of aeration and plate angles: (a) $20°$ and (b) $30°$.

A general trend is observed in which higher wave approach angles, corresponding to lower approach velocities, result in lower pressures. This trend is most noticeable at a wave angle of 30°. However, as the relative difference between plate angles and wave approach angles decreases, this relationship becomes less evident. For that reason the effect of the relative angle between the plate and the approaching wave is shown below. A positive angle β_w for plate angle smaller than the wave angle, $\beta_w = 0$ when to the wave approach angle and plate angle are equal and a negative β_w for plate angle larger than wave angle, meaning that entrapped air occurs in the corner.

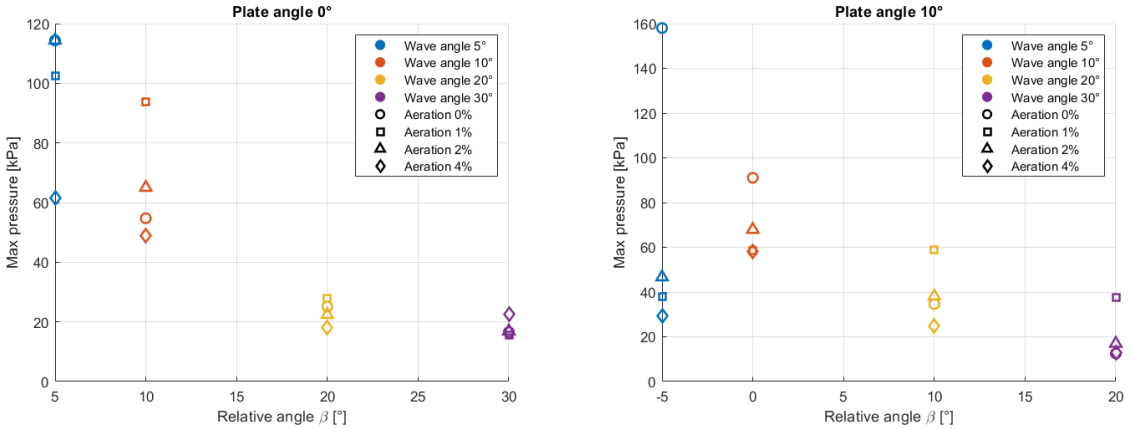

Figure 4.6: Max pressures vs. relative angle β_w for different wave approach angles, levels of aeration and plate angles: (a) $0°$ and (b) $10°$.

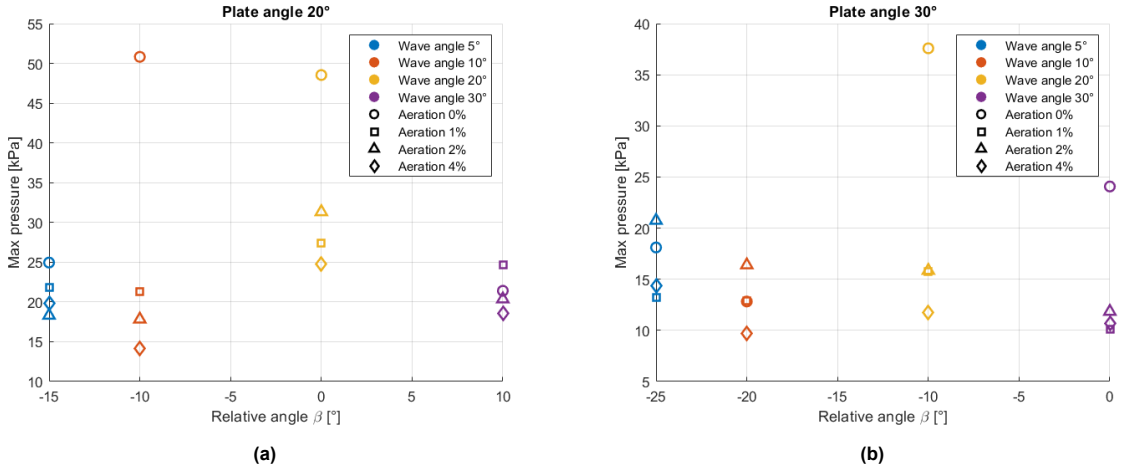

Figure 4.7: Max pressures vs. relative angle β_w for different wave approach angles, levels of aeration and plate angles: (a) $20°$ and (b) $30°$.

For a plate angle of $0°$ the average maximum pressure increases as the wave approach angle decreases. This trend is consistent with the expectation that higher impact velocities generate higher pressures upon impact. As the plate angle increases, however, the differences in maximum pressure between the wave approach angles become less pronounced. This reduction indicates that entrapped air pockets at the plate corner provide cushioning, and thereby dampen the impacts and lower the measured maximum pressures.

The effect is particularly evident for more negative relative angles, where the absolute values of the maximum pressures systematically decrease for the same wave approach velocities. In contrast, a distinct peak in pressure occurs when $\beta_w = 0$ i.e., when the wave approach angle closely matches the plate angle. Under these conditions, the wave front impacts the plate with close alignment, leading to direct and concentrated transfer of momentum. This configuration amplifies the impact, producing high pressures compared to neighbouring values, as is clearly visible in Figure 4.6b and Figure 4.7a. Such an alignment may be interpreted as a “perfect storm” condition, where the plate geometry and incoming wave angle combine to maximise the impact load. Only for the plate angle and wave approach angle of $30°$ in Figure 4.7b this effect is not clear, which may be due to the low impact by this specific wave type.

Pressure time series

The measured pressure time history is strongly influenced by local conditions, such as airflow and the entrapment of air bubbles. An example of the pressure trace recorded at sensor SMI1 is shown in Appendix B in Figure B.8a. The figure shows that the pressure rise starts before initial impact is hard to determine as local impact conditions make defining the rise time complex according to Abrahamsen [43]. For that reason, simplified triangular pressure histories [41] can provide a more practical approach in the future for estimating the load duration and for simplifying response calculations.

4.1.3. Force: effect of relative angle, plate rigidity and aeration

The measured impact force exhibits a consistent trend: as the wave approach angle decreases (corresponding to higher effective impact velocity), the resultant force increases (Figure 4.8a). Among cases with identical approach angles but varying levels of aeration and plate inclination, the largest impact forces consistently occur for the non-aerated conditions. This indicates that entrained air acts to cushion the impact, reducing the transmitted load. Nonetheless, this is not always the case when the wave approach angle does not correspond to the plate angle and more variability in the results seem to occur.

Furthermore, for a given wave approach angle, the maximum forces are recorded when the plate angle matches the wave approach angle (e.g. $\beta_w = 0$, see Figure 4.8b). In this setup, the local impact occurs perpendicular to the plate surface, leading to the most efficient momentum transfer and consequently the highest measured force.

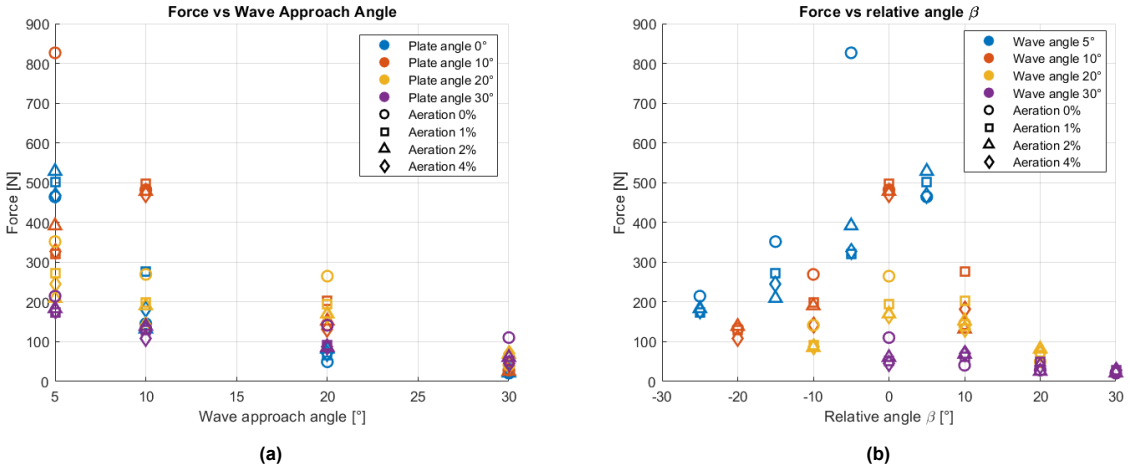

Figure 4.8: Maximum compression force for combinations plate angles and levels of aeration: (a) compared to different wave approach angles, and (b) compared to the relative angle β_w.

Figure 4.9b presents the maximum force corresponding to comparable relative angles. Note that different combinations of wave approach angle and plate angle can result in the same relative angle. A pattern similar to that seen in Figure 4.9a is observed, with the influence of hydroelasticity becoming increasingly pronounced as plate thickness decreases. However, Figure 4.9b further reveals that the effect of hydroelasticity diminishes for large relative angles (approximately ±20–30°). The highest forces are observed at a relative angle of 0°, followed by relative angles of +5° and +10°, and then by -5° and -10°. This pattern highlights two additional mechanisms. First, the closer the wave approach angle aligns with the plate angle (in both positive and negative directions) the higher the resulting force. Secondly, a relative force reduction for $\beta_w < 0$ compared to $\beta_w > 0$ due to larger air entrapment having a damping effect. Additionally, Figure 4.9b shows an increased variability in the maximum forces for lower plate thicknesses for a larger negative relative angle β_w. It is hypothesised that the observed variability is caused by increased air entrapment at greater negative relative angles (β_w), where increased air cushioning leads to a prolonged impact duration and, for decreasing plate thicknesses, a greater energy transfer takes place between the fluid and the structure due to the stronger hydroelastic coupling specific to these fluid–structure combinations. However, the specific mechanisms governing this variability remain uncertain.

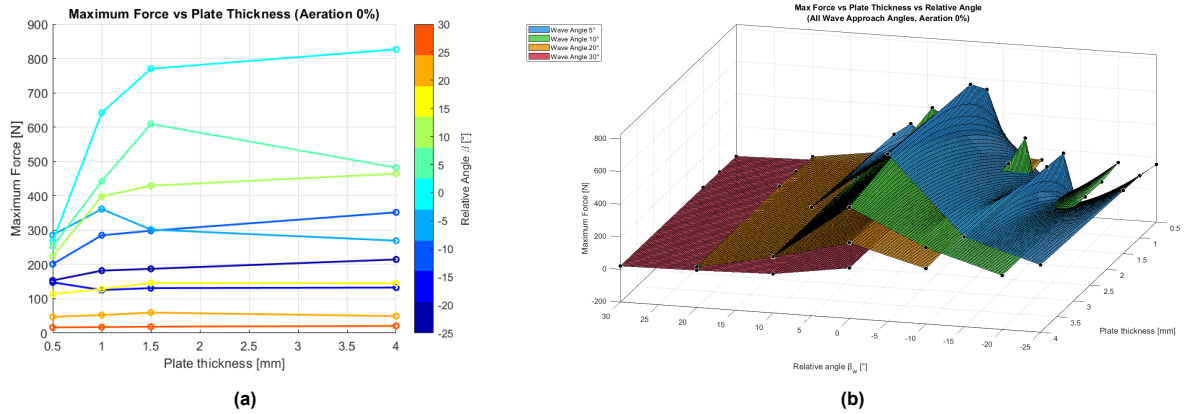

Figure 4.9: Maximum compressive force vs. plate thickness for 0% aeration: (a) comparison for different relative angles β_w, and (b) 3D representation for all wave approach angles and relative angles with 0% aeration.

Peak force rise time

The force rise time is defined as the time between the mean force and the first measured peak compression force as is shown in Figure 4.10a. The rise time characterises the duration of the initial impact and is dependant on the type of impact.

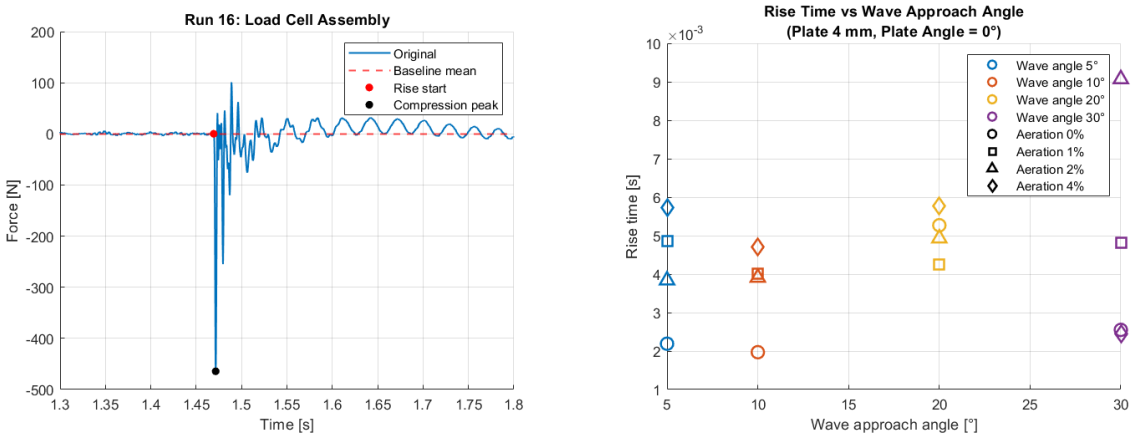

(a) (b)

Figure 4.10: Rise time: (a) the force signal for a plate angle of $0°$, wave approach angle of $5°$ and 0% aeration, and (b) Trend of rise time for different wave approach angles.

The rise time is plotted for different wave approach angles and aeration levels for a 4mm plate to characterise the influence of the wave shapes on the rise time. A general trend can be identified in Figure 4.10b that heavier impacts (lower wave approach angles) results in rapid increase of force in a short period. Additionally, for the approach angles of 5,10 and 30° higher levels of aeration results in a longer rise times.

The rise time is plotted in Figure 4.11 for different wave approach angles and plate thicknesses to characterise the influence of hydroelasticity. Rise times show an increase trend with decreasing plate thickness. This suggests that deformation of the plate prolongs the contact time between the wave and the plate. For the plats at $0°$, the lower wave approach angles lead to shorter durations of the peak force, which is primarily related to the energy contained in the wave. Whether this is also related to the relative angle needs further investigation.

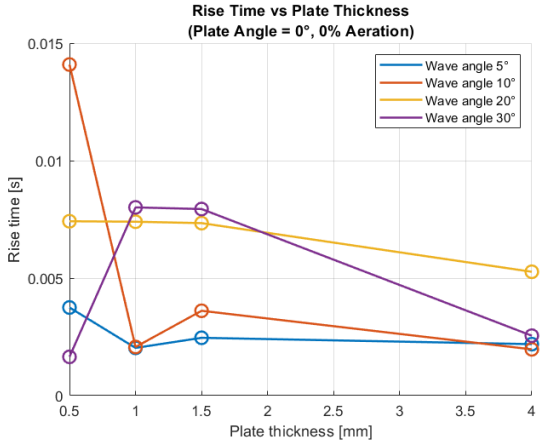

Figure 4.11: The rise time for different plate thicknesses at a plate angle of $0°$ and 0% aeration.

When considering the individual contributions, aerated wave impacts tend to increase the rise time because the presence of air bubbles dampens the load, spreading the impact over a longer period.

Similarly, elastic plates also increase rise time, as the deformation prolongs the contact duration with the wave. However, when these two effects are combined with aerated impacts acting on elastic plates, the expected cumulative increase in rise time is not observed. The reason is that aerated waves produce lower peak loads, which in turn cause smaller deformations in the elastic plates. As a result, the prolongation of rise time due to plate elasticity is partially counteracted by the reduced deformation. This interaction highlights how the damping effect of aeration and the deformation of elastic plates do not simply add up, but rather interact in a way that influences the overall response.

4.1.4. Plate deformation: effect of relative angle, plate rigidity and aeration

The deformation of the plates is measured using the three laser distance sensors as described in subsection 3.2.4. The horizontal positioning of laser 171 is influenced by the plate's angle and thickness, since plate deformation under impact can reduce the effective horizontal distance of the plate due bending deformation. For a plate angle of 0°, the laser is positioned at 195 mm. At a plate angle of 10° with plate thicknesses of 1 mm and 0.5 mm, the laser position is 180 mm. When the plate angle increases to 20°, the laser is placed at 170 mm, and for the same angle with a reduced thickness of 0.5 mm, the position decreases to 140 mm. Finally, for a plate angle of 30° and a thickness of 0.5 mm, the laser is positioned at 125 mm. For this reason, the measured maximum deflections presented below are based solely on the vertical deformation of the plate at plate and angle specific horizontal locations, which should be considered when interpreting the results.

Plate deformation

Figure 4.12 shows the displacement at 3 locations on the plate for two wave approach angles for a 0.5mm plate. Depending on the wave approach angle, the largest deformation may occur on initial impact (Figure 4.12b) or when the plate moves downwards again on the secondary loading due to waves mass further exciting the plate or a possible vacuum effect in the corner of the plate. This effect is shown in Appendix C. Depending on the plate thickness, plate angle and wave approach angle the motion of the water mass following the plate can reinforce or oppose the oscillations depending on timing and phase.

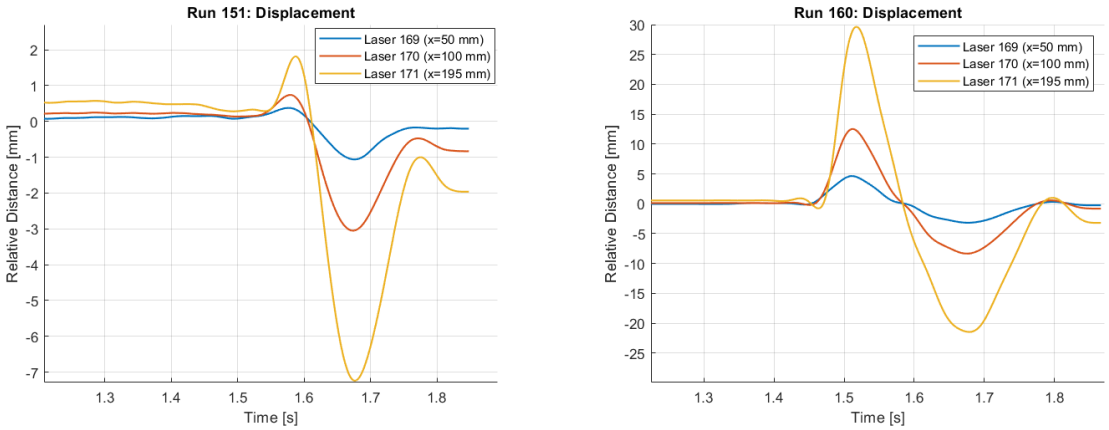

Figure 4.12: Displacement of a horizontal 0.5mm plate at different locations for 0% aeration for (a) wave approach angle of $30°$ and (b) wave approach angle of $5°$.

The temporal evolution of the plate deformation was interpolated from the four measured plate positions and is presented in Figure 4.13. The deformation is illustrated using a colour gradient, highlighting the moment of maximum excitation and the asymmetry of the deformation resulting from differences in damping and loading.

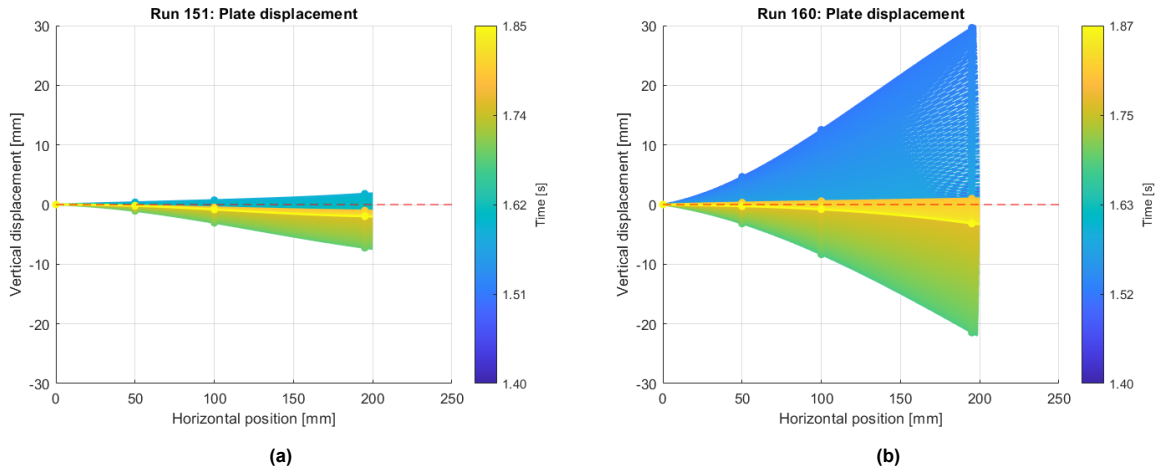

(a) (b)

Figure 4.13: Interpolation of plate displacement of a horizontal 0.5mm plate at 0% aeration for (a) wave approach angle of $30°$ and (b) wave approach angle of $5°$.

The analysis of the behaviour of the maximum and minimum deflection as described earlier at Figure 4.12 is extended in Figure 4.14. Both the minimum and maximum deflection increases for decreasing wave approach angles and decreasing plate thicknesses. Where the maximum peak deflection is dominated by smaller wave angles (5° and 10 °), the minimum peak deflection is dominated by larger wave angles (5° and 10 °) at lower plate thicknesses. Furthermore, both maximum and minimum peak deformations are increasing exponentially with decreasing plate thickness. This behaviour aligns with 1D-bending theory where the bending stiffness decreases by a factor of 8 when decreasing the plate thickness by a factor of 2, as follows from $EI = E \cdot \frac{bt^3}{12}$.

Variable loading, non-linearities and added mass effects may explain the difference between the anticipated deformation and the measured deformation.

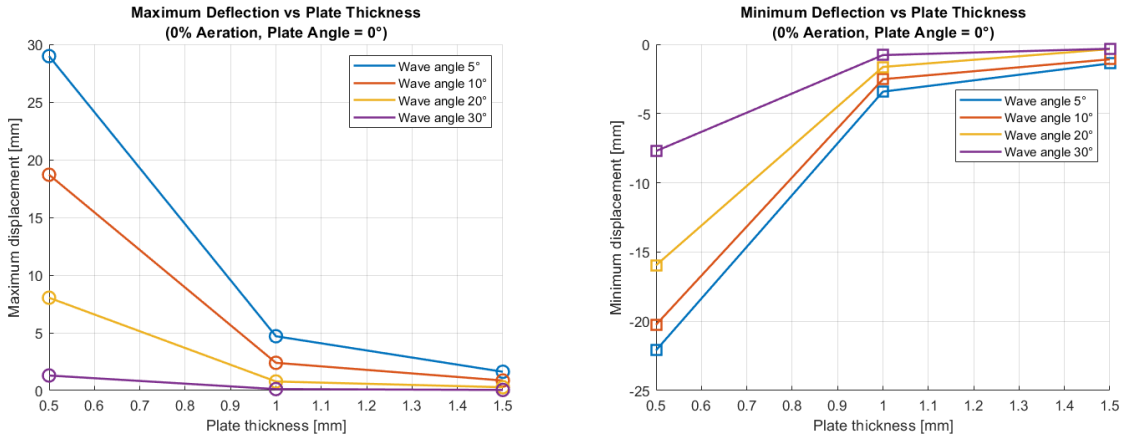

(a) (b)

Figure 4.14: Maximum plate tip displacement for different plate thicknesses: (a) maximum upward deflection, and (b) minimum downward deflection.

In Figure 4.15 the effect of the relative angle may be derived. Note that for a plate angle of $30°$, two data points are missing because the plate deformation exceeded the measurable range of the laser. Contrary to the pressure and force measurement where the relative angle was governing for the relative increase in loads which correspond to described for the force in subsection 4.1.3 and pressure in subsection 4.1.2, the deformation is not governed by the relative angle, but rather shows a consist

trend that the wave angle is now governing for the deflection of the plate. Additionally, for increasing plate angles the maximum deflection shows an increasing trend, potentially caused by the fact that a larger water mass impacts the plate further from the wall as was shown for the location of the maximum pressures in Figure 4.6 and Figure 4.7, resulting in a larger moment.

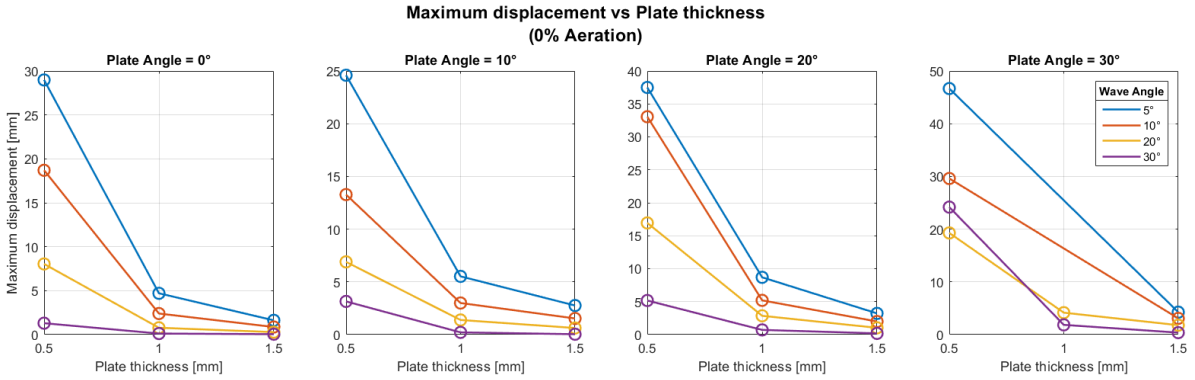

Figure 4.15: The effect of the plate angle vs. the wave approach angle on plate displacement.

The influence of aeration on the displacement of elastic plates was investigated for different plate thicknesses. Figure 4.16 illustrates that the effect of aeration varies with plate thickness. For the thinnest plate considered (0.5 mm), which exhibits high elasticity, increasing aeration appears to increase the maximum displacement. In contrast, for the thicker plate (1.5 mm), which is comparatively stiffer, the trend is reversed: increasing aeration tends to reduce the maximum displacement.

This behaviour can be explained by the interaction of two phenomena. First, the presence of air can increase the loading duration, which is the dominant factor for highly elastic plates such as the 0.5 mm case, leading to larger displacements due to prolonged excitation. Second, for stiffer plates the presence of air primarily reduces the peak impact force, and since maximum force governs deformation in these cases, the resulting displacement decreases.The transition between these two responses for aerated wave impacts occurs at an intermediate plate thickness, where neither mechanism fully dominates. The same behaviour was found in the analysis of rise time of the force in subsection 4.1.3.

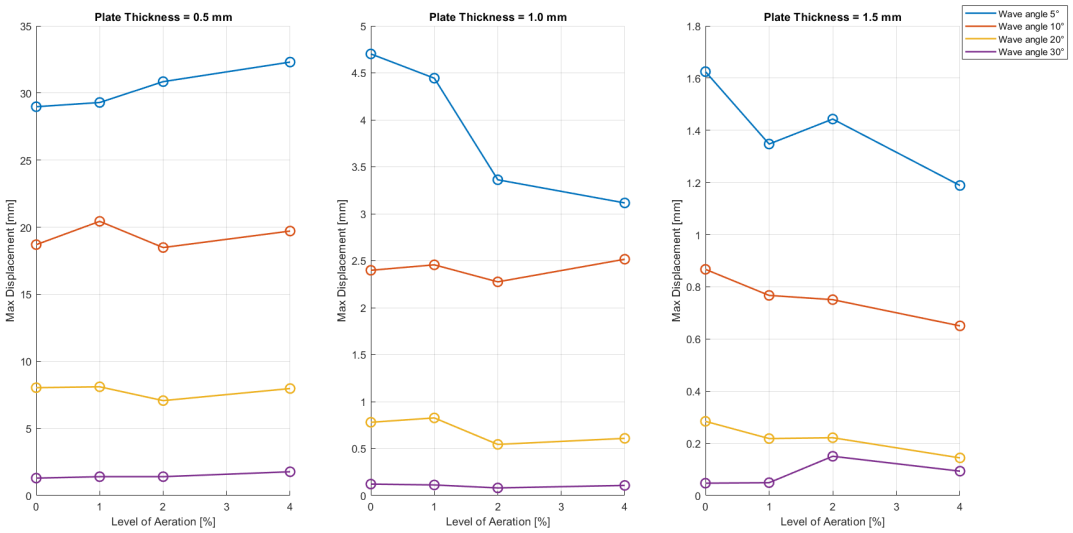

Figure 4.16: The effect of aeration for different plate thicknesses on plate displacement.

Deformational modes

The plate displacement response may be explained by means of the modal analysis, which is used when the transient response of a structure to a non-stationary load or a load of relatively short duration needs to be computed. Pictures from the high-speed camera (Figure 4.17) show different mode shapes that are excited over time during a single wave impact. The analytical response of the plate and modal coordinates based as a results of the hydrodynamic loading is explained in section 2.3.

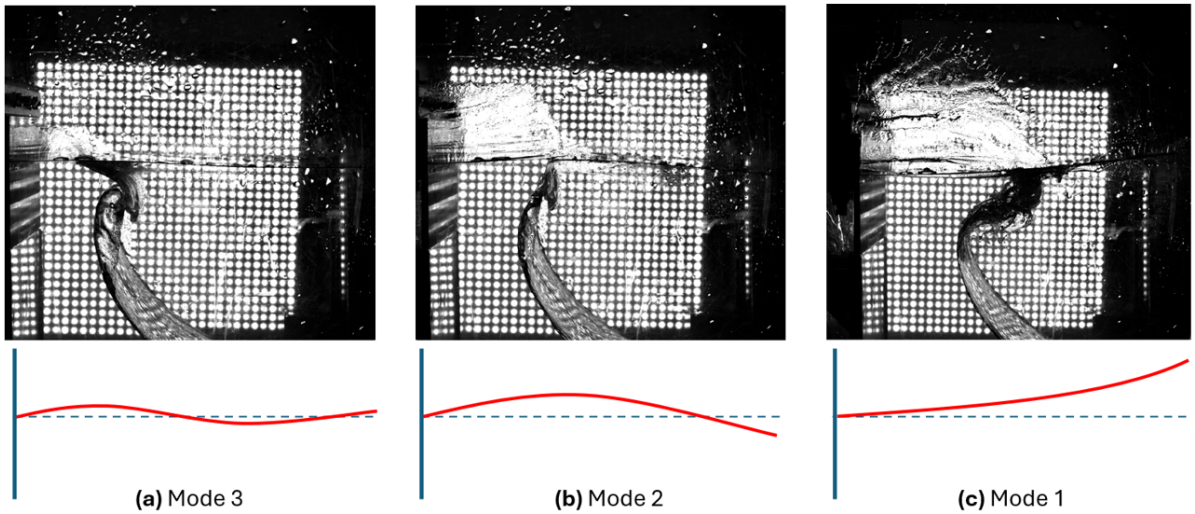

Figure 4.17: The excitation of different eigenmodes in a chronological order in time during one impact of a wave with an approach angle of 5° on a 0.5mm plate.

It was observed that different wave approach angles, front velocities, and initial wetted lengths excite the plates in distinct vibrational modes. For smaller approach angles, larger wave fronts, and higher front velocities, the response of the flexible plates displayed multiple mode excitations within a single impact event, see Figure 4.17. The high-speed camera recordings revealed that, immediately following impact, higher-order deformation modes (e.g. mode 4) were activated. As time progressed, the plate response transitioned through lower-order modes.

The modal evolution may be attributed to several coupled mechanisms. First, the progressive increase in wetted area imposes additional hydrodynamic constraints leading to lower-frequency plate deformations. Secondly, the precise location and distribution of the impact load at a given moment in time influence which modes are excited. In combination, these factors may explain the observed temporal shift from complex, higher-order responses immediately after impact toward simpler, large-scale deformations as the interaction evolves. For impacts with lower velocity and smaller wetted areas, the pressure loading evolves gradually, resulting in a forcing function with a spectrum concentrated at low frequencies. Higher-order modes which possess larger natural frequencies receive negligible excitation energy because the spectral overlap with the forcing is small. Consequently, the response is dominated by the fundamental mode, which has the lowest natural frequency and the largest modal participation factor for low-frequency loading.

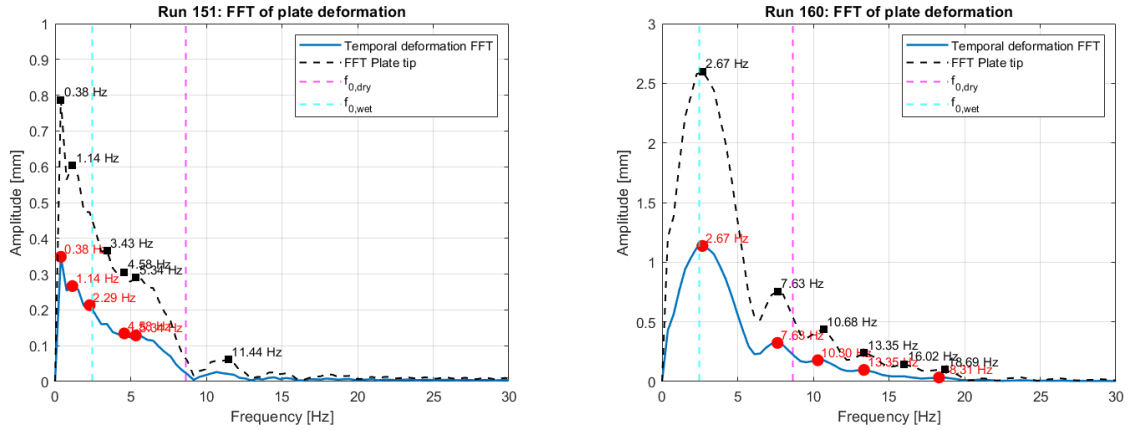

Figure 4.18: FFT on the average plate displacement of a horizontal 0.5mm plate at 0% aeration for (a) wave approach angle of $30°$ and (b) wave approach angle of $5°$.

In contrast, impacts generated by smaller approach angles, larger wave fronts, and higher velocities produce a forcing function with a broader frequency and energy content, as is shown in Figure 4.18 where the Fast-Fourier Transform (FFT) is used to identify the frequency spectrum of the plate deformation. The spectrum is shown for both the plate tip and the averaged plate deformation based on the interpolation curve approximating the behaviour across the entire plate length as described in Figure 4.13. The wave with a $5°$ approach angle excites multiple modes simultaneously. As the interaction evolves, the progressive increase in wetted area and associated added hydrodynamic mass shifts the effective system frequencies downward, suppressing higher-order oscillations and leaving the fundamental mode as the dominant response. This change in the wetted length and therefore added mass causes the (wetted) natural frequency of the plate to shift over time, which is shown in Figure 4.19. The FFT of the wave with an approach angle of 30° displays simultaneous peak frequencies, but its energy content is insufficient to activate modal responses governed by the plate's properties. Therefore, based on the available data, the origin of the lower-frequency peaks remains uncertain. For the wave with an approach angle of $5°$s the highest frequency peaks occur first, after which the lower frequency peaks occur later in time. This relates back to the modal evolution as described in Figure 4.17, although the exact time trace may be different the FFT is based on the averaged temporal displacement of the entire spline interpolation.

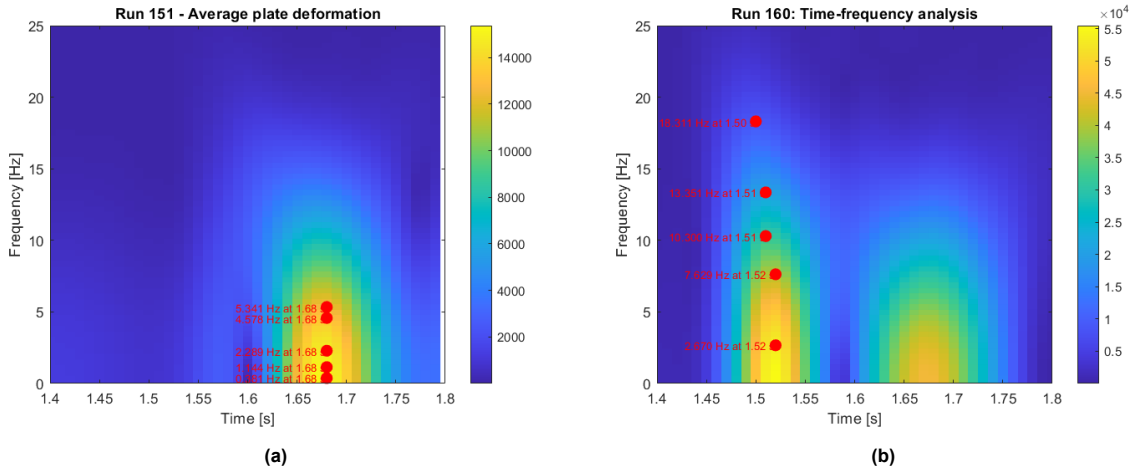

Figure 4.19: Time-frequency plot on the average plate displacement of a horizontal 0.5mm plate at 0% aeration for (a) wave approach angle of $30°$ and (b) wave approach angle of $5°$.

4.1.5. Impact duration: force vs. displacement

In previous studies the wetting time, which is the time required for the wetted length to develop as the plate enters the water, served as a practical measure of the impact duration and can be related to the relevance of hydroelasticity [39], [40]. However, the current study on wave wedges impacting a plate differs from a wedge entry. The wetted area upon wave impact is variable, and the added mass associated with the fluid–structure interaction evolves dynamically in time and space. Consequently, the classical notion of wetting time for the wedge impact does not adequately capture the characteristic loading duration. Instead, the effective wetting time is represented by the duration of the compressive phase of the impact, i.e., the time over which the initial upward force acts on the plate. This duration takes the evolving added mass and its momentum into account, providing a more physically relevant timescale for the dynamic interaction between the wave and the structure. Although impact duration is now compared with time in compression leading to the initial upward deflection, the followed downward deflection and associated tensile impulse are also significant as was shown in Figure 4.14. However, secondary effects such as fluid adhesion to the plate, turbulent flow and additional air entrapment further complicate the analysis of the loading after compression.

The measured force Figure 4.20a during a single wave impact typically exhibits two distinct peaks. The first corresponds to the compression force generated by the initial wave impact, causing the plate to deform upwards. This peak is characterised by a high magnitude and a short duration. The second peak arises during the tension phase, when the plate moves downwards. This tensile peak generally has a lower magnitude but a longer duration compared to the initial compression peak. The area under these peaks can be defined as the force impulse, providing a measure of the total momentum transfer during each phase. Figure 4.20a shows that the maximum/minimum deflections do not correspond to the maximum and minimum force peak in time, as there is a large delay in the deflection. Additionally, in Figure 4.20b a small dip is noticeable before the marked rise of the maximum deflection. Upon initial impact, first a higher mode of deformation is excited, as is described in Figure 4.1.4. The time of this initial deformation aligns to the time of the peak impact force.

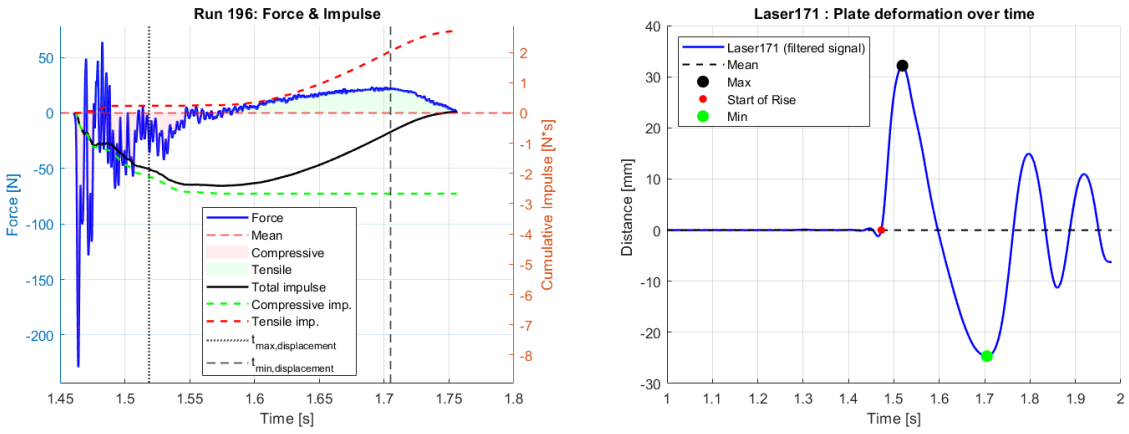

Figure 4.20: Force vs. deformation for a 0.5mm plate, 4% aeration, plate angle of 0° and wave approach angle of 5°: (a) force response, impulse and time of max/min deflection, and (b) the corresponding deformational response.

While aeration in the water can prolong the initial compressive impact due to the compressibility of the air bubbles, it may reduce the tensile impulse because the bubbles disrupt the liquid bridge formed between the water and the plate, leading to earlier detachment of the water from the plate surface. Aeration further weakens the adhesion by introducing air pockets that disrupt continuous liquid contact. Additionally, an increased plate angle relative to the horizontal could facilitate drainage along the plate due to gravity, and consequently decreasing adhesion. And at last, plate rigidity can also play a significant role as elastic plates may conform to the water surface, temporarily increasing adhesion and extending load duration, whereas rigid plates maintain a fixed geometry, resulting in shorter tensile interactions.

Figure 4.21 illustrates that the duration of the compressive impulse depends on both the wave approach angle and the relative angle β_w. The duration is longest for the smallest approach angles (corresponding to the highest wave velocities) and increases with smaller relative angles. Moreover, for the 1.5 mm plate, there is no significant difference in impulse duration between the non-aerated and aerated impacts. In contrast, for the more elastic 0.5 mm plate, the aerated impacts generally have a longer impact duration. This indicates that the influence of aeration is dependent on the plate's rigidity, which is in line with the observations in Figure 4.16. Furthermore, the results suggest that the increased deformation observed in more elastic plates is associated with the prolonged impact duration, implying that reduced structural stiffness allows the plate to respond over a longer timescale under compressive loading.

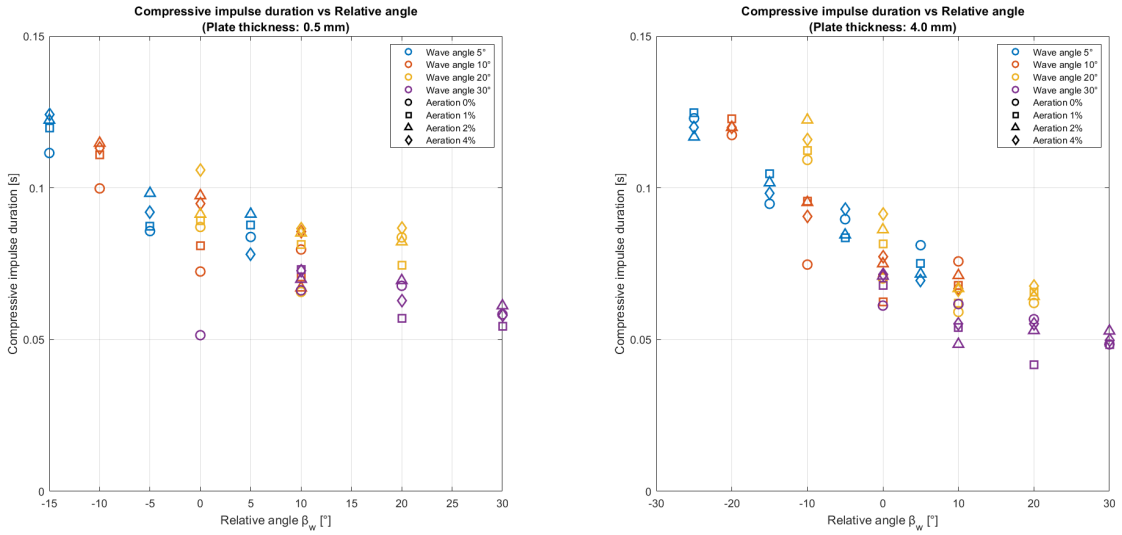

Figure 4.21: Compressive impulse duration vs. relative angle for different percentages of aeration: (a) plate thickness of 0.5mm, and (b) plate thickness of 4.0mm.

4.1.6. Cavitation

To capture and analyse the behaviour during impact under the so-called "perfect storm" condition, a high-speed camera was applied to visually record the hypothesised formation and collapse of bubbles beneath the impact plate due to cavitation, as described in Figure 3.2.4. The presence of cavitation could lead to high pressures and local pressure variability. However, based on the Rayleigh–Plesset equation, which describes the collapse time of cavitation bubbles (subsection 2.1.4), and the high-speed camera footage, no evidence of cavitation bubble formation was observed. Consequently, the increased measured forces and pressures under the "perfect storm" condition are more likely attributed to an optimal momentum transfer rather than cavitation effects.

4.2. Numerical results

In this section, the numerical results obtained using ComFLOW are presented and compared with a selection of experimental runs. The comparison focuses on impact pressures, forces, and their frequency responses, to evaluate both the influence of the experimental setup on the measurements and the extent to which the numerical predictions capture the observed behaviour.

4.2.1. Force comparison

The maximum impact forces are presented for a plate under a 10° angle in Figure 4.22b. For lower sloshing frequencies, which correspond to lower impact velocities, the numerical results show an increase in force with increasing frequency. However, the difference between the experimental and numerical results becomes more pronounced at higher sloshing frequencies. The frequencies of 0.85, 1.00, 1.15, and 1.40 Hz correspond to wave angles of 30°, 20°, 10°, and 5°, respectively. Beyond 1.15 Hz the computed maximum force decreases, suggesting that higher impact velocities generate shorter peaks that are not fully resolved in the simulation at the maximum achievable resolution for this thesis. A frequency filter of 400 Hz was applied to the numerical signal. While this filter effectively captures the overall trend, it limits the simulation's ability to resolve the load peaks accurately. And conversely, removing the filter results in unrealistically high peak forces compared to the experimental measurements.

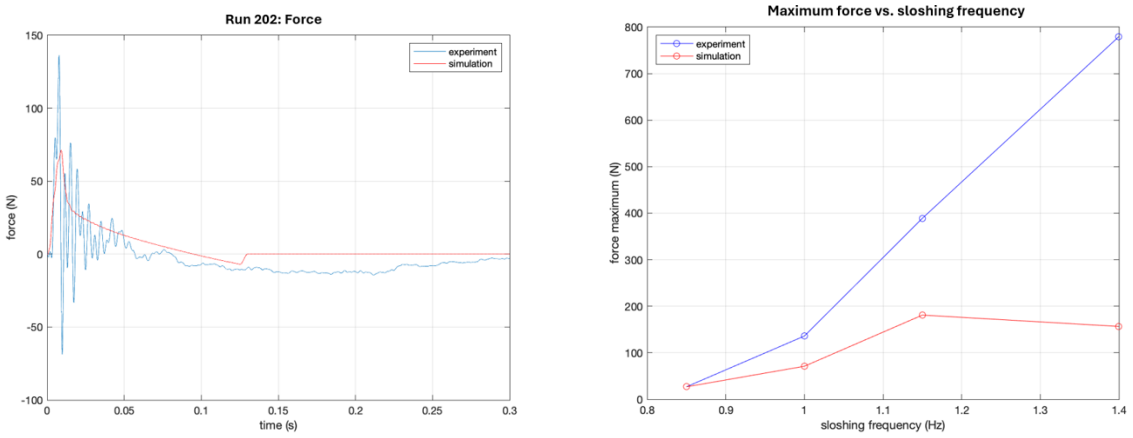

(a) (b)

Figure 4.22: Force determined experimentally vs. ComFLOW: (a) results for a plate angle of 10° and wave approach angle of 20 degrees, and (b) Maximum force for a plate angle of 10° for different sloshing frequencies.

The increasing difference in the measured force may also result from the larger moment generated by the higher impact forces and the changing load application on the plate. As illustrated in Figure 4.5, the variation in plate angle affects how the load is transferred to the load cells. This moment is introducing a significant non-linearity in the measurements, as discussed in section A.1.

Besides the difference in the peak load, Figure 4.23 reveals a strong resonant behaviour. At 30 Hz, this resonance likely arises from the load cells and the impacted assembly, indicating that the impacts contain a frequency close to the system's natural frequency. Consequently, the measured response can be amplified, which may affect the accuracy of the recorded load values.

Nevertheless, the integration methods used to approximate the impact duration, as described in subsection 4.1.5, can still be considered valid. These methods are less sensitive to the high-frequency fluctuations observed in the measurements. While the calculated duration may be shorter than that obtained from a comparable numerical integration when the resonance crosses the tension/compression transition, the method remains effective for capturing the overall force trends and impact duration.

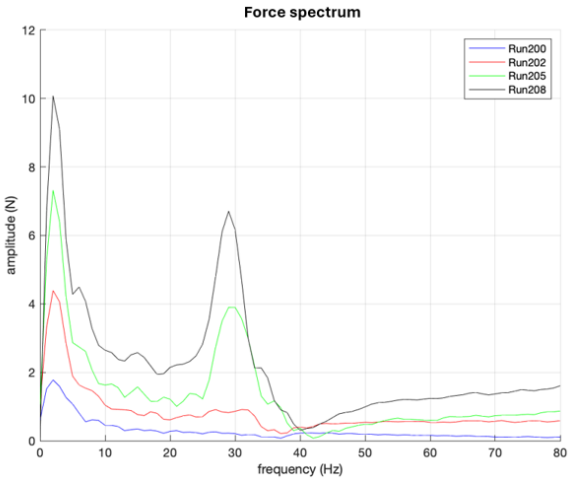

Figure 4.23: The frequency analysis for different wave approach angle for a plate angle of $10°$.

4.2.2. Pressure comparison

For the pressure comparison between the simulation and the experiments in Figure 4.24, the pressure peaks and overall behaviour are captured reasonably well. However, for slower wave impacts, the simulation predicts the pressure rise earlier than observed experimentally. The magnitude of this phenomenon is not associated with the spatial averaging shown in Figure 3.6a, but instead is likely to arise from a difference between the simulated and experimental accelerations of the sloshing tank. Although the tank position is measured during the experiments, taking its second derivative can introduce deviations from the actual tank acceleration. Additionally, the numerical simulation includes a discontinuity in the approximation of the tank's acceleration, which may further contribute to the observed differences. It is therefore recommended to measure the tank's acceleration in future research.

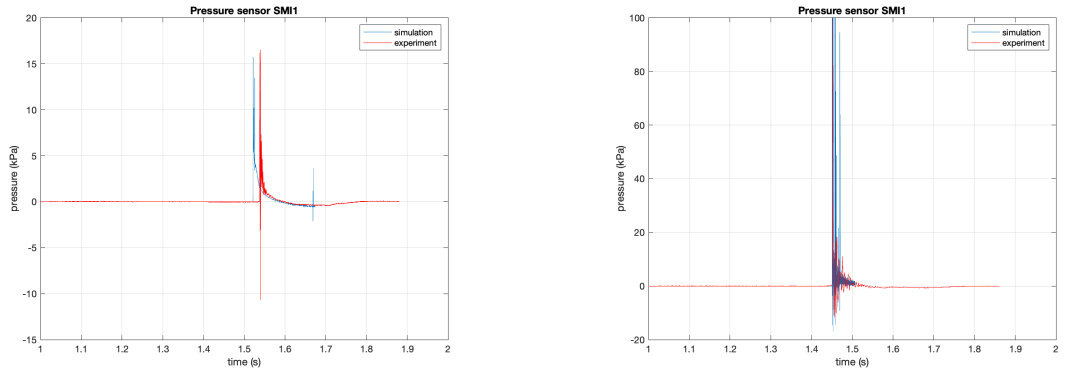

(a) **(b)**

Figure 4.24: Pressure time history determined experimentally vs. ComFLOW for a plate angle of $10°$: (a) results for a wave angle of $30°$, and (b) results for a wave angle of $5°$.

Additionally, a slight resonance can be observed in the measured pressure signal. The SMI pressure sensors feature a small cavity that houses the sensing diaphragm. It is likely that an air bubble became trapped in this cavity, leading to high-frequent oscillations in the measured pressure. Another possible cause is the vibration of the plate itself, which could also induce fluctuations in the recorded pressure. The numerical pressures also show numerical peaks. While the "true" value of the pressure is obtained through further analysis of the numerical and experimental configurations, continued research on the numerical model and the underlying sloshing dynamics is essential to improve predictive reliability.

5

Discussion

This chapter interprets the findings of the hydroelastic impact experiments, focusing on the effects of plate rigidity, inclination, aeration, and wave shape. A comparison is made with relevant literature to contextualise the findings.

5.1. Loads vs. plate rigidity

The findings of this study align with previous research on the influence of flexibility and aeration on impact loads, while providing new insight into the role of wave geometries, wave/plate alignment and the effect of air entrainment. Consistent with Mai [8] and Zhang [30], the results confirm that flexibility and aeration reduce impact pressures and forces. The observed decrease confirms that entrained air cushions the impact, dissipating energy between the fluid and the structure. In contrast to Attili [31], who reported negligible influence of plate stiffness on total force, the present findings show that hydroelastic effects are more pronounced for thinner plates and higher wave approach velocities. Lower wave approach angles with higher impact velocities produce shorter rise times, while more flexible plates exhibit longer rise times due to deformation that prolongs fluid–structure contact. For aerated waves impacting elastic plates, the effects of aeration and plate deformation on rise time interact non-linearly, revealing the combined influence of fluid cushioning and structural flexibility on plate stresses and strains. Additionally, the relative wave–plate angle (β_w) remains a critical factor: maximum pressures and forces occur at $\beta_w = 0$, while misalignment and air entrapment at non-zero β_w substantially reduce impact magnitude. Overall, the magnitude of deformation is not solely governed by the wave load, but also by the impact duration, plate–wave interaction geometry, and degree of aeration.

5.2. Plate deformation

The discussion on whether the solution of a structural response should include hydroelastic effects was described by Faltinsen [39] and Bereznitski [40] who presented a summary of results for a wedge impacting water at a constant velocity, illustrating the maximum displacement as a function of two parameters: the dead rise angle of the wedge and ratio between the first natural frequency of the beam against the impact duration. Bereznitski concluded that if the ratio is more than 2.0 the effect of hydroelasticity can most likely be neglected. After this point, the impact loading acts slowly compared to the structural vibration and a quasi-static approach is sufficient. In Figure 5.1b the reduction of displacement in the middle of the beam relative to the displacement for a non-aerated impact(Figure 5.2b) is shown. When comparing the moving average of the maximum deflection with the inverse of the reduction of deformation in Figure 5.1, similar trends are observed. Based on the ratio between the duration of the compressive impulse and the first dry natural frequency of the plate, hydroelastic effects are of less significance when this ratio exceeds a value ranging from approximately 1 to 2, depending on the plate thickness and percentage aeration.

Bereznitski also observed that the structural stiffness influences the reduction in deformation during wedge impact, showing around a 30% difference between a plate with a first free vibration frequency of 19.0 Hz and one at 43.6 Hz [40]. For the overhanging cantilevered plate impact, the maximum deformation and the degree to which hydroelasticity plays a role appear to be far more affected by the plate thickness. This may be attributed to the differences in boundary conditions between the two

configurations, as well as additional membrane effects when the beam is clamped on both sides in the case of the wedge impact as is described in subsection 3.2.6. Another reason for the difference that the current impact duration is based on the compressive impulse duration, rather than on the wetting time.

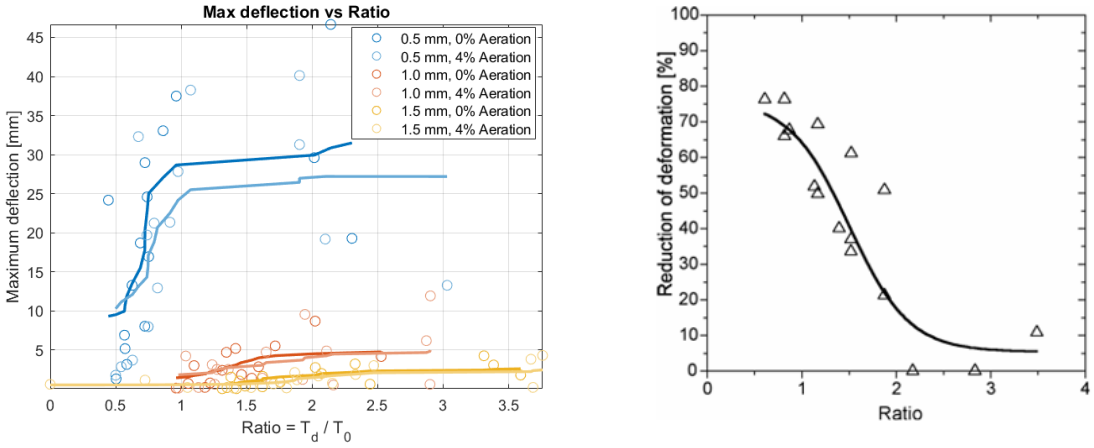

(a) (b)

Figure 5.1: Defection vs. Ratio: (a) the moving average of the maximum deflection of the plate tip vs. the ratio from the current study, and (b) the reduction of deformation in the middle of a beam in a wedge for increasing ratio [40].

A comparison between Bereznitski's research case and the current setup is demonstrated in subsection 3.2.6. The scenario most comparable to a wedge without large air entrapment is selected for comparison where for the wave angle of $30°$ all relative angles remain non-negative. Figure 5.2a shows trends consistent with Bereznitski's findings: the maximum deflection of the structure is the largest for the plate with the lowest dry natural frequency and decreases with increasing levels of aeration. In the current study however, it was found that the impact duration and maximum deformation can increase for aerated impacts for the plate with the lowest natural frequency depending on the relative angle as is discussed in subsection 4.1.5.

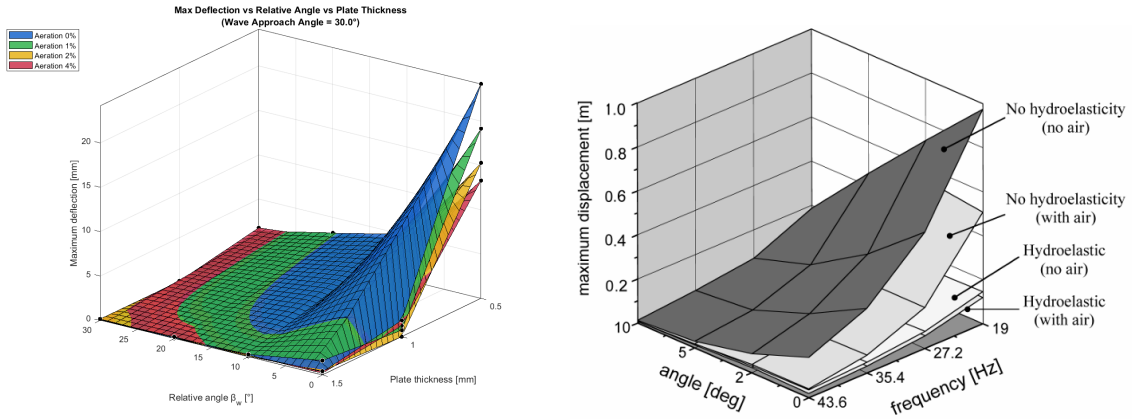

(a) (b)

Figure 5.2: Effect of plate thickness and aeration on displacement: (a) plate displacement for a constant $30°$ wave approach angle, and (b) the maximum displacement of a beam of a wedge impacting the water surface with a constant velocity [40].

Additionally, for larger relative angles the maximum deflection across different aeration levels appears to follow a different trend from that reported by Bereznitski. Although the effect of aeration compared to non-aerated impacts on the deformation is smaller for rigid plates, and with a reduced loading as $\beta >> 0$ (as was shown in Figure 4.8a), aerated impacts may still produce slightly greater deformations.

For a direct comparison with the graph in Figure 2.4, which illustrates the significance of hydroelasticity in wedge impacts as described by Equation 3.10, further investigation is required into the influence of the boundary conditions in the current experimental setup described the correction factor κ applied to the modified dimensionless parameter ξ^*, as defined by Faltinsen Equation 3.10.

5.3. Compressibility mixture

In subsection 4.1.2, it is concluded that the the effect of compressibility occurs even at Mach numbers as low as 0.016. However, for wedge impacts with aeration percentages comparable to those studied in this thesis, the Mach edge number was found to significantly affect the impact pressure only above 0.05 [26], [27]. This indicates that higher velocities are required for wedge impacts than for wave impacts on a cantilevered plate, depending on both the wedge angle and the angle between the plate and the wave.

In aviation, compressibility effects in air generally become significant at Mach numbers above 0.3, leading to a 5$\%$ change in air density [61]. Air is relatively easily compressible, and with having a low density and a low bulk modulus K flow must reach comparatively high speeds to exceed this threshold. In contrast, the results presented subsection 4.1.2 indicate that compressibility becomes important at much lower Mach numbers around 0.016, even for small air fractions (1%) and despite the medium having a higher density and bulk modulus but experiencing lower flow velocities. The reason why compressibility becomes relevant at such low Mach numbers in aerated water, compared to the case of pure air, may be due to relative change in density, but is not yet fully understood and requires further research.

5.4. Cavitation

Galiev [35] suggest that cavitation may play an important role under impulsive loading conditions, however there was no cavitation based on the high speed camera images. According to Galiev, the effect of cavitation becomes significant when the duration of the water pressure loading is shorter than the fundamental period of the plate vibration, or equivalently, when the frequency of loading exceeds the natural frequency of the plate. Although the measured pressure time histories in this study included loading durations of similar order, no cavitation developed, indicating that other factors mitigated the formation of cavitation.

One reason for the absence of cavitation is that local pressures did not drop sufficiently below the cavitation threshold. According to cavitation requires pressures on the order of 0.2–0.35 MPa below ambient conditions [35], depending on hydrodynamic effects and the presence of nuclei. In the experiments, the maximum pressure associated with the approaching wave with the highest velocity of 2.2 m/s (Figure 4.2) and shortest loading times was approximately at 160 kPa, and the calculated cavitation number (Equation 2.8) for this case σ is 65. This high cavitation number indicates that the fluid was far from conditions favourable for cavitation, although the presence of turbulence and air bubbles may lower this threshold. Nonetheless, the water may experience much larger velocities following the impact, which drastically lowers the cavitation number and increases the likelihood of cavitation.

Additionally, the hydroelastic coupling between the plate and water plays a significant role in flexible plates: the water tends to move together with the plate, preventing separation and the low pressures required for cavitation. While plates with low natural frequencies can exhibit high-frequency responses around 500 Hz (see Appendix C), the corresponding vibration amplitudes were small, and the resulting local suction may be insufficient to reach the cavitation threshold. In tests with rigid plates cavitation also did not occur. In this case, the absence of cavitation can be explained by the insufficient local pressure drop and the inertia of water, which resists sudden acceleration and prevents the formation of low-pressure regions.

6

Conclusions

This study examined the hydroelastic impacts of breaking waves on a flexible plate through combined experimental and analytical approaches. The investigation explored the combined influence of aeration, relative impact angle, and structural flexibility on the magnitude and distribution of impact loads and structural responses. The findings answer the research questions and advance the understanding of hydroelastic wave–structure interactions.

6.1. Answers to Research questions

RQ1: The effect of the relative angle between the wave and impact plate

- The measured pressures strongly depend on the relative angle β_w between the plate and the approaching wave (Figure 4.6, Figure 4.7). When the plate and wave are aligned $\beta_w = 0$, the impact is normal to the surface, producing the highest peak pressures due to direct and concentrated momentum transfer, also known as the “perfect storm” condition. For negative relative angles, entrapped air pockets form near the lower edge, cushioning the impact and reducing the pressure amplitude while increasing the impact duration. Positive relative angles result in delayed impacts and lower pressures because of reduced approach velocity. As the plate angle increases, the influence of wave approach angle becomes less pronounced, with pressure peaks shifting along the plate surface depending on the local impact point.
- The impact force follows a similar trend to the pressure response, being primarily governed by the relative alignment between the plate and wave (Figure 4.8b). The highest forces occur when $\beta_w = 0$, where the wave strikes almost perpendicularly to the plate, resulting in the most efficient momentum transfer. As the wave approach angle decreases (flatter waves, higher velocity), the overall impact force increases; conversely, waves with larger approach angles produce lower forces due to the reduced approach velocity. When the relative angle becomes negative, air entrapment at the plate corner dampens the impact, leading to systematically lower forces than for comparable positive β_w values.
- The maximum plate deformation is influenced by the wave approach angle, plate thickness, and plate inclination. However, the ”perfect storm” scenario does not produce the largest deflections, and increases as the relative angle β_w decreases (Figure 4.15). For the plate with a thickness of 0.5 mm, the greatest deformation can occur either during the initial impact or during secondary loading, when the downward motion of the plate coincides with the returning water mass (Figure 4.12). It is hypothesised that this phenomenon is due to a low-pressure zone that pulls the plate downward. Moreover, increasing plate angle results in larger maximum deflections, likely due to a greater water mass impacting further from the wall and generating a higher moment.

RQ2: The relationship between impact duration, plate natural frequency, and structural response

- Shorter rise times correspond to more impulsive wave impacts. The data showed that lower wave approach angles with a higher impact velocity produce shorter rise times (Figure 4.10b). Plates with a lower frequency exhibit longer rise times, as their deformation under load prolongs the contact between the wave and plate (Figure 4.11). The coupling between fluid and structural motion reduces the eigenfrequency of the plate, resulting in a more gradual build-up of the deflection.
- The modal analysis shows that the plate exhibits multiple vibrational modes during a single wave impact. Waves with smaller approach angles, larger wave fronts, and higher velocities produce broad frequency content (Figure 4.18) and higher-order modes appear immediately after impact, transitioning over time to lower-order modes (Figure 4.19). This evolution occurs as the wetted area increases, imposing additional hydrodynamic constraints and redistributing the forcing over the plate. Impacts with lower velocity and smaller wetted areas primarily excite the fundamental mode, because the forcing is concentrated at low frequencies and higher-order modes receive little excitation. As the interaction evolves, added hydrodynamic mass and damping shift effective system frequencies downward, suppressing higher-order oscillations and leaving the fundamental mode dominant. However, at a wave approach angle of 30°, excitation of the fundamental mode did not occur due to the insufficient energy content. The FFT analysis (Figure 4.19) shows that for a 5° wave approach angle, higher frequency peaks occur first, followed by lower frequency peaks later in time, whereas for a 30° wave approach angle, peak frequencies occur simultaneously, illustrating the time-dependent modal evolution of the plate during impact.
- The significance of hydroelastic effects is related to the ratio between the impact duration and the first natural frequency of the structure as presented by Faltinsen [39]. Bereznitski [40] concluded that if this ratio exceeds approximately 2.0, the impact duration is long relative to the structures eigenperiod, and hydroelastic effects can generally be neglected. For the present cantilevered plate experiments, similar trends are observed. Hydroelastic effects become increasingly insignificant once the compressive impulse duration surpasses roughly 1–2 times the first dry natural period, with the threshold influenced by plate thickness and aeration level (Figure 5.1). In the present setup, the plate thickness exerts a greater influence on maximum deformation and hydroelastic effects than reported in wedge impact investigations. This difference is attributed to variations in boundary conditions (cantilever versus fully clamped wedge bottom plate) and additional membrane effects (subsection 3.2.6) in the clamped case. Furthermore, the impact duration in this study is defined based on the compressive impulse rather than the wetting time, which may also influence the observed hydroelastic response.

RQ3: Influence of aerated water on hydroelastic impacts

- For pressure measurements, higher levels of aeration lower the pressure amplitude but increase the duration of loading, demonstrating that air reduces the intensity of the impact while spreading it over a longer time interval (Figure 4.3). Overall, maximum pressures occur for $\beta_w \approx 0$ and minimal aeration, while both higher aeration and greater relative angles ($|\beta_w| > 0$) lead to a notable decrease in impact intensity (Figure 4.6, Figure 4.7).
- Aerated impacts consistently yield smaller forces than non-aerated ones, confirming the cushioning effect of entrained air. Hydroelastic effects amplify these trends for thinner plates, but diminish at large positive (β_w) where the overall impact energy is lower (Figure 4.8b).
- The plate deformation and compressive impulse duration are dependant on the relative influence of aeration versus the plate stiffness. Aeration and plate deformation both extend the impact duration when considered individually. Aeration reduces the peak loads, resulting in smaller deformations that can counteract the increase of the impact duration induced by plate flexibility. This interaction demonstrates the non-linear coupling between aeration and structural elasticity: although each factor independently increases the impact duration, their simultaneous presence can diminish each other's influence. Consequently, the overall structural response is governed by the interplay between wave the wave impact, aeration level, and plate stiffness (Figure 4.21, Figure 4.16).

RQ4: Influence of entrapped air on hydroelastic impacts

- Maximum forces occur when the plate and wave angles are aligned (β_w = 0), due to direct impact and efficient momentum transfer. However, when $\beta_w < 0$, in addition to the plate-wave misalignment, the entrapped air reduces the transmitted force. For positive relative angles ($\beta_w > 0$), forces are also reduced but the reduction is less pronounced and is mainly related to the plate-wave misalignment (Figure 4.8b).
- Increased maximum forces are observed for thinner plates at larger negative relative angles β_w (Figure 4.9b). This variability is caused by enhanced air entrapment, where increased air cushioning prolongs the impact duration and, for thinner plates, leads to greater energy transfer between the fluid and structure due to stronger hydroelastic coupling, which corresponds to the deformational behaviour previously mentioned for aerated water impacts.
- The maximum deformation is primarily controlled by the compressive impulse duration. As shown in Figure 4.21, decreasing relative angles lead to longer impact durations. Consequently, significant air entrapment further extends the loading duration, thereby amplifying the plate's response.

6.2. Additional findings

- The wave velocity and approach angle resulting from increasing sloshing frequency do not exhibit a linear trend. As the sloshing frequency increases from 0.85 Hz to 1.4 Hz, the wave approach angle decreases while the wave velocity increases. Beyond this range, both parameters show a declining trend, as illustrated in Figure 4.2b, even with a further increase in energy input. This behaviour highlights that the wave geometry relative to the plate configuration plays a crucial role in analysing the resulting impact loads.

6.3. Conclusion

This study addressed the primary research question:

How do hydroelastic effects influence the structural response during specific breaking wave type interactions?

Hydroelastic effects play a significant role in the structural response of plates during breaking wave impacts. Flexible plates exhibit increased deformations, longer force rise times, and more pronounced oscillations due to the coupling between structural elasticity and fluid loading. Hydroelastic effects are particularly important for thinner plates and higher-energy impacts, where plate deflection and added mass influence the measured forces and pressures. The timing and distribution of pressure and force are sensitive to the relative angle between the plate and the incoming wave. Maximum forces and pressures occur when the wave approach angle closely aligns with the plate angle, while negative relative angles can lead to air entrapment, cushioning, and increased variability in the force response. Aeration and entrapped air modify the hydroelastic response by extending the impact duration, reducing peak forces, and altering displacement patterns. The influence of these effects is non-linear and interacts with plate stiffness, leading to opposed trends for plates with a relatively low natural frequency versus plates with a relatively high natural frequency.

Inspired by Hokusai's *The Great Wave off Kanagawa*, illustrating the destructive potential of steep, aerated waves, this experimental study provides an understanding of the mechanisms in play during aerated hydroelastic impacts of breaking waves on flexible structures, offering insights that can improve the design and safety of offshore infrastructure under extreme wave conditions.

7

Recommendations

- This research identified a mechanism governing the non-linear interaction between aerated waves and plate stiffness. Further research is needed to define the transition of this mechanism, particularly regarding the conditions under which the dominant influence shifts between aeration effects and structural flexibility.
- The sloshing rig moves horizontally with a certain frequency to generate the desired wave shape with a corresponding impact velocity. However, the horizontal velocity of the sloshing rig during impact inherently affects the characteristics of the generated wave and therefore added mass effect, as was also discussed by Bos[9] where the effect added mass changes for a moving structure. Further research is therefore needed to quantify the influence of the sloshing rig's motion on wave impact dynamics within this experimental setup.
- The current aeration setup enables the generation of aerated waves. However, by increasing the aerated volume, the pressure in the aeration stones increases which in turn increases the average bubble size. This makes the scaling for comparison between aerated wave impacts increasingly difficult. A future setup should consider independent control of air bubble size alongside aeration level to improve the experimental consistency.
- The calibration results of the load cells indicate that off-axis loading from the vertical wall introduces significant variations in measured forces. It is therefore recommended to carefully document and monitor potential off-axis effects during testing to ensure data accuracy. Alternatively, the use of load cells with reduced sensitivity to applied moments should be considered to minimise measurement errors caused by moment effects.
- To extend research on the formation of cavitation bubbles during breaking wave impacts, the acoustic signal of cavitation bubbles may be investigated with the use of hydrophones with special focus on spectral and wavelet-analyses.
- During the experiments, water was observed to adhere to the plate surface upon impact, with the effect increasing for larger plate angles and more flexible plates, but decreasing under aerated wave conditions. This effect may be caused by the formation of a localised low-pressure region at the plate–wall intersection. It is recommended that future studies further investigate this phenomenon to clarify the underlying mechanisms and assess the influence of aeration.
- It was observed that water passing through the 1 mm gap between the plate and the tank wall revealed high-frequency plate responses (500 Hz and above) for the elastic plates. It is recommended that future studies further investigate these high-frequency responses to better understand their implications during breaking wave impacts.

References

[1] V. Sarano, "Rogue wave," 1991. [Online]. Available: https://www.nationalgeographic.nl/wetenschap/2022/06/enorme-monstergolven-kunnen-uit-het-niets-verschijnen-de-wiskunde-verklaart-hun-geheim.

[2] A. Patra, S.-K. Min, P. Kumar, and X. Wang, "Changes in extreme ocean wave heights under 1.5 °C, 2 °C, and 3 °C global warming," *Weather and Climate Extremes*, vol. 33, 2021. DOI: 10.1016/j.wace.2021.100358.

[3] R. Gopalakrishnakurup, "WAVE IMPACT ON SEMI-SUBMERSIBLE UNITS: A REVIEW OF DESIGN STANDARDS," in *Proceedings of the International Conference on Offshore Mechanics and Arctic Engineering - OMAE*, vol. 2, 2022, ISBN: 9780791885864. DOI: 10.1115/OMAE2022-81456.

[4] M. Derakhti, M. L. Banner, and J. T. Kirby, "Predicting the breaking strength of gravity water waves in deep and intermediate depth," *Journal of Fluid Mechanics*, vol. 848, 2018, ISSN: 14697645. DOI: 10.1017/jfm.2018.352.

[5] A. Varing, J. F. Filipot, S. Grilli, R. Duarte, V. Roeber, and M. Yates, "A new definition of the kinematic breaking onset criterion validated with solitary and quasi-regular waves in shallow water," *Coastal Engineering*, vol. 164, 2021, ISSN: 03783839. DOI: 10.1016/j.coastaleng.2020.103755.

[6] W. Lafeber, L. Brosset, and H. Bogaert, "Elementary loading processes (ELP) involved in breaking wave impacts: Findings from the Sloshel project," in *Proceedings of the International Offshore and Polar Engineering Conference*, 2012.

[7] C. Lugni, M. Brocchini, and O. M. Faltinsen, "Wave impact loads: The role of the flip-through," in *Physics of Fluids*, vol. 18, 2006. DOI: 10.1063/1.2399077.

[8] T. Mai, C. Mai, A. Raby, and D. M. Greaves, "Hydroelasticity effects on water-structure impacts," *Experiments in Fluids*, vol. 61, no. 9, 2020, ISSN: 14321114. DOI: 10.1007/s00348-020-03024-3.

[9] R. W. Bos and P. R. Wellens, "Fluid structure interaction between a pendulum and focused breaking waves," *Physics of Fluids*, vol. 33, no. 6, 2021, ISSN: 10897666. DOI: 10.1063/5.0054426.

[10] G. N. Bullock, C. Obhrai, D. H. Peregrine, and H. Bredmose, "Violent breaking wave impacts. Part 1: Results from large-scale regular wave tests on vertical and sloping walls," *Coastal Engineering*, vol. 54, no. 8, pp. 602–617, Aug. 2007, ISSN: 0378-3839. DOI: 10.1016/J.COASTALENG.2006.12.002.

[11] A. Ghadirian and H. Bredmose, "Pressure impulse theory for a slamming wave on a vertical circular cylinder," *Journal of Fluid Mechanics*, vol. 867, R1, May 2019, ISSN: 14697645. DOI: 10.1017/jfm.2019.151.

[12] U. Jain, P. Vega-Martínez, and D. Van Der Meer, "Air entrapment and its effect on pressure impulses in the slamming of a flat disc on water," *Journal of Fluid Mechanics*, vol. 928, 2021. DOI: 10.1017/jfm.2021.846.

[13] M. van Meerkerk, C. Poelma, B. Hofland, and J. Westerweel, "Gas flow dynamics over a plunging breaking wave prior to impact on a vertical wall," *European Journal of Mechanics, B/Fluids*, vol. 91, pp. 52–65, Jan. 2022, ISSN: 09977546. DOI: 10.1016/J.EUROMECHFLU.2021.09.008/GAS{_}FLOW{_}DYNAMICS{_}OVER{_}A{_}PLUNGING{_}BREAKING{_}WAVE{_}PRIOR{_}TO{_}IMPACT{_}ON{_}A{_}VERTICAL{_}WALL.PDF.

[14] M. Derakhti and J. T. Kirby, "Breaking-onset, energy and momentum flux in unsteady focused wave packets," *Journal of Fluid Mechanics*, vol. 790, 2016, ISSN: 14697645. DOI: 10.1017/jfm.2016.17.

[15] D. J. Wood, D. H. Peregrine, and T. Bruce, “Wave Impact on a Wall Using Pressure-Impulse Theory. I: Trapped Air,” *Journal of Waterway, Port, Coastal, and Ocean Engineering*, vol. 126, no. 4, 2000, ISSN: 0733-950X. DOI: 10.1061/(asce)0733-950x(2000)126:4(182).

[16] A. Hoque and S. I. Aoki, “Distributions of void fraction under breaking waves in the surf zone,” *Ocean Engineering*, vol. 32, no. 14-15, 2005, ISSN: 00298018. DOI: 10.1016/j.oceaneng.2004.11.013.

[17] G. N. Bullock, A. R. Crawford, P. J. Hewson, M. J. Walkden, and P. A. Bird, “The influence of air and scale on wave impact pressures,” *Coastal Engineering*, vol. 42, no. 4, pp. 291–312, Apr. 2001, ISSN: 0378-3839. DOI: 10.1016/S0378-3839(00)00065-X. [Online]. Available: https://www.sciencedirect.com/science/article/pii/S037838390000065X?pes=vor&entityID=https%3A%2F%2Flogin.tudelft.nl%2Fsso%2Fsaml2%2Fidp%2Fmetadata.php&utm_source=mendeley&getft_integrator=mendeley.

[18] D. H. Peregrine and L. Thais, “The effect of entrained air in violent water wave impacts,” *Journal of Fluid Mechanics*, vol. 325, 1996, ISSN: 00221120. DOI: 10.1017/S0022112096008166.

[19] T. P. Stanton and E. B. Thornton, “Profiles of void fraction and turbulent dissipation under breaking waves in the surf zone,” in *Coastal Engineering 2000 - Proceedings of the 27th International Conference on Coastal Engineering, ICCE 2000*, vol. 276, 2000. DOI: 10.1061/40549(276)6.

[20] H. Bredmose, G. N. Bullock, and A. J. Hogg, “Violent breaking wave impacts. Part 3. Effects of scale and aeration,” *Journal of Fluid Mechanics*, vol. 765, 2015, ISSN: 14697645. DOI: 10.1017/jfm.2014.692.

[21] H. J. Lim, K. A. Chang, Z. C. Huang, and B. Na, “Experimental study on plunging breaking waves in deep water,” *Journal of Geophysical Research: Oceans*, vol. 120, no. 3, 2015, ISSN: 21699291. DOI: 10.1002/2014JC010269.

[22] G. B. Deane and M. D. Stokes, “Air entrainment processes and bubble size distributions in the surf zone,” *Journal of Physical Oceanography*, vol. 29, no. 7, 1999, ISSN: 00223670. DOI: 10.1175/1520-0485(1999)029<1393:AEPABS>2.0.CO;2.

[23] Y. Shao, B. Song, D. Wan, and J. Wang, “Numerical study of air entrainment mechanisms and vortical structures in breaking waves,” *Ocean Engineering*, vol. 341, p. 122 569, Dec. 2025, ISSN: 0029-8018. DOI: 10.1016/J.OCEANENG.2025.122569. [Online]. Available: https://www.sciencedirect.com/science/article/pii/S0029801825022528.

[24] G. Costigan and P. B. Whalley, “Measurements of the speed of sound in air-water flows,” *Chemical Engineering Journal*, vol. 66, no. 2, 1997, ISSN: 13858947. DOI: 10.1016/S1385-8947(96)03169-5.

[25] A. B. Wood, *A Textbook of Sound*, 1946th ed. London: G. Belle and Sons LTD, 1941.

[26] M. Elhimer, N. Jacques, A. El Malki Alaoui, and C. Gabillet, “The influence of aeration and compressibility on slamming loads during cone water entry,” *Journal of Fluids and Structures*, vol. 70, pp. 24–46, Apr. 2017, ISSN: 0889-9746. DOI: 10.1016/J.JFLUIDSTRUCTS.2016.12.012. [Online]. Available: https://www.sciencedirect.com/science/article/pii/S0889974616302419.

[27] M. van der Eijk and P. Wellens, “An efficient pressure-based multiphase finite volume method for interaction between compressible aerated water and moving bodies,” *Journal of Computational Physics*, vol. 514, p. 113 167, Oct. 2024, ISSN: 0021-9991. DOI: 10.1016/J.JCP.2024.113167. [Online]. Available: https://www.sciencedirect.com/science/article/pii/S0021999124004169.

[28] N. Zhang, L. Xiao, Z. Cheng, H. Wei, and G. Chen, “Classification of breaking wave impact loads on a fixed surface-piercing square column with an overhanging deck,” *Coastal Engineering*, vol. 193, p. 104 570, Oct. 2024, ISSN: 0378-3839. DOI: 10.1016/J.COASTALENG.2024.104570.

[29] D. Linton, R. Gupta, D. Cox, J. van de Lindt, M. E. Oshnack, and M. Clauson, “Evaluation of Tsunami Loads on Wood-Frame Walls at Full Scale,” *Journal of Structural Engineering*, vol. 139, no. 8, 2013, ISSN: 0733-9445. DOI: 10.1061/(asce)st.1943-541x.0000644.

[30] G. Zhang, X. Chen, and D. Wan, “MPS-FEM Coupled Method for Study of Wave-Structure Interaction,” *Journal of Marine Science and Application*, vol. 18, no. 4, 2019, ISSN: 19935048. DOI: 10.1007/s11804-019-00105-6.

[31] T. Attili, V. Heller, and S. Triantafyllou, “Wave impact on rigid and flexible plates,” *Coastal Engineering*, vol. 182, 2023, ISSN: 03783839. DOI: 10.1016/j.coastaleng.2023.104302.

[32] M. J. Cooker, “Liquid impact, kinetic energy loss and compressibility: Lagrangian, Eulerian and acoustic viewpoints,” *Journal of Engineering Mathematics*, vol. 44, no. 3, 2002, ISSN: 00220833. DOI: 10.1023/A:1020943222015.

[33] S. U. Galiev and R. G. Flay, “The transient interaction of plates with extreme water waves: Effects of deformability and hull cavitation,” in *WIT Transactions on the Built Environment*, vol. 105, 2009. DOI: 10.2495/FSI090161.

[34] C. E. Brennen, *Cavitation and bubble dynamics*. 2013. DOI: 10.1017/CBO9781107338760.

[35] S. U. Galiev and R. G. Flay, “Interaction of breaking waves with plates: The effect of hull cavitation,” *Ocean Engineering*, vol. 88, 2014, ISSN: 00298018. DOI: 10.1016/j.oceaneng.2014.04.024.

[36] Z. Hu and Y. Li, “Two-dimensional simulations of large-scale violent breaking wave impacts on a flexible wall,” *Coastal Engineering*, vol. 185, 2023, ISSN: 03783839. DOI: 10.1016/j.coastaleng.2023.104370.

[37] T. Attili, V. Heller, and S. Triantafyllou, “Scaling approaches and scale effects in wave–flexible structure interaction,” *Journal of Fluids and Structures*, vol. 123, 2023, ISSN: 10958622. DOI: 10.1016/j.jfluidstructs.2023.103987.

[38] B. Hofland, M. Kaminski, and G. Wolters, “Large scale wave impact on a vertical wall,” *Coastal Engineering Proceedings*, no. 32, 2011, ISSN: 0589-087X. DOI: 10.9753/icce.v32.structures.15.

[39] O. M. Faltinsen, “Water entry of a wedge by hydroelastic orthotropic plate theory,” *Journal of Ship Research*, vol. 43, no. 3, 1999, ISSN: 00224502. DOI: 10.5957/jsr.1999.43.3.180.

[40] A. Bereznitski, “Slamming: The role of hydroelasticity,” *International Shipbuilding Progress*, vol. 48, no. 4, 2001, ISSN: 0020868X.

[41] V. K. Govindasamy, M. A. Chella, S. Sannasi Annamalaisamy, and P. S. Rajamanickam, “Impact pressure distribution and characteristics of breaking wave impact on a monopile,” *Ocean Engineering*, vol. 271, 2023, ISSN: 00298018. DOI: 10.1016/j.oceaneng.2023.113771.

[42] M. A. Chella, A. Tørum, and D. Myrhaug, “An overview of wave impact forces on offshore wind turbine substructures,” in *Energy Procedia*, vol. 20, 2012. DOI: 10.1016/j.egypro.2012.03.022.

[43] B. Abrahamsen, A. Holstad, and Ø. Hellan, “The importance of local hydroelastic effects when calculating structural response from measured wave slamming pressures,” in *Proceedings of the International Conference on Offshore Mechanics and Arctic Engineering - OMAE*, vol. 1, 2024, ISBN: 9780791887783. DOI: 10.1115/OMAE2024-127172.

[44] B. C. Abrahamsen, F. Grytten, Ø. Hellan, T. H. Søreide, and O. M. Faltinsen, “Hydroelastic response of concrete shells during impact on calm water,” *Journal of Fluids and Structures*, vol. 116, 2023, ISSN: 10958622. DOI: 10.1016/j.jfluidstructs.2022.103804.

[45] O. M. Faltinsen and A. N. Timokha, *Sloshing*. Cambridge University Press, Sep. 2009, ISBN: 978-0-521-88111-1. [Online]. Available: www.cambridge.org.

[46] R. W. Bos, M. Van Der Eijk, J. H. Den Besten, and P. R. Wellens, “A reduced order model for FSI of tank walls subject to wave impacts during sloshing,” *International Shipbuilding Progress*, vol. 69, no. 2, 2022, ISSN: 15662829. DOI: 10.3233/ISP-220003.

[47] M. Van Der Eijk and P. R. Wellens, “A compressible two-phase flow model for pressure oscillations in air entrapments following green water impact events on ships,” *International Shipbuilding Progress*, vol. 66, no. 4, 2020, ISSN: 15662829. DOI: 10.3233/ISP-200278.

[48] M. van der Eijk and P. Wellens, “Two-phase free-surface flow interaction with moving bodies using a consistent, momentum preserving method,” *Journal of Computational Physics*, vol. 474, 2023, ISSN: 10902716. DOI: 10.1016/j.jcp.2022.111796.

[49] D. Zuzio, A. Orazzo, J. L. Estivalèzes, and I. Lagrange, “A new efficient momentum preserving Level-Set/VOF method for high density and momentum ratio incompressible two-phase flows,” *Journal of Computational Physics*, vol. 410, 2020, ISSN: 10902716. DOI: 10.1016/j.jcp.2020.109342.

[50] J. H. Jung, H. S. Yoon, and C. Y. Lee, “Effect of natural frequency modes on sloshing phenomenon in a rectangular tank,” *International Journal of Naval Architecture and Ocean Engineering*, vol. 7, no. 3, pp. 580–594, May 2015, ISSN: 2092-6782. DOI: 10.1515/IJNAOE-2015-0041. [Online]. Available: https://www.sciencedirect.com/science/article/pii/S2092678216300668.

[51] H. Akyildiz and N. Erdem Ünal, “Sloshing in a three-dimensional rectangular tank: Numerical simulation and experimental validation,” *Ocean Engineering*, vol. 33, no. 16, 2006, ISSN: 00298018. DOI: 10.1016/j.oceaneng.2005.11.001.

[52] S. Y. Kim, K. H. Kim, and Y. Kim, “Comparative study on pressure sensors for sloshing experiment,” *Ocean Engineering*, vol. 94, 2015, ISSN: 00298018. DOI: 10.1016/j.oceaneng.2014.11.014.

[53] Z. Huang, D. Spencer, R. Oberlies, G. Watts, and W. Xiao, “Wave impact experiment of a GBS model in large waves,” in *Proceedings of the International Conference on Offshore Mechanics and Arctic Engineering - OMAE*, vol. 1, 2017, ISBN: 9780791857632. DOI: 10.1115/OMAE2017-61473.

[54] Y. J. Ha, K. H. Kim, B. W. Nam, and S. Y. Hong, “Experimental investigation for characteristics of wave impact loads on a vertical cylinder in breaking waves,” *Ocean Engineering*, vol. 209, 2020, ISSN: 00298018. DOI: 10.1016/j.oceaneng.2020.107470.

[55] B. C. Abrahamsen and O. M. Faltinsen, “Scaling of entrapped gas pocket slamming events at dissimilar Euler number,” *Journal of Fluids and Structures*, vol. 40, pp. 246–256, Jul. 2013, ISSN: 0889-9746. DOI: 10.1016/J.JFLUIDSTRUCTS.2013.04.009. [Online]. Available: https://www.sciencedirect.com/science/article/pii/S0889974613001151?via%3Dihub.

[56] J. C. Scott, “The role of salt in whitecap persistence,” *Deep Sea Research and Oceanographic Abstracts*, vol. 22, no. 10, pp. 653–657, Oct. 1975, ISSN: 0011-7471. DOI: 10.1016/0011-7471(75)90002-9. [Online]. Available: https://www.sciencedirect.com/science/article/pii/0011747175900029.

[57] K. M. Kleefsman, G. Fekken, A. E. Veldman, B. Iwanowski, and B. Buchner, “A Volume-of-Fluid based simulation method for wave impact problems,” *Journal of Computational Physics*, vol. 206, no. 1, 2005, ISSN: 10902716. DOI: 10.1016/j.jcp.2004.12.007.

[58] *Program documentation — ComFLOW 4.2.0-alpha documentation*. [Online]. Available: https://poseidon.housing.rug.nl/sphinx/index_documentation.html.

[59] Bromlewe. Jimme, “Green water impacts on flexible breakwaters - an experimental study,” Technical University of Delft, Delft, Tech. Rep., Apr. 2025, pp. -88.

[60] C. E. Shannon, “Communication in the Presence of Noise,” *Proceedings of the IRE*, vol. 37, no. 1, 1949, ISSN: 00968390. DOI: 10.1109/JRPROC.1949.232969.

[61] J. D. Anderson, “Modern compressible flow with historical perspective.,” 1982.

Acknowledgments

I would like to express my gratitude to my supervisor and the staff of the Ship Hydromechanics laboratory for their guidance during this thesis. I greatly appreciated Peter Wellens's continuous openness and support throughout this project, which allowed me to explore broad theoretical areas, pursue my own interests, reflect on intriguing hypotheses during our many meetings, work with advanced instruments that made exploration of new dimensions possible, and ultimately connect these insights to the practical completion of this thesis. It has been a pleasure to work on this project under such engaging and interactive supervision.

I am also grateful to Sebastian Schreier for introducing me to the precise art of sensor calibration and for his assistance in navigating the electrical maze of the system, Peter Poot for his guidance in designing the experimental components, Jasper den Ouden, Ton Veer, Frits Sterk, and Pascal Chabot for their help in realising the experimental setup, Marnix Bockstael for his support with CFD simulations, and Sedat Tokgöz for his assistance in configuring the high-speed camera system.

A

System calibration

The sensors and equipment are calibrated prior to the experiments in an environment similar to the sloshing rig. The applied calibration procedures and results are described in detail for each component.

A.1. Load cells

The load cells are first calibrated independently, outside of the wave tank and without any additional structural elements. This step established the baseline calibration curve for each sensor. The load cells are calibrated in both tension and compression (Figure A.1b and Figure A.1a) using static load steps, thereby creating a full hysteresis loop. The static load steps are chosen to be in the range of the expected loads (Table 3.2), ranging from 0 (relative) to 40kg in steps of 5kg for each load cell going from zero load to maximum load and back to zero.

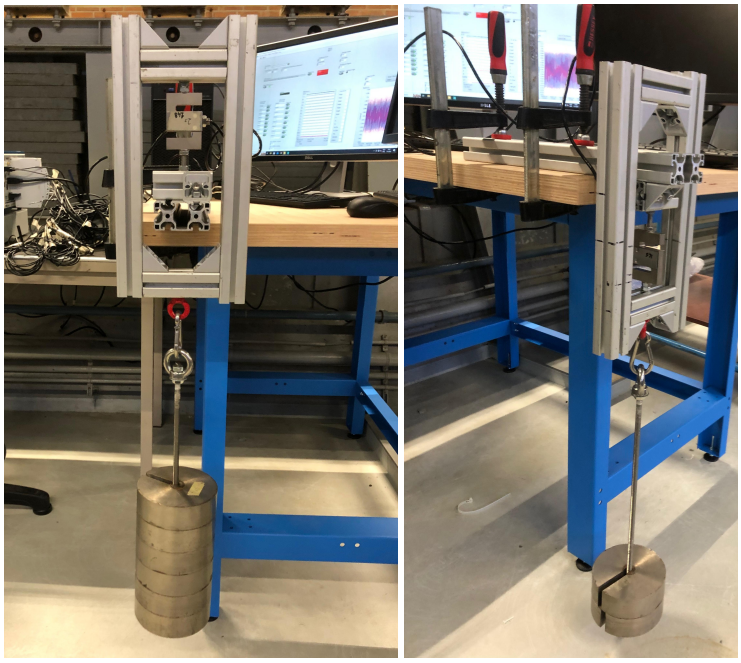

(a) The load cell loaded in compression **(b)** The load cell loaded in tension

Figure A.1: Load cell configurations.

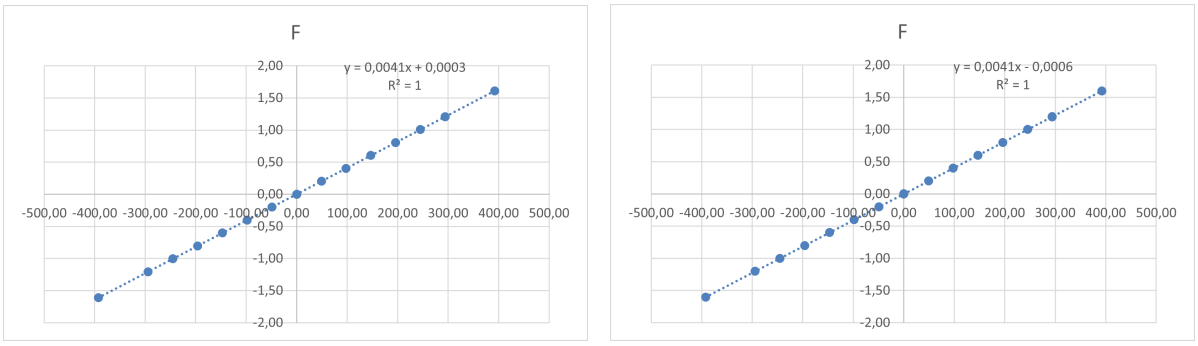

(a) **(b)**

Figure A.2: The force curves of the load cells 146(a) and 148(b) that were used in the experiment.

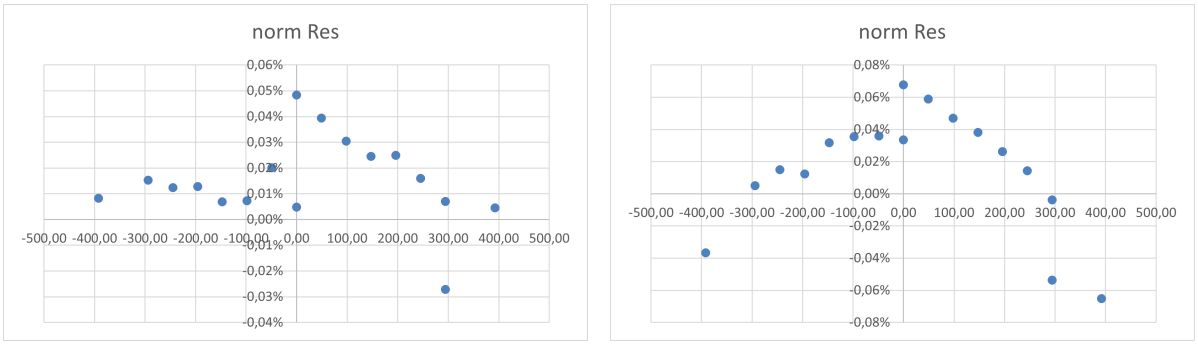

(a) **(b)**

Figure A.3: The normalised residuals of the load cells 146(a) and 148(b) that were used in the experiment.

The second stage of calibration is performed with the load cells mounted in their experimental positions inside the wave tank, but without the rods that provide rotational stiffness. This procedure accounts for any installation effects, such as preloading, mounting misalignments, or stiffness effects of the sub-assembly, which could influence the sensor readings compared to the baseline condition. Wall-friction causes hysterisis which should be avoided to ensure replicable results. The load (0-30kg) was applied to compress the load cells with the use of pulleys.

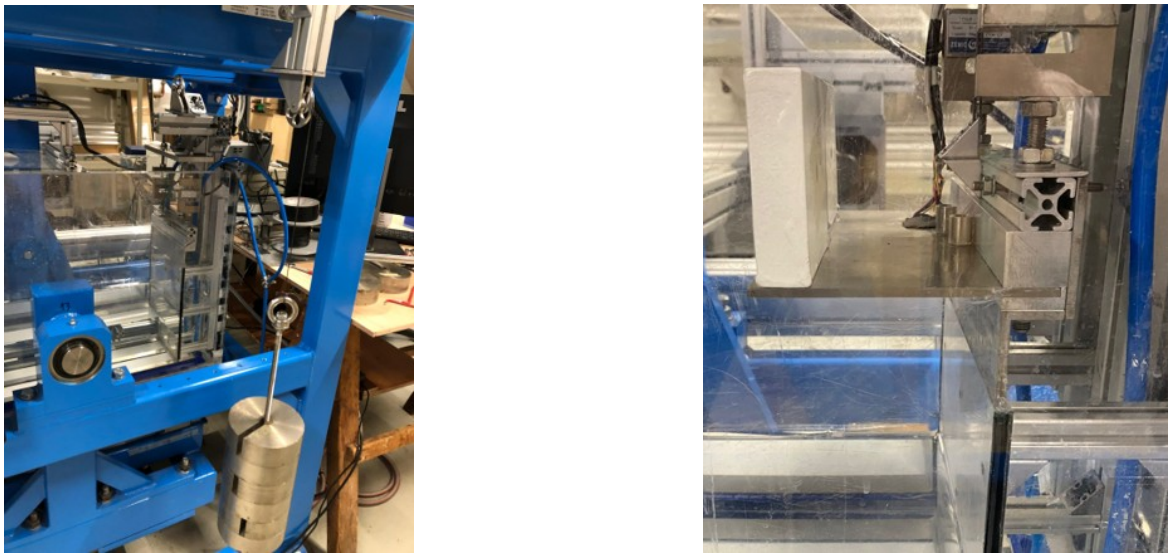

(a) (b)

Figure A.4: System configurations for testing the behaviour of the load cell: (a) the load cells mounted in the system with a compression load applied with the use of pulleys, (b) an applied moment on the load cells.

Finally, the load cells are calibrated with the full assembly in place, including the rods that provide rotational stiffness of the sub-assembly. The comparison between calibration of the first, second and third calibrations is shown below:

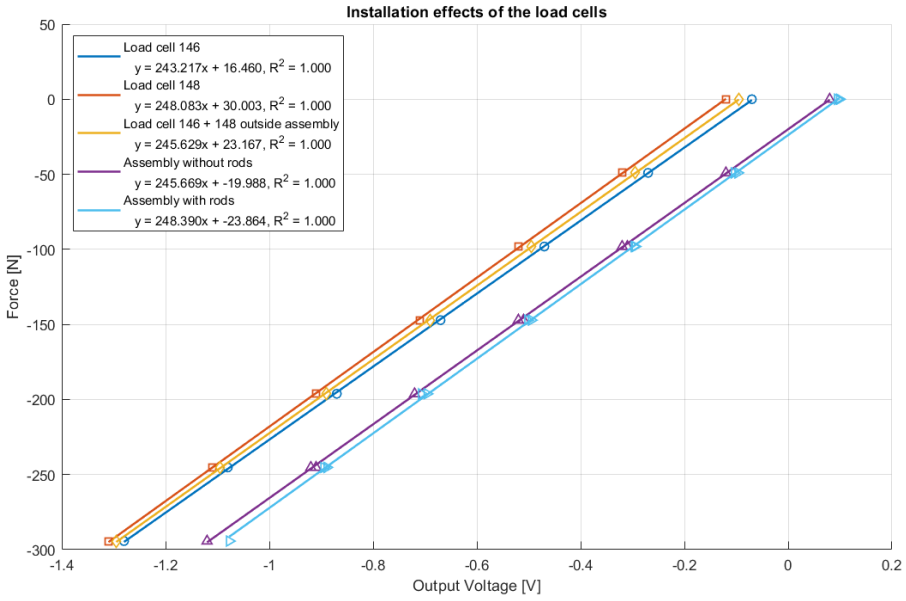

Figure A.5: Installation effects on the output of the load cells.

In addition to the calibration procedure, the sensitivity of the linear load cells with respect to applied moments on the impact plate is tested. The aim is to determine whether off-axis loading introduces systematic variations in the measured vertical force. First, a calibrated mass of 1.9937 kg is positioned centrally, aligned with both load cells. In this configuration, the applied moment is zero. Subsequently, the same mass is shifted by 6.3 cm from the centreline, which introduces a moment relative to the load cell axis. Finally, the weight is positioned 9.4 cm from the centreline close to the plate edge, which

results in a higher applied moment. The corresponding applied moments and measured loads are summarised in Table A.1. The results show that a resulting moment can have a significant effect on the measured force by the load cells. The actual effect will depend on wave/plate configurations.

Table A.1: Sensitivity of linear load cells to applied moments.

Position of weight	Applied moment [Nm]	Measured load [N]	Effect [%]
Aligned with load cells (0 cm)	0.000	19.7222	0.00
Shifted 6.3 cm	0.62	19.85	0.63
Shifted 9.4 cm	0.92	20.64	4.66

A.2. Pressure sensors

The pressure sensors were calibrated using a high-accuracy reference pressure sensor (Omega model: MMA050V1B4ME0T3A5CE) with a known calibration traceable to the applied water column. A water column system with a maximum pressure capacity of 1 bar was used to provide the reference pressure for calibration. The setup of for the calibration of the sensors is shown in Figure A.6a and a detailed view of the connection in Figure A.6b.

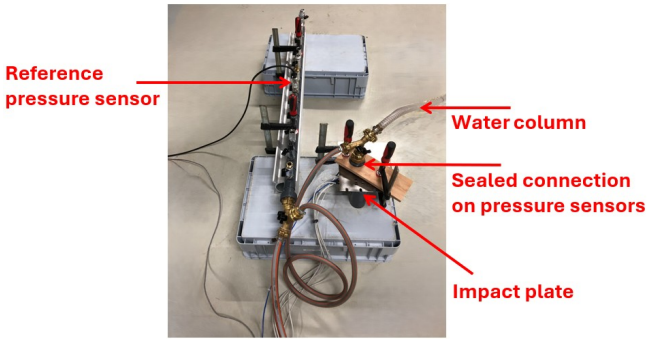

(a) The setup used for the calibration of the SMI and PCB pressure sensors.

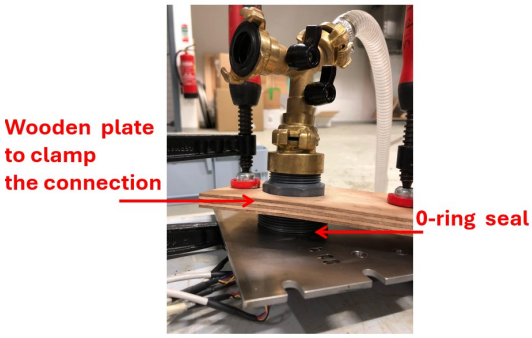

(b) Detailed view of the sealed connection.

Figure A.6

For the SMI pressure sensors, calibration was performed under static pressure conditions. These sensors respond to steady pressure levels, making them suitable for direct comparison with the water column reference. In contrast, the piezoelectric PCB sensors required dynamic (impulse) pressure measurements, since they are designed to measure absolute pressure changes. Due to their decay characteristic, the piezoelectric sensors gradually return to their baseline value under static conditions, which makes static calibration inappropriate.

To achieve the desired calibration points, the pressure in the water column was adjusted by controlling the valves, thereby changing the effective height of the water column and the applied hydrostatic pressure. For the PCB sensors, each measurement cycle required the pressure to be relieved after recording, ensuring that the sensor returned to its baseline state before the next calibration step. This procedure helped to minimise drift effects and ensured consistent measurement conditions throughout the calibration process.

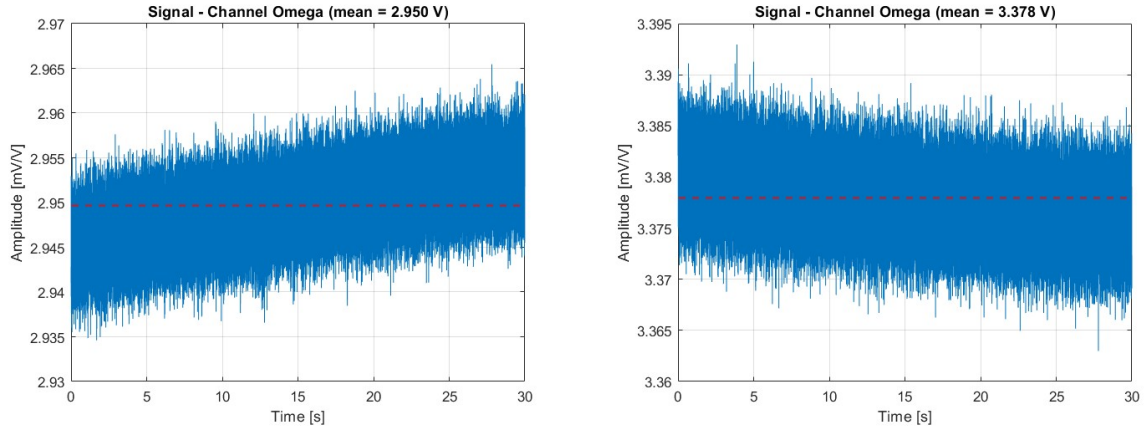

(a) (b)

Figure A.7: The signal of the Omega reference sensor and the SMI pressure sensors displayed a small increase or decrease over the 30 second measurement, which can be related to the slow retraction(a) or expansion(b) of the rubber hose of the water column, resulting in a slight increase or decrease in the water column and therefore pressure.

Because of the behaviour of the piezo PCB pressure sensors, the measured pressure signal returns to its zero value because it does a relative pressure measurement, meaning that over time it becomes zero again (Figure A.8b). For that reason the PCB sensors are loaded with an impulse and its peak values are compared to the Omega pressure sensor.

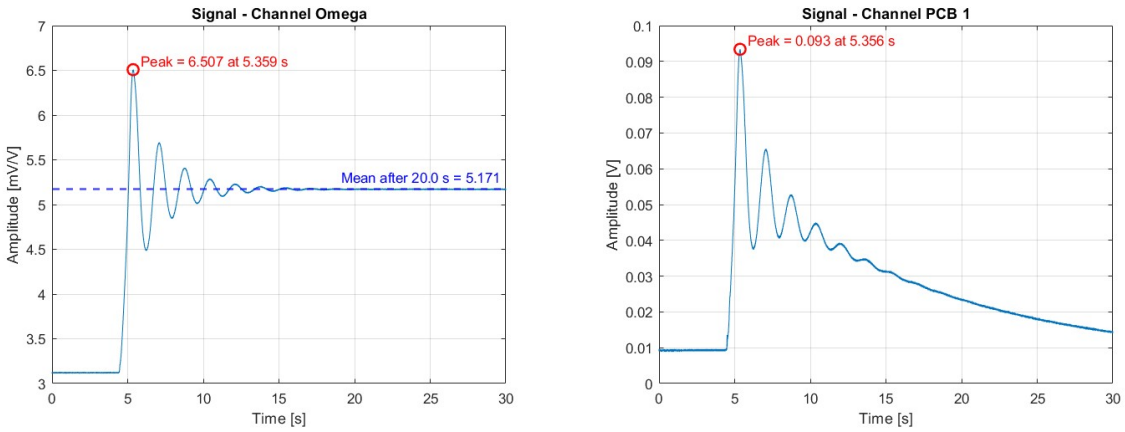

(a) (b)

Figure A.8: Comparison between the signal of the Omega reference sensor and the piezo PCB sensor.

The results of the calibration test are presented in the figures below.

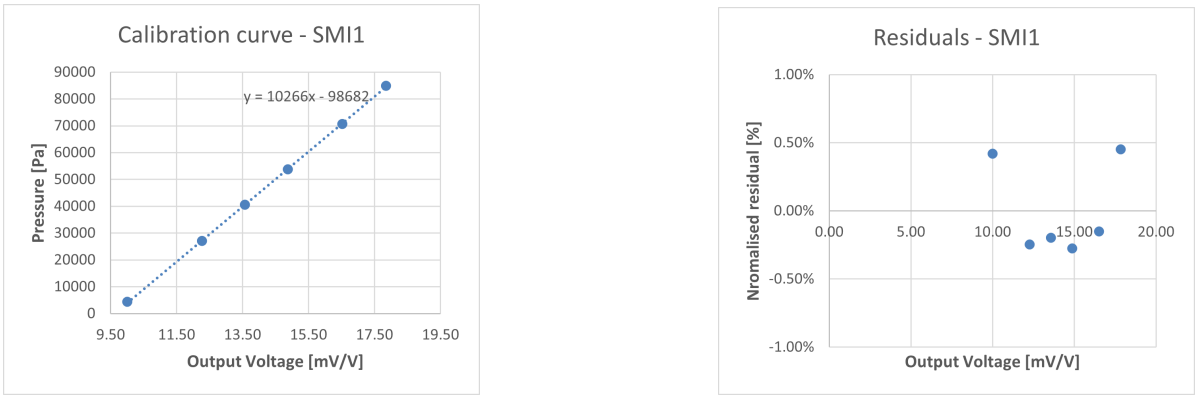

(a) (b)

Figure A.9: Trend line and residuals of the SMI1 pressure sensor.

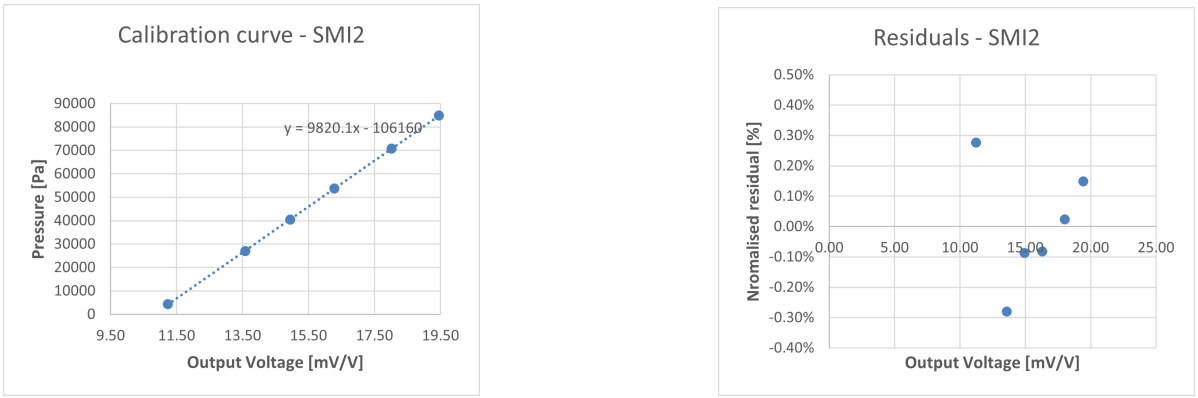

(a) (b)

Figure A.10: Trend line and residuals of the SMI2 pressure sensor.

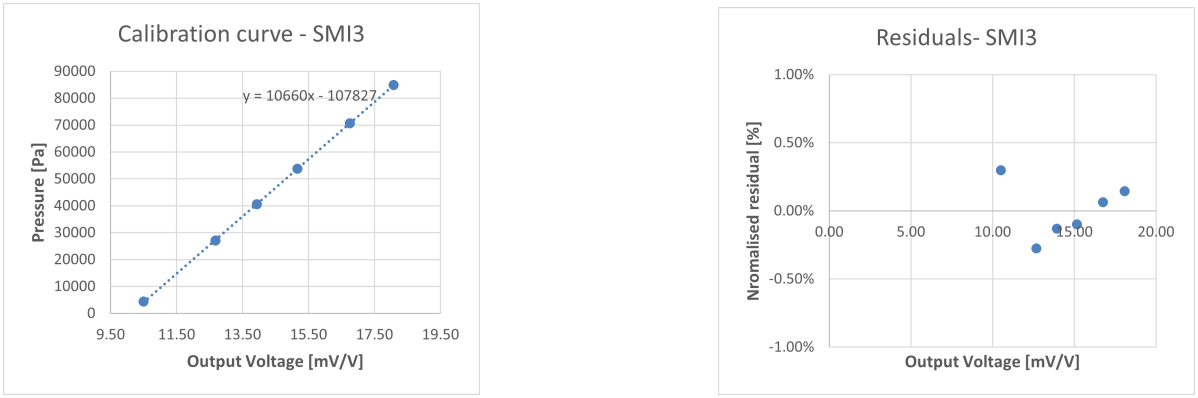

(a) (b)

Figure A.11: Trend line and residuals of the SMI3 pressure sensor.

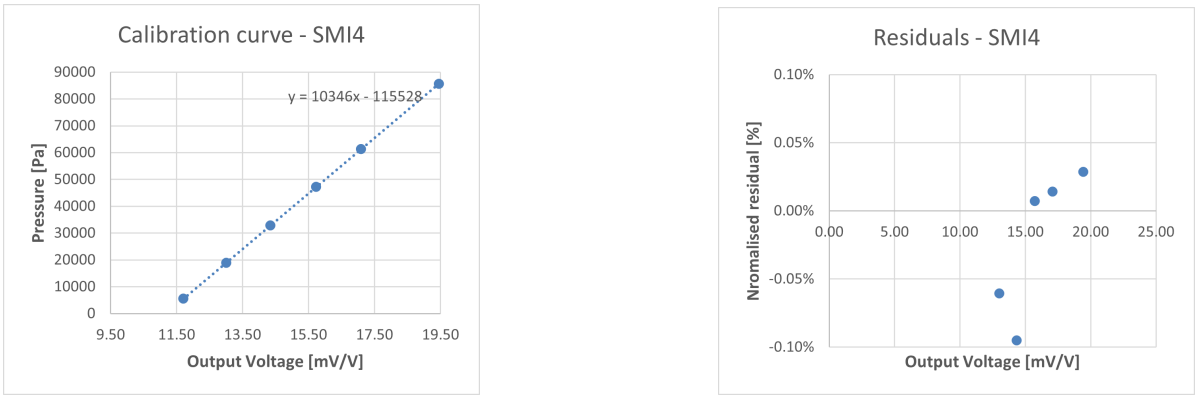

(a) (b)

Figure A.12: Trend line and residuals of the SMI4 pressure sensor.

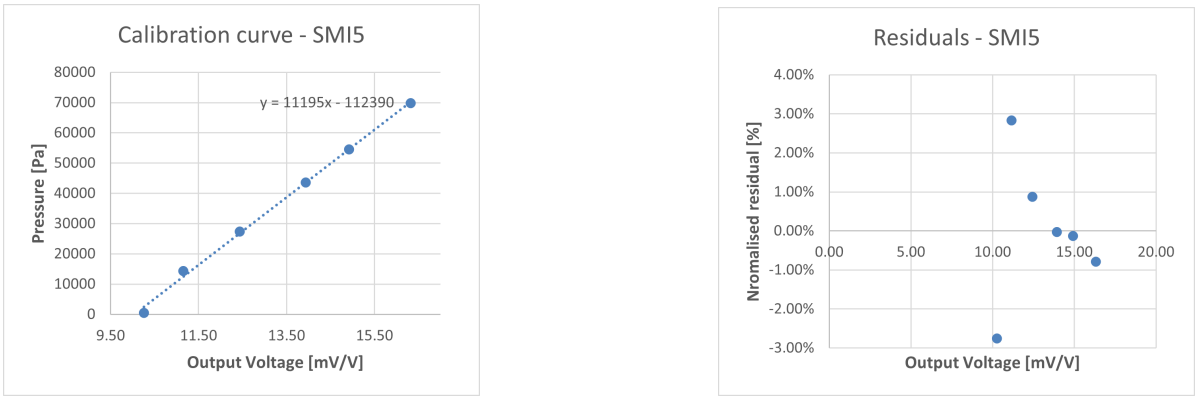

(a) (b)

Figure A.13: Trend line and residuals of the SMI5 pressure sensor.

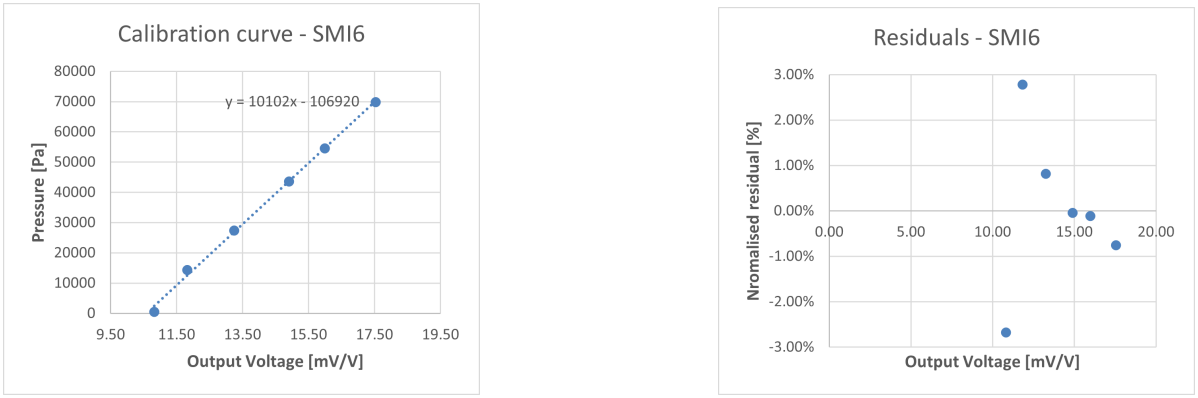

(a) (b)

Figure A.14: Trend line and residuals of the SMI6 pressure sensor.

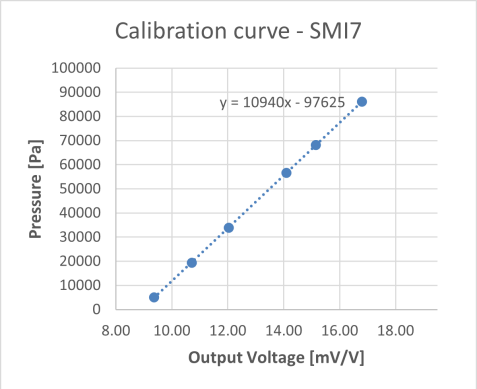

(a)

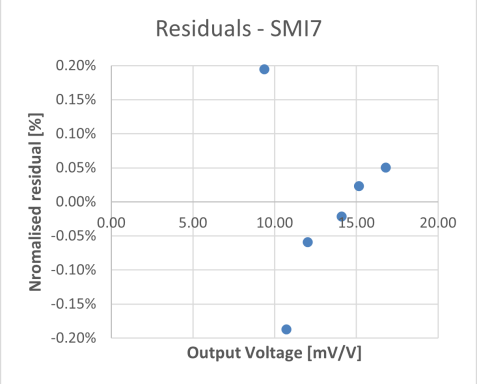

(b)

Figure A.15: Trend line and residuals of the SMI7 pressure sensor.

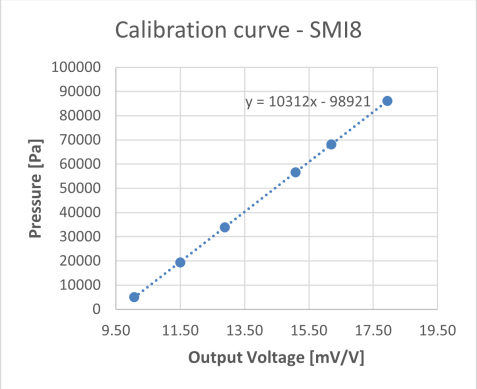

(a)

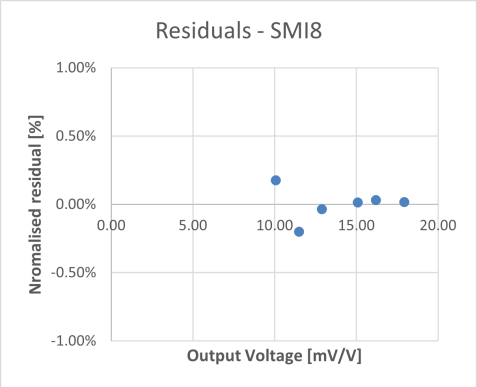

(b)

Figure A.16: Trend line and residuals of the SMI8 pressure sensor.

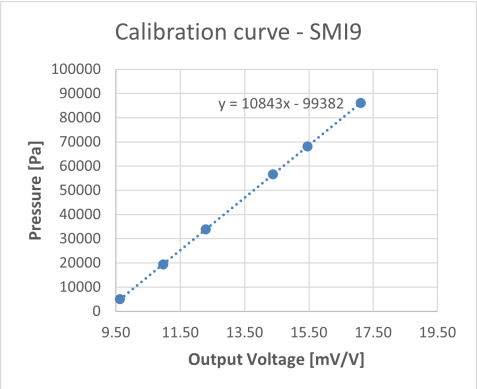

(a)

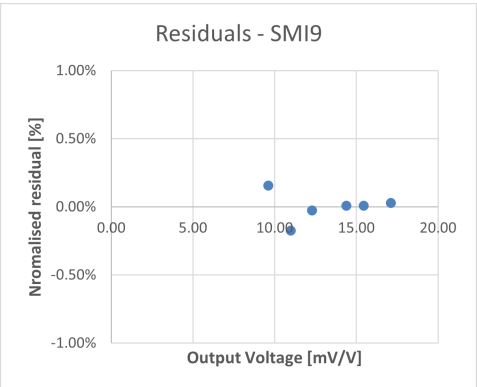

(b)

Figure A.17: Trend line and residuals of the SMI9 pressure sensor.

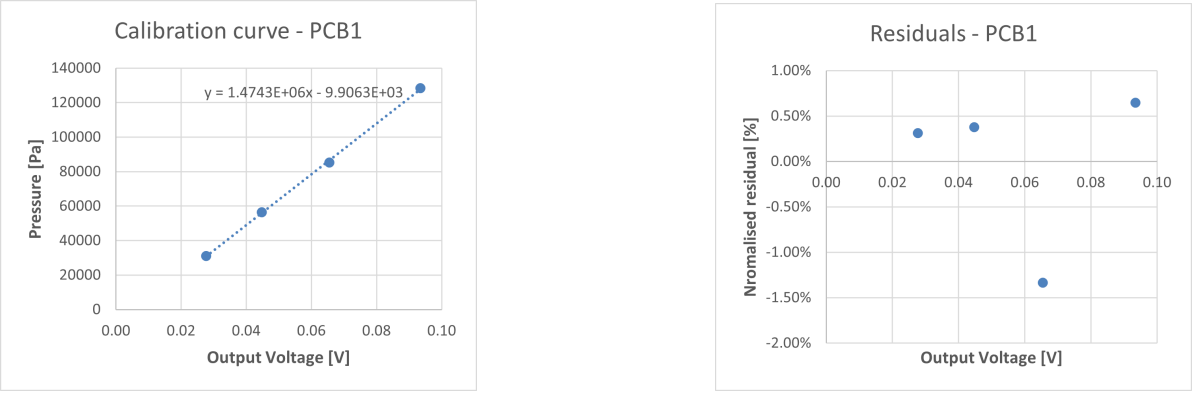

(a) (b)

Figure A.18: Trend line and residuals of the PCB1 pressure sensor.

(a) (b)

Figure A.19: Trend line and residuals of the PCB3 pressure sensor.

A.3. Laser distance sensors

For the calibration procedure, an impact plate from the experiment, to ensure consistent reflection, is positioned at a series of known distances from each sensor. The measurement range of the sensor spans from +200 mm to +600 mm.

Under the current configuration, the output is approximately 0 V (0.060 V measured) when the object is located at a distance of 400 mm. Voltages are positive in the range from 200 mm to 400 mm, and negative from 400 mm to 600 mm. The calibration of the lasers is done in the region of interest, i.e. between 200 mm and 400 mm from the plate.

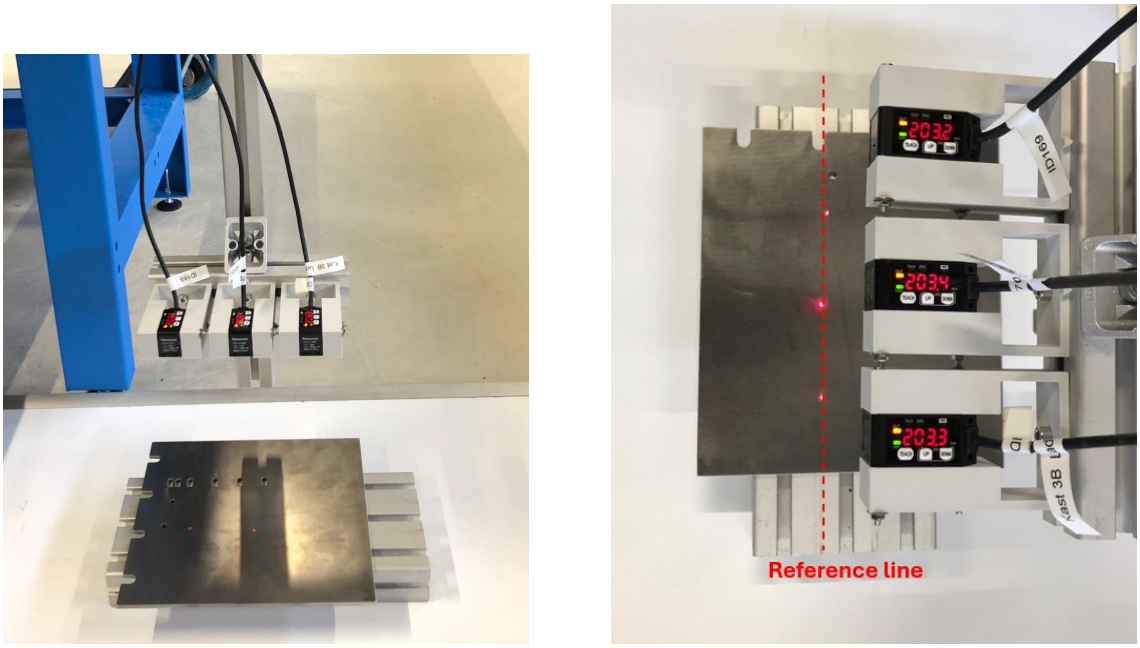

(a) (b)

Figure A.20: The setup for the calibration of the lasers. The focus points of the lasers are not at an equal distance, see the reference line.

This calibration test was performed for each of the three sensors individually to ensure consistent response characteristics across the set. The results are shown in the figures below.

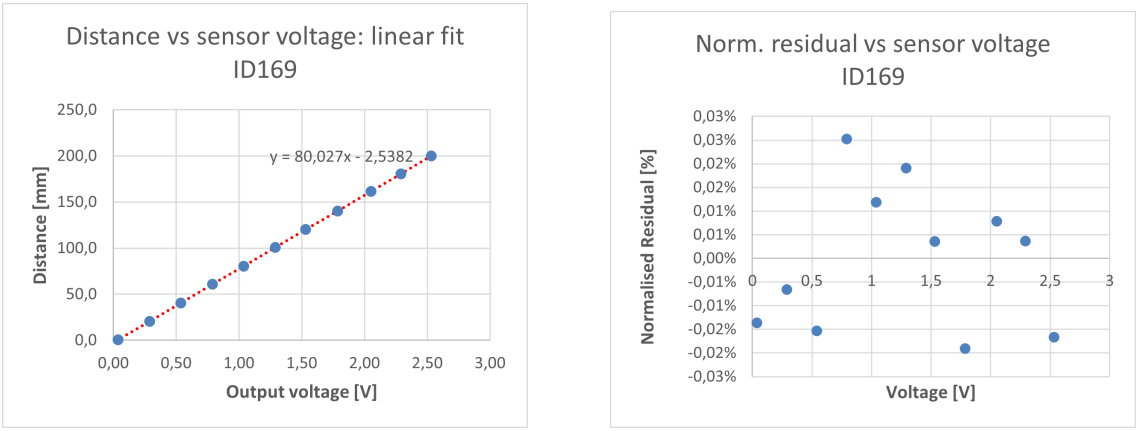

(a) (b)

Figure A.21: Trend line and residuals of laser sensor ID169.

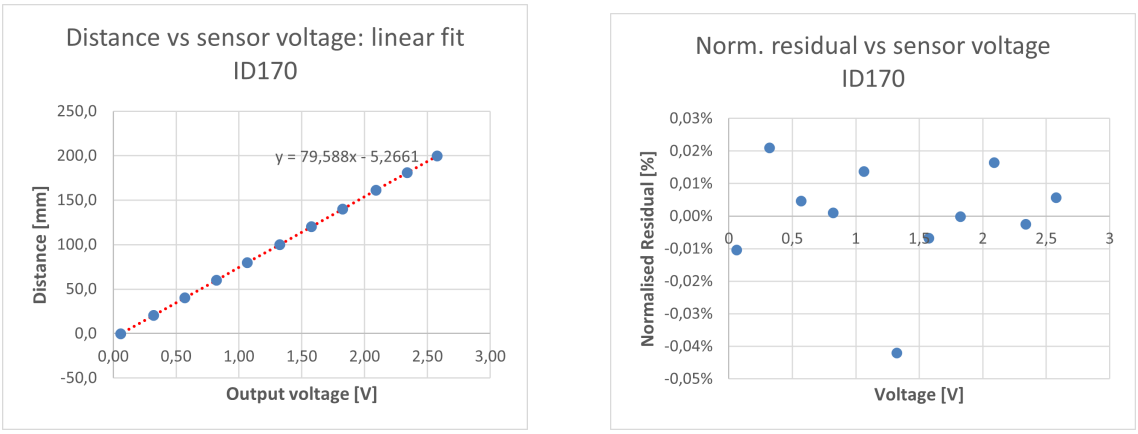

(a) (b)

Figure A.22: Trend line and residuals of laser sensor ID170.

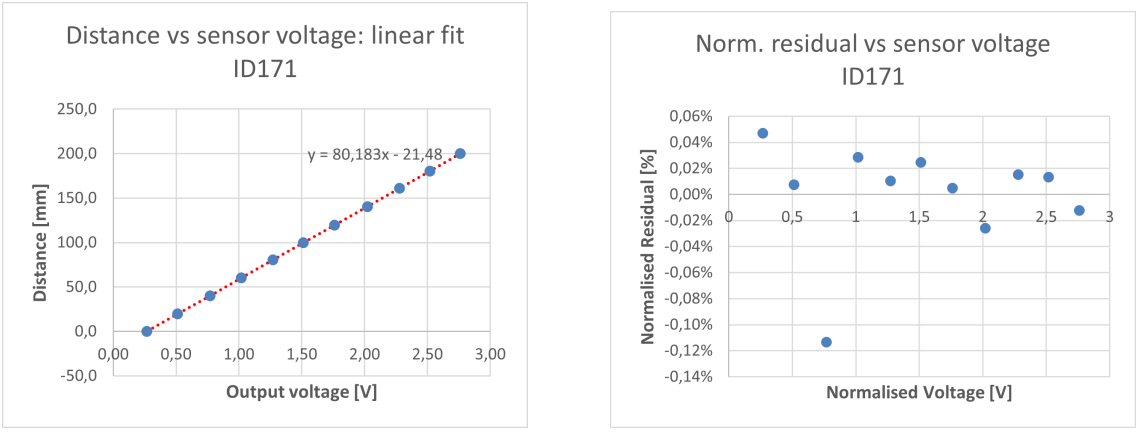

(a) (b)

Figure A.23: Trend line and residuals of laser sensor ID171.

A.4. Tank position sensor

The position of the sloshing rig was measured using a caliper and compared with the sensor output to assess accuracy. A filter was applied to reduce noise in the sensor signal and ensure the sloshing rig consistently started from 50 mm before moving to the desired direction. The filtering slightly altered the signal, requiring a minor adjustment of the tank input voltage to maintain correct alignment.

A.5. Wave gauge

The wave gauge is based on stainless-steel (RVS) strips, which are highly sensitive to the electrical properties of the surrounding water. To ensure consistent measurements, the water in the tank must originate from a single reservoir, thereby maintaining a constant salinity and pH. Since the strips require time to stabilise through a gradual corrosion process, the gauge is immersed in the tank water prior to measurements while a current is applied. This initial phase allows the sensor response to reach a stable state, serving as a pre-calibration procedure. Nonetheless, the stable state must be verified at the start of each testing day.

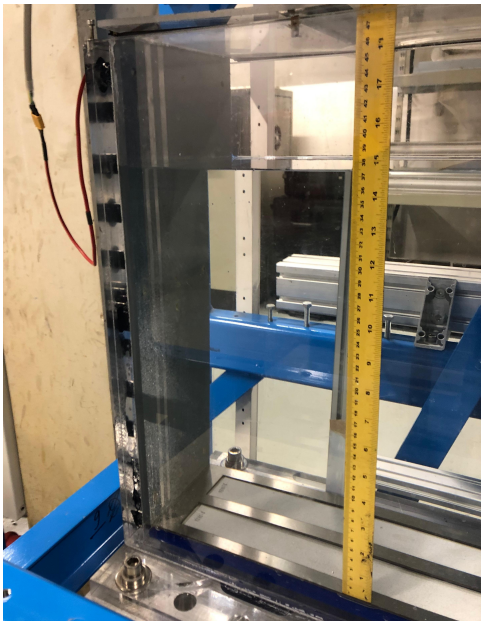

Figure A.24: Measuring the wave height and signal of the wave gauge.

Once the corrosion effects have stabilised, the wave gauge can be calibrated, although recalibration is needed over time. An example of the results of the calibration are shown in Figure A.25. A ruler is placed in the tank to provide reference water levels, which are then compared to the gauge output. The signal amplifier of the gauge provides an output in the range of $\pm 5V$, where both the offset and gain can be adjusted. For this setup, the offset is set such that the still water level of 145 mm corresponds approximately to an output of 0 V. The gain and the offset must be set such that the output is of $\pm 5V$, as this is the maximum allowable voltage for the data acquisition.

The gain is set at 1x with an offset of 1.00 and determines the amplification of the input signal: increasing the gain enhances the output signal magnitude, making the variations more distinguishable. However, this also amplifies noise and possible signal distortion. Conversely, if the gain is set too low, the resulting weak output signal may be difficult to separate from noise during post-processing. Therefore, an appropriate balance between signal strength and noise amplification is required for accurate wave measurements.

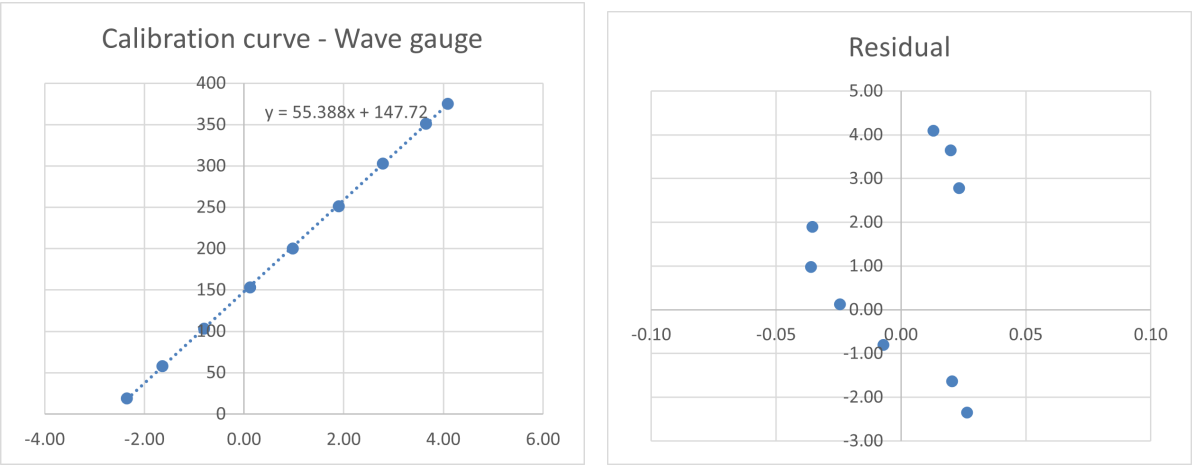

(a) **(b)**

Figure A.25: Trend line and residuals of the wave gauge calibration.

A.6. Aeration stones

An aeration float is a buoyant device used to indicate the level of aeration in a tank where air is introduced through aeration stones. As the stones release bubbles, the water becomes less dense and the total volume increases. The float responds to these changes by adjusting its position in the tank, assuming that the air will only leave the system at the free water surface. The change in volume is defined as:

$$V_{\Delta} = V_{aerated} - V_{water} \tag{A.1}$$

In the same manner the water height can be determined by the difference in the water level before and after aeration.

$$h_{\Delta} = h_{aerated} - h_{water} \tag{A.2}$$

The percentage of aeration is then calculated as:

$$aeration = \frac{V_{\Delta}}{V_{aerated}} \cdot 100\% = \frac{h_{\Delta}}{h_{aerated}} \cdot 100\% \tag{A.3}$$

Air is supplied through a mass flow controller, which provides an output signal between 2V and 10V, corresponding to a flow range of 0 to 5kg/h (i.e., 0 to 4080L/h or 68L/min). Each diffuser is set to deliver a maximum of 7L/min at 3.45bar, giving a total of 14L/min for the two diffusers.

The corresponding controller voltage for this maximum flow given by:

$$\frac{14}{68} \approx 0.2 \tag{A.4}$$

$$0.2 \times (10\,\mathrm{V} - 2\,\mathrm{V}) + 2\,\mathrm{V} = 3.6\,\mathrm{V} \tag{A.5}$$

Therefore, 3.6 V represents the maximum permissible flow rate through the diffusers.

While the pressure regulator is set to 3.45 bar, additional pressure losses in the system may require a higher inlet pressure to achieve the desired flow. Adjustments can be made accordingly to maintain sufficient aeration performance.

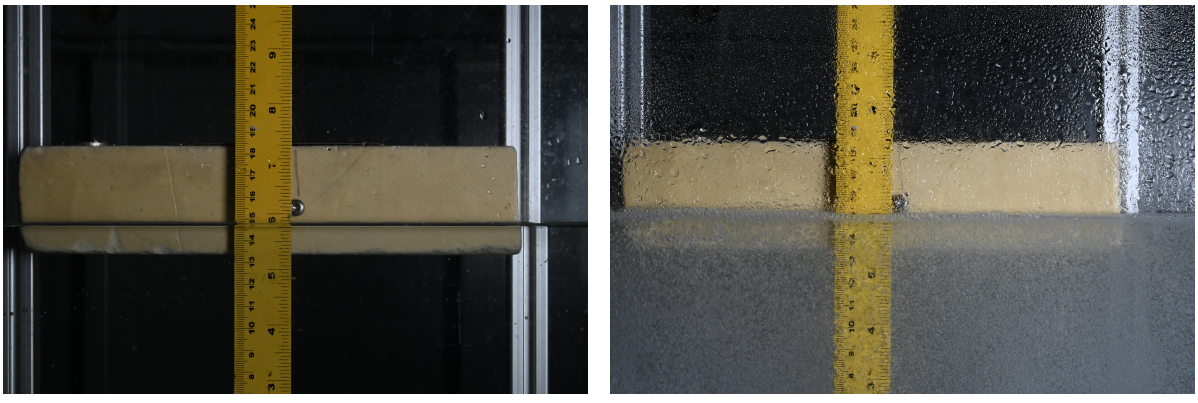

(a) (b)

Figure A.26: Change of mixture volume: (a) non-aerated still water level, and (b) aerated water level.

As air is introduced through bubble diffusers, the water becomes less dense and slightly expands in volume. To ensure consistent test conditions, a target relative water height of 145 mm was established.

However, due to practical considerations, the bottom plate surrounding the bubble diffusers was not included in the setup. This component has a volume of 106.704 mm^3, which would normally displace water. To compensate and maintain an equivalent total water volume, this volume is subtracted from the system by adjusting the water height.

The effective surface area at the maximum water level was estimated by subtracting the footprints of structural elements from the base area including the impact wall, wave gauge, the air tubes and the ITEM profiles. Neglecting the minor effect of triangular brackets, this results in an effective surface area of 106.444 mm^2. To offset the missing plate volume, the water height is adjusted downward by 106.704/106.444=1mm from 145mm to 144 mm.

A.7. High-Speed Cameras

The experimental setup employs two high-speed cameras, each with a distinct focus. Camera 1 is dedicated to capturing the wave and plate dynamics, while Camera 2 is used to observe potential cavitation beneath the impact plate. Consequently, the spatial scale of objects differs significantly between the two recordings.

Prior to calibration, the camera settings are adjusted as follows:

1. **Resolution:** Set according to the required level of detail for the measurements, in this case 1024x1024.
2. **Frame rate:** Chosen to adequately capture the wave-plate interaction and cavitation bubbles (20000 fps). A higher frame rate reduces the amount of light available to the sensor.
3. **Shutter speed:** Determines the exposure time. Short exposure reduces motion blur but results in darker images. The chosen shutter speed is 1/20664 seconds.
4. **Aperture:** Controls the amount of light passing through the lens. A low number (e.g. 2) corresponds to a wide aperture, increasing light intake but reducing depth of field, whereas a high f-number (e.g. 32) narrows the aperture. The chosen aperture for Camera 1 is 16 and for Camera 2 the aperture is 2.8.

Calibration is performed by filming a ruler placed at the measurement location. The pixel count corresponding to a given physical length is then determined, ensuring that the calibration is valid for the exact plane in which the experiments are conducted. With the current settings, a resolution of 41 pixels per cm is obtained.

Figure A.27: The number of pixels is related to a known distance measured by a ruler.

B

Repeatability experiment

To ensure the reliability and verify the consistency of the experimental results, all test cases are repeated three times under identical conditions. This analysis quantifies the variability between repeated measurements to confirm the reproducibility of the observed impact loads and structural responses. The repeatability and normalised standard deviation are presented for each test code, with each test code representing three identical runs. The test codes ($X_1X_2X_3X_4X_5$) are defined as follows:

Table B.1: Description of test code components.

Component	Description	Values
X_1	Plate angle	$A = 0°$, $B = 10°$, $C = 20°$, $D = 30°$
X_2X_3	Plate thickness	$05 = 0.5$ mm, $10 = 1.0$ mm, $15 = 1.5$ mm, $40 = 4.0$ mm
X_4	Percentage of aeration	$0 = 0\%$, $1 = 1\%$, $2 = 2\%$, $4 = 4\%$
X_5	Wave approach angle	$1 = 30°$, $2 = 20°$, $3 = 10°$, $4 = 5°$

B.1. Forces

The repeatability of the maximum forces is evaluated for a plate thickness of $4\,\mathrm{mm}$ at varying aeration levels to assess the variability introduced by aeration. Additionally, tests are conducted for different plate thicknesses to investigate the influence of plate rigidity on the measured forces.

Effect of Aeration

Figure B.1 shows that the absolute differences in measured forces increase with larger wave angles. Furthermore, this effect appears more pronounced for aerated impacts compared to non-aerated ones.

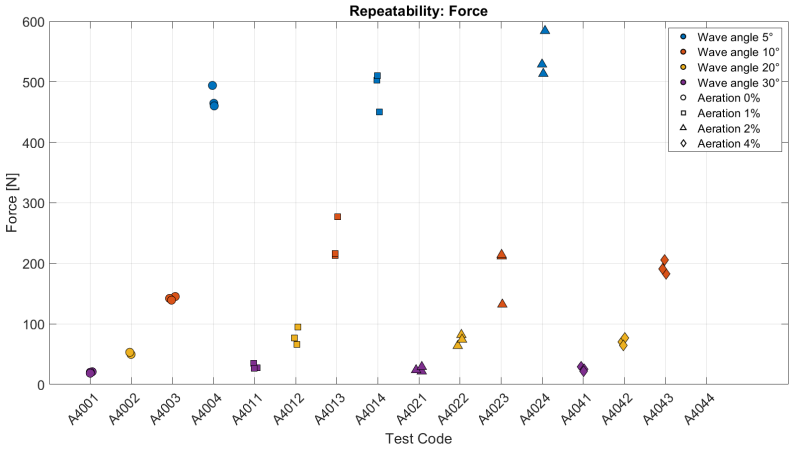

Figure B.1: Repeatability study on the maximum force measured on a 4 mm plate for different levels of aeration.

The relative differences are represented by the normalised standard deviation in Figure B.2. It can be observed that for no aeration, the variability is the lowest, with a normalised standard deviation of 4.2%, which is comparable to the variability measured in a similar setup by Bromlewe [59]. However, the variability does not increase consistently with higher levels of aeration, and there appears to be no clear relationship between the level of aeration and the normalised variance.

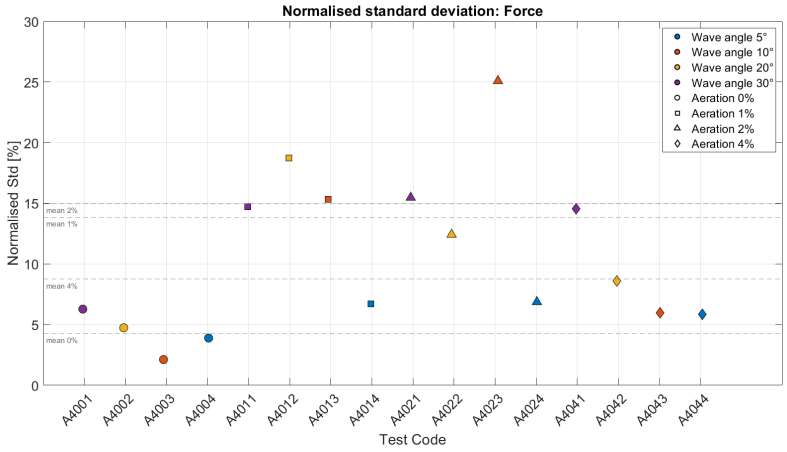

Figure B.2: Normalised standard deviation of the measured maximum force measured on a 4 mm plate for different levels of aeration.

Effect of plate rigidity

The absolute differences in the measured force appear to increase with increasing plate thickness, a trend that is consistent with the observations from the previous analysis.

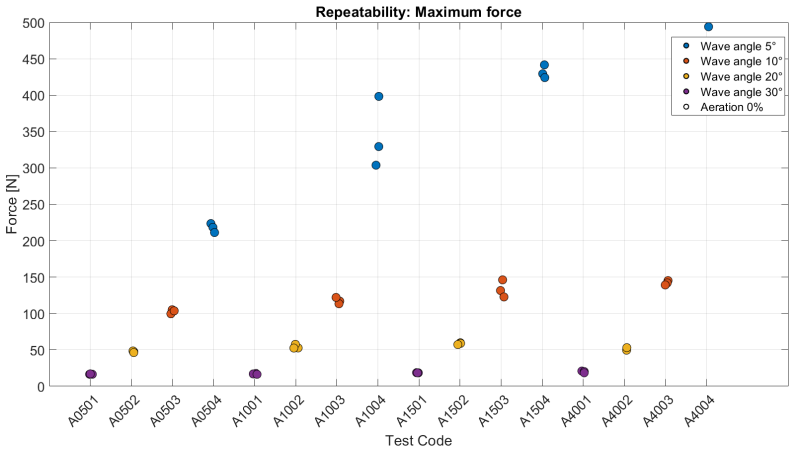

Figure B.3: Repeatability study on the maximum force measured on a 4 mm plate for 0% aeration and different plate thicknesses.

Figure B.4 indicates that there is no clear trend in the variance when comparing rigid plates to more flexible plates.

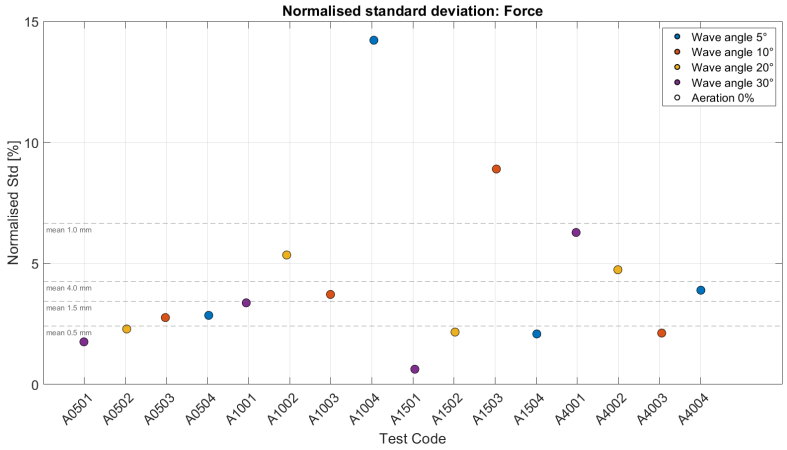

Figure B.4: Normalised standard deviation of the measured the maximum force measured on a 4 mm plate for 0% aeration and different plate thicknesses.

B.2. Pressures

The repeatability of the maximum pressures is evaluated for a plate thickness of $4\,\mathrm{mm}$ at varying aeration levels to assess the variability introduced by aeration. In addition, the effect of the relative angle β_w on pressure variability has been tested. At last, a detailed analysis of the pressure time histories is provided to further illustrate the variability observed in the measured impact pressures.

Effect of Aeration

Figure B.5 illustrates that the maximum pressures exhibit a noticeably larger spread for both aerated and non-aerated impacts compared to the variability observed in Figure B.1. This indicates that pressure measurements can be more sensitive to experimental variations than the corresponding force measurements.

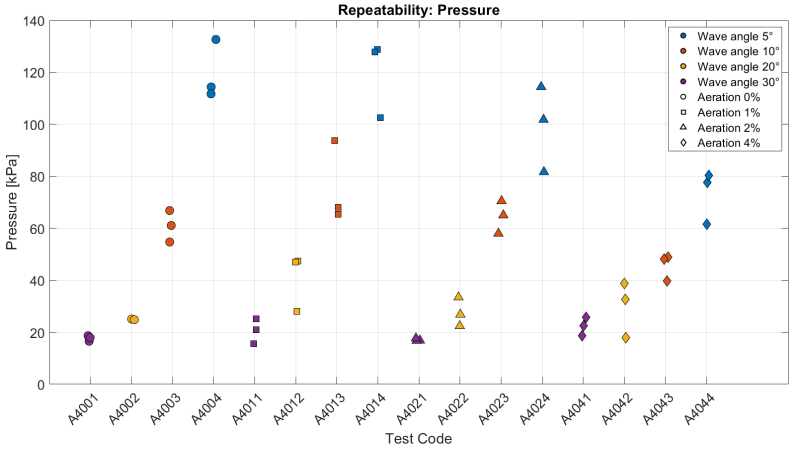

Figure B.5: Repeatability study on the maximum pressure measured on a 4 mm plate for different levels of aeration.

The normalised standard deviation shown in Figure B.6 indicates that in the absence of aeration the variability is lowest with a value of 6%. This is considerably lower than the variability reported by Bromlewe [59]. However, it should be noted that Bromlewe evaluated the mean of the maximum pressures recorded by each individual sensor along the plate, rather than considering the overall maximum pressure across the entire plate length.

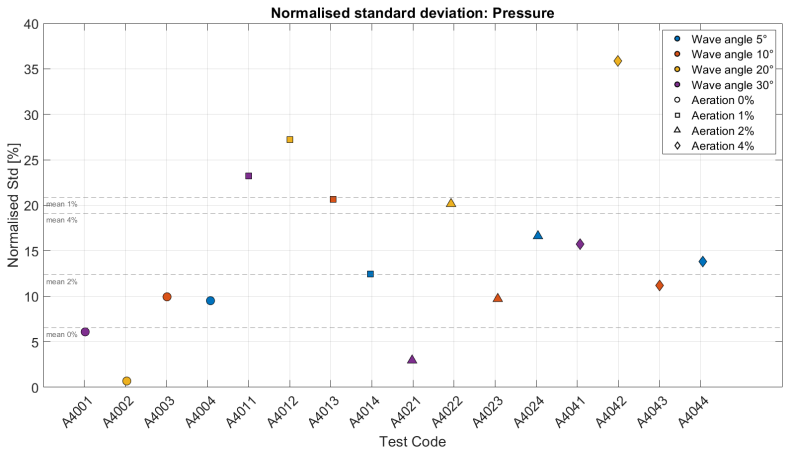

Figure B.6: Normalised standard deviation of the measured maximum pressure measured on a 4 mm plate for different levels of aeration.

Effect of relative angle

Bromlewe [59] noted that significant variance occurs at high maximum pressures during the ”perfect storm” scenario, when the free surface aligns with the angle of the impacted geometry, i.e. when the relative angle β_w is close to 0. In Figure B.7, the largest variance does not occur at $\beta_w = 0$. There appears to be a slight trend of increased variability when the relative angle is negative compared to when it is positive, although this trend is neither consistent nor strictly ordered.

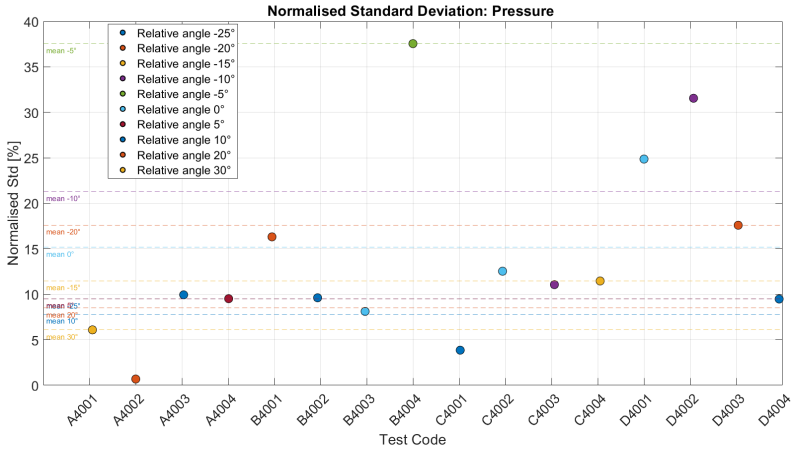

Figure B.7: Normalised standard deviation of the measured maximum pressure measured on a 4 mm plate for different relative angles.

Consistency run-up

The smoothness of this initial run-up depends on the local conditions, as illustrated in Figure B.8b, where the presence of an air bubble ridge may cause a temporary pressure drop immediately before the main pressure peak. This makes the characterisation of the pressure rise time challenging and affects the repeatability the pressure measurements.

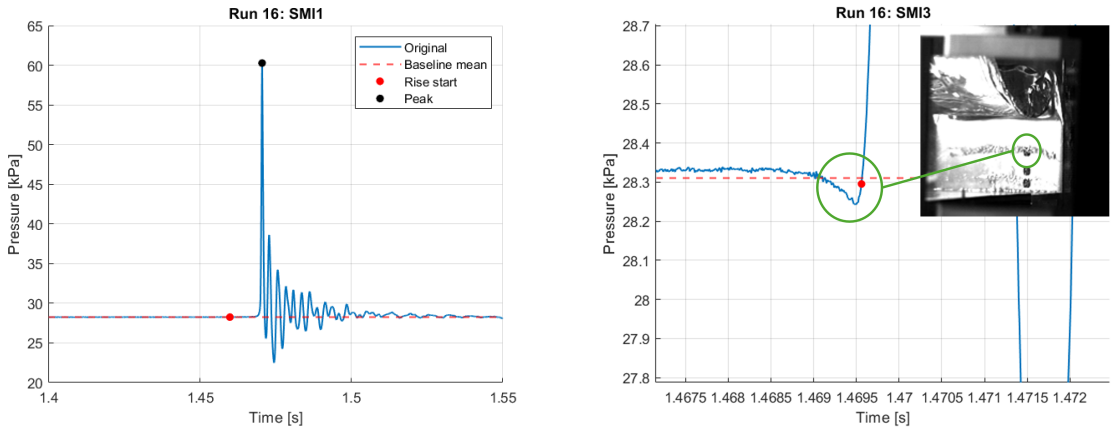

Figure B.8: Examples of pressure over time: (a) the pressure signal at SMI1 for a plate angle of $0°$, wave approach angle of $5°$ and 0% aeration, and (b) an example where the start of the pressure rise at SMI3 is influenced by local free-surface conditions.

B.3. Deflections

The consistency of the measured maximum deflections is verified for plate thickness's of 1.5, 1.0 and 0.5 mm at 0% aeration. The deflections seem to correspond very well in absolute terms of deflection.

The consistency of the measured maximum deflections is evaluated for plate thicknesses of 1.5, 1.0, and 0.5 mm at 0% aeration. The results show that the measured deflections correspond closely across repeated tests, indicating a high level of repeatability in the structural response.

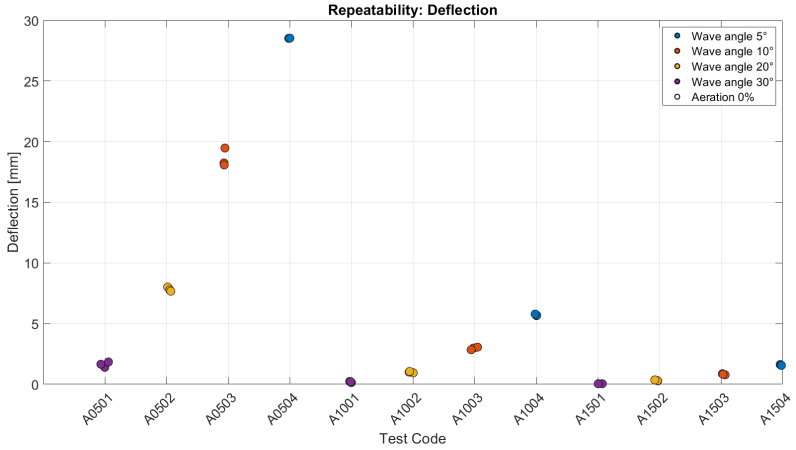

Figure B.9: Repeatability study on the maximum deflection measured for different plate thicknesses at 0% aeration.

Nonetheless, the normalised standard deviation shown in Figure B.10 indicates that, particularly for a wave angle of $30°$, where lower impact loads and consequently smaller deflections are expected, the variability increases. This can be attributed to the fact that the laser distance measurements exhibit significant noise (on the order of millimetres) prior to filtering, making it more difficult to distinguish actual displacement from measurement noise at small deflection magnitudes. Conversely, for smaller

wave angles and thinner plates, which are associated with larger deflections, the variability is notably reduced.

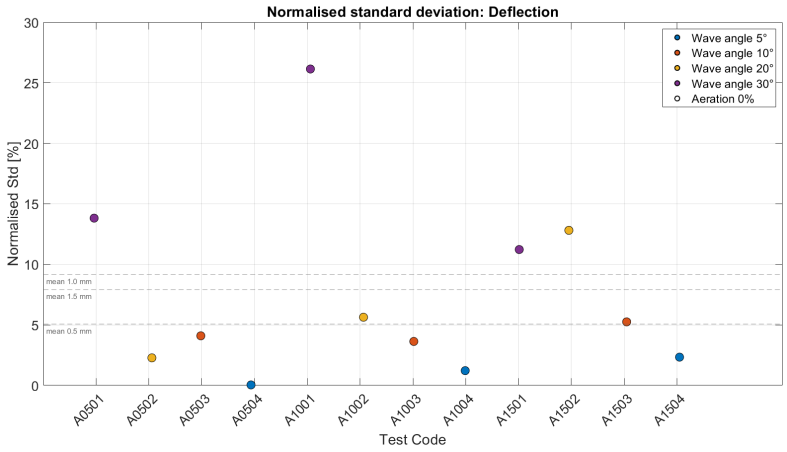

Figure B.10: Normalised standard deviation of the measured the maximum deflection measured for different plate thicknesses at 0% aeration.

B.4. Conclusion repeatability experiment

Overall, the repeatability analysis confirms that the experimental setup provides sufficiently consistent and reliable results across force, pressure, and deflection measurements to allow for the identification of trends. Non-aerated impacts consistently show the lowest variability, with aeration introducing additional fluctuations but without a clear correlation between aeration level and variability. Likewise, plate rigidity does not exhibit a systematic effect on repeatability, suggesting that thickness-related stiffness variations have a limited influence under the tested conditions. The largest variance did not occur at $\beta_w = 0$ for the pressure measurements, but showed an increasing variance when relative plate angles were negative. Local variability in the pressure time histories may be attributed to local aeration effects. And at last, deflection measurements remain consistent except at small amplitudes, where sensor noise becomes significant.

C

Additional observations

During the experiments, several additional observations were made that are not directly related to the primary research questions but may have implications for future studies. These findings are presented and discussed in the sections below.

C.1. Vacuum effect

Upon wave impact, the flexible plate initially deflects upward, followed by a downward motion that for certain plate/wave configurations exceeds the initial displacement. When the secondary deflection surpasses the initial upward deflection, it is hypothesised that a low-pressure region forms near the plate corner which intensifies over time, generating a suction force that pulls the plate downward. Figure C.1 illustrates the temporal evolution of this behaviour, showing the development of the vacuum region and the associated maximum plate deflection. Further research on this phenomenon may clarify the secondary loading mechanisms acting on structures during hydroelastic wave impacts.

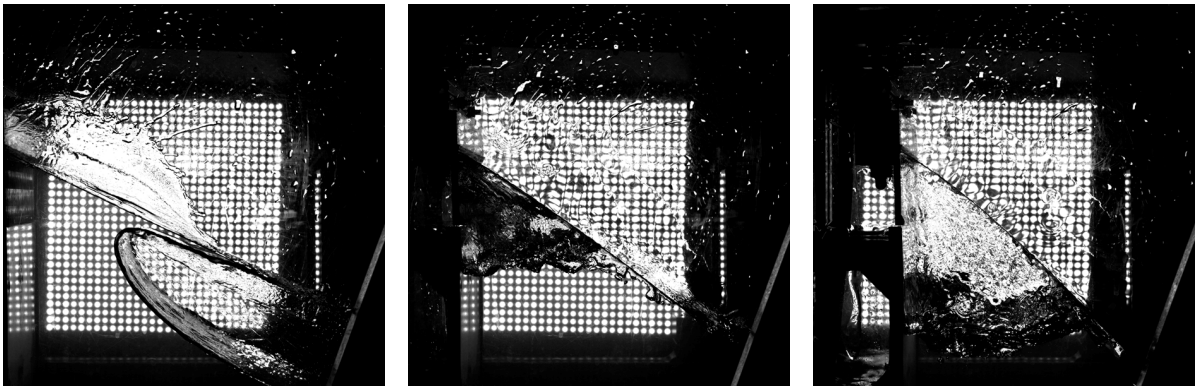

(a) **(b)** **(c)**

Figure C.1: Sequence of the plate response during a single wave impact at an approach angle of 30° on the 0.5 mm plate. A vacuum region forms near the corner, producing a suction effect that “pulls” the plate and leads to the maximum observed deflection.

C.2. High-frequency response

High-frequency structural responses of the plate (500 Hz and above) were revealed when water passed the 1 mm gap between the plate and the tank wall, indicating the presence of high-frequency modes in the system. These modes are distinct from the primary hydroelastic response but may still influence local pressure distributions and pressure measurements during impact. Further investigation is recommended to characterise the origin and implications of these high-frequency responses.

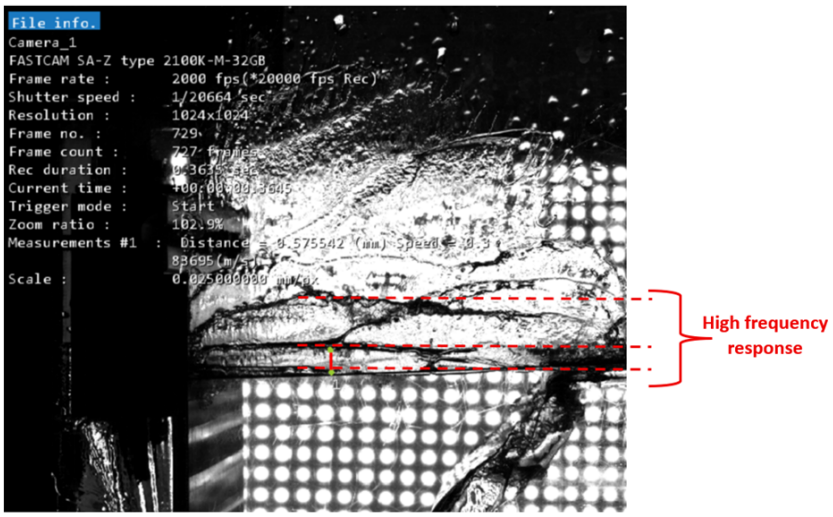

Figure C.2: The high-frequency response of the plate observed in the thin layer of water passing between the plate and the tank wall.